

A New Concept of Sensor for Ultra-high Levels of Radiation based on Radiation Enhanced Oxidation of Copper Thin-films

Présentée le 19 mai 2020

à la Faculté des sciences et techniques de l'ingénieur
Groupe de scientifiques IEL
Programme doctoral en microsystemes et microélectronique

pour l'obtention du grade de Docteur ès Sciences

par

Georgi GORINE

Acceptée sur proposition du jury

Prof. C. Dehollain, présidente du jury
Dr J.-M. Sallese, Dr F. Ravotti, directeurs de thèse
Dr I. Mandic, rapporteur
Dr F. Cerutti, rapporteur
Prof. L. Shchutka, rapporteuse

Arthur turned it over nervously in his hands. "I like the cover," he said.
"**Don't Panic.** It's the first helpful or intelligible thing anybody's said to me all day."
— *Douglas Adams, The Hitchhiker's Guide to the Galaxy*

To my parents... and cats!

Acknowledgements

I would like to show my greatest appreciation to my thesis supervisors Prof. Jean-Michel Sallese and Dr. Federico Ravotti. Your guidance during these years was top class and fundamental for the success of this PhD thesis. Even if located in different sites, we had a wonderful and efficient collaboration bridging between CERN and EPFL with complementary expertise. I must thank you for the stimulating comments and wise suggestions, for the time spent brainstorming over the various challenges and for always helping me pushing all the way through. Thank you for being not only excellent scientific advisors, but also for being very good friends, supportive and care-giving, making this PhD experience incredibly precious both professionally and personally. Grazie!

I am very grateful to jury members that examined the thesis, Prof. Catherine Dehollain and Prof. Lesya Shchutka from EPFL, Dr. Igor Mandic from the Jožef Stefan Institute, and Dr. Francesco Cerutti from CERN, for your insightful comments and interesting discussions during the defense. Thank you for helping me improve the quality of this work making this manuscript more insightful and easier to read.

I am very thankful to the CERN colleagues from the EP department and FCC collaboration that made this thesis project possible: Dr. Michael Moll, Dr. Mar Capeans Garrido, Dr. Petra Riedler, Dr. Burkhard Schmidt and Dr. Alessandro Mapelli. Thanks also to all the other colleagues from EP-DT-DD which all somehow contributed to the realization of this thesis.

Special thanks to the SEM/FIB team from CERN EN/MME Dr. Alexander Lunt, Dr. Elisa Garcia-Tabares Valdivieso and Dr. Ana Teresa Perez Fontenla for the discussions and valuable and professional help with the SEM imaging and analyzes.

Thanks to the CERN FLUKA experts Dr. Andrea Tsinganis, Dr. Robert Froeschl for providing me the results for several DPA simulations and Dr. Maria Ilaria Besana and Dr. Angelo Infantino for sharing your radiation environment simulations for the FCC experiments and accelerator.

Thanks to the efficient, professional, and friendly colleagues from the Jožef Stefan Institute Dr. Luka Snoj, Anže Jazbec, and Sebastjan Rupnik, for their help with the irradiation tests at their TRIGA reactor. Thanks to Dr. Enrico Bravin, Dr. Sune Jakobsen and Dr. Marcus Palm for their valuable help in setting up the irradiation test in the LHC next to their BRAN monitor.

I would like to thank the staff of the Center of MicroNanotechnology of EPFL for providing me with excellent training and guidance. Special thanks to Giancarlo Corradini for his professional work and availability with the dicing and bonding, and to Dr. Didiet Bouvet for his valuable suggestions and fruitful scientific collaboration. Thanks also to Prof. Mikko Ritala and Dr. Katja Väyrynen from the University of Helsinki for providing us with several copper samples and for the collaboration.

A huge thanks goes to my amazing colleagues from the IRRAD team at CERN: Maurice Glaser, Giuseppe Pezzullo, Dr. Isidre Mateu, (soon Dr.) Blerina Gotzke, and Dr. Federico Ravotti.

With the help of Maurice I got my first hands-on experiences with the design of PCBs and profited from his life-long experience on irradiations for getting any CERN-related question always answered. It was

an honor to work with you.

This thesis work would not have been possible without the 360° support from Giuseppe, my colleague, advisor, friend, and best pizza maker ever. Thank you for your priceless contributions in helping setting up and following the irradiation tests, for your encouragements and 24/7 assistance throughout this whole thesis project and beyond. You are the team member that anyone wishes to have and I was lucky enough.

Thanks to my fellow PhD student Blerina, with whom I have started this thesis experience at CERN. Thanks for the great collaboration in running the irradiation facilities and for teaching me how to use all the great software infrastructure you developed for IRRAD. I will always remember how well we represented the team when helping organising and running the RADECS 2017 conference in Geneva, and I will never forget all the paper submissions we rushed together.

Thanks to 50% of Isidoro, for preferring the IRRAD team rather than the SSD group. Thank you for your valuable support both within CERN and outside. Together we expanded so many new skills when working on the ReadMON system and thanks to you I understood how unfriendly Labview can be and why you should never leave your PC unattended and unlocked.

Finally again thank you Federico for being the most welcoming supervisor, for not only sharing your deep knowledge on radiation monitoring devices and radiation effects, but also for tutoring me during the whole learning process both in content and methods. I am extremely proud of having worked with you on this project.

I must thank also my colleagues from the EDLAB group at EPFL Chiara Rossi and Dr. Jacopo Bronuzzi. Thanks Chiara for your moral support and for helping me out so many times, from the training in the CMi to the calculations in the first drafts of the model of radiation enhanced oxidation. Thanks for always making our EPFL lab a happy and cosy environment.

This PhD experience would have not been the same without Jacopo. We not only shared friends, laboratories, groups, and flats between Lausanne and Ferney, but we also greatly collaborated professionally in the first designs of the vacuum transistor and in the development and tests of the first micro beam-profile-monitors for IRRAD. I will be always grateful for your help in mastering the cleanroom skills as well as your professional and personal support.

I would also like to express my gratitude to my parents Sasha, Tania, and my sister Natasha for your moral support, warm encouragements and for cheering for me till the end of this adventure. For you and for Anna and Luigi I will always be the zio stupidino no worries, but now with a PhD.

It goes without saying that I would not be who I am without all the great people that I have bonded with during these golden years of my life adventure.

I would need to devote a paragraph for each of you, but let me try to squeeze it out in a short, but extremely dense list: my Lupini in Legnano, doctors in Ferrara, the collegiali divini in Pavia (with soon to marry vulvix in Cambridge), the imec crew in Leuven now spread from Shanghai to Luxembourg, the norwegians emigrated back to Oslo, the italian mafia growing in Lausanne and spreading from Annecy to Solothurn, the polish mafia across europe from Geneva to Krakow, the lovely pucikflorciu and Madzia in Jaslo, and the swiss friends in Zurich.

To all of you, a huge thanks for the support in these years of PhD and the great time together. Please be patient with the social distancing, we will soon meet not only digitally, but in an old fashion analog way and celebrate together as required by the occasion (→ with Soplica).

Abstract

The Future Circular Collider (FCC) is the envisioned particle accelerator to be installed in the Geneva area (Switzerland). It could achieve an energy of 100 TeV by colliding proton beams (FCC-hh) travelling through a 100 km tunnel. Unprecedented radiation levels inside the FCC detectors will presumably exceed several tens of MGy with more than 10^{17} particles/cm². Current solid-state dosimetry technologies based on silicon, are not capable of withstanding such radiation, thus requiring a new type of sensor to be used as dosimeter in the future irradiation facilities and, at a later stage, in the accelerator itself.

The aim of this thesis is to develop a Radiation Dependent Resistor (RDR) as novel candidate technology for ultra-high radiation monitoring, and to study the radiation effects that are responsible for the measured increase of resistance of the RDR.

Following theoretical and experimental selection processes, copper was chosen as the best candidate material as thin film for the active layer of such radiation sensor. Such approach was never attempted before.

The RDR was developed via four experimental phases each including: the micro-fabrication at the CMi Center of MicroNanoTechnology (EPFL), the irradiation tests with protons at the IRRAD Proton Facility (CERN) and neutrons at the TRIGA nuclear reactor (Jožef Stefan Institute), and the characterisation at CERN and EPFL. As result, the RDR was fully prototyped with an optimized process flow, a compact chip layout, a radiation hard Printed Circuit Board (PCB), and an online and remote readout system.

By analyzing the electrical data and cross-sectional images of the irradiated samples, the conventional theory of high-temperature copper oxidation has proven useful in proposing a new concept of room temperature oxidation which is considerably amplified by radiation (Radiation Enhanced Oxidation). This new interpretation has been implemented in behavioural, analytical and empirical models and validated against experimental data.

Through the knowledge gathered in the framework of this thesis, the RDR technology was demonstrated to be compatible with the radiation levels expected in high energy physics experiments such as the HL-LHC and FCC. Additionally, these copper RDR sensors could also be used as dosimeters in particularly radioactive environments such as nuclear and fusion reactors.

Key words: *CERN, Future Circular Collider, radiation effects, radiation monitoring, sensors, Radiation Dependent Resistor, Radiation Enhanced Oxidation, copper, thin films, oxidation processes.*

Résumé

Le Future Circular Collider (FCC) est le nouvel accélérateur de particules qui devrait être installé dans la région de Genève (Suisse). Il pourrait permettre d'atteindre une énergie de 100 TeV en faisant entrer en collision des faisceaux de protons (FCC-hh) circulant dans un tunnel ayant un périmètre de 100 km. Les niveaux de rayonnement sans précédent à l'intérieur des détecteurs du FCC dépasseront probablement plusieurs dizaines de MGy avec plus de 10^{17} particules/cm². Les technologies actuelles de dosimétrie à l'état solide, basées sur le silicium, ne résistent pas à de telles doses de rayonnement. Celles-ci nécessitent un nouveau type de capteur qui soit adapté pour les mesures de dosimétrie dans ces futures installations d'irradiation et, à un stade ultérieur, pour les mesures dans l'accélérateur lui-même.

L'objectif de cette thèse est donc de développer une résistance électrique dont la valeur dépend de l'effet cumulatif du rayonnements (RDR). Il s'agit d'une nouvelle technologie qui permettrait de contrôler les rayonnements de très haute intensité et d'étudier le mécanisme sous-jacent qui gouverne l'augmentation de la résistance de la RDR sous l'influence de l'irradiation. Suite à des analyses basées sur des études théoriques et expérimentales, le cuivre a été retenu comme le matériau de choix. Dans notre approche, il sera utilisé en couche mince pour réaliser la zone active du capteur de rayonnement, ce qui n'a jamais été réalisé auparavant. Le RDR a été développé au cours de quatre phases expérimentales comprenant chacune diverses étapes : la microfabrication au Centre de MicroNanoTechnologie CMi (EPFL), les essais d'irradiation avec des protons à l'installation de protons IRRAD (CERN) et avec des neutrons au réacteur nucléaire TRIGA (Institut Jožef Stefan), et finalement les caractérisations électriques et structurales réalisées au CERN et à l'EPFL. Le RDR a été entièrement prototypé en suivant un flux de processus optimisés et intégrés de façon compacte sur puces, elles-mêmes combinées sur un support de circuit imprimé (PCB) résistant aux rayonnements et muni d'un système de lecture en ligne et à distance. En analysant les données électriques et les images de coupes transversales des échantillons irradiés, la théorie conventionnelle de l'oxydation du cuivre à haute température s'est avérée utile pour proposer un nouveau concept d'oxydation à température ambiante qui est considérablement amplifiée par le rayonnement (Radiation Enhanced Oxidation). Cette nouvelle interprétation a été implémentée dans des modèles comportementaux, analytiques et empiriques, et validée par rapport à des données expérimentales. A travers les connaissances recueillies dans le cadre de cette thèse, nous avons démontré que les prototypes réalisés sont compatibles avec les niveaux de rayonnements attendus dans les expériences de physique des hautes énergies du HL-LHC et FCC. De façon prospective, ces RDR en cuivre pourraient également être utilisés comme dosimètres dans des environnements particulièrement radioactifs tels que les centrales nucléaires et à fusion.

Mots clefs : CERN, Future Circular Collider, effets des rayonnements, capteurs, Radiation Dependent Resistor, Radiation Enhanced Oxidation, cuivre, couches minces, processus d'oxydation.

Sintesi

Il Future Circular Collider (FCC) è il nuovo acceleratore di particelle che potrà esser costruito nei pressi di Ginevra (Svizzera). Al suo interno si prevedono energie di 100 TeV ottenibili facendo scontrare fasci di protoni (FCC-hh) che viaggiano attraverso un tunnel lungo 100 km. I livelli di radiazione all'interno dei rilevatori FCC supereranno probabilmente diverse decine di MGy con più di 10^{17} particelle/cm² raggiungendo livelli senza precedenti. Le attuali tecnologie di dosimetria allo stato solido, basate sul silicio, non possono resistere a tali livelli di radiazioni. L'obiettivo di questa tesi è quindi di sviluppare una resistenza elettrica il cui valore dipende dalla radiazione accumulata (RDR), e lo studio del meccanismo sottostante che regola l'aumento della resistenza dell'RDR sotto l'influenza delle radiazioni. A seguito di analisi basate su studi teorici e sperimentali, il rame è stato selezionato come miglior materiale da usare come film sottile per lo strato attivo di tale sensore di radiazione.

. Questo apporto non è mai stato provato prima.

L'RDR è stato sviluppato in quattro fasi sperimentali, ognuna delle quali comprende varie tappe: microfabbricazione presso il Centre of MicroNanoTechnology CMi (EPFL), test di irraggiamento con protoni presso il centro IRRAD (CERN) e con neutroni presso il reattore nucleare TRIGA (Istituto Jožef Stefan), ed infine le caratterizzazioni elettriche e strutturali effettuate presso il CERN e l'EPFL. L'RDR è stato completamente prototipato utilizzando un processo ottimizzato e integrato in modo compatto su chip, che sono stati combinati su un circuito stampato (PCB) resistente alle radiazioni e dotato di un sistema di lettura online e a distanza. Analizzando i dati elettrici e le immagini trasversali dei campioni irradiati, la teoria convenzionale dell'ossidazione del rame ad alta temperatura si è dimostrata utile nel proporre un nuovo concetto di ossidazione a temperatura ambiente che viene notevolmente amplificato dalla radiazione (Radiation Enhanced Oxidation). Questa nuova interpretazione è stata implementata in modelli comportamentali, analitici ed empirici e validata a fronte di dati sperimentali. Attraverso le conoscenze raccolte nell'ambito di questa tesi, abbiamo dimostrato che i prototipi realizzati sono compatibili con i livelli di radiazione previsti negli esperimenti di fisica delle alte energie HL-LHC e FCC. Inoltre, questi sensori RDR in rame potrebbero anche essere utilizzati come dosimetri in ambienti particolarmente radioattivi come le centrali nucleari e a fusione.

Parole chiave: CERN, Future Circular Collider, effetti delle radiazioni, monitoraggio delle radiazioni, sensori, Radiation Dependent Resistor, Radiation Enhanced Oxidation, rame, film sottili, processi di ossidazione.

Contents

Acknowledgements	i
Abstracts (English, Italiano, Français)	iii
1 Introduction	1
1.1 Motivation and Aim of This Study	4
1.2 Thesis Outline	5
2 Radiation Damage and Dosimetry Techniques	7
2.1 Radiation Quantities and Effects	8
2.2 Radiation Environment in the FCC	10
2.3 Dosimetry Techniques	13
2.3.1 FCC-driven dosimetry requirements	14
2.4 Radiation Damage on Metals	16
2.5 New Dosimeter Concept	18
2.5.1 Material Selection	18
2.5.2 Radiation Damage Simulations	21
3 Experimental Equipment and Methods	23
3.1 Irradiation Facilities	24
3.1.1 Irradiation Facilities at CERN	24
3.1.1.1 CERN Irradiation Facilities Upgrades Required for FCC	26
3.1.2 Deployed Irradiation Facilities	28
3.1.2.1 CERN IRRAD Proton Facility	28
3.1.2.2 JSI TRIGA Nuclear Reactor	31
3.1.2.3 LHC Neutron Absorber (TAN)	32
3.2 Characterization Methods	34
3.2.1 Tools for Electrical Characterization	34
3.2.2 Scanning Electron Microscope for Morphological Characterization	37
3.3 Radiation Hard Tools for Ultra-High Radiation Tests	38
3.3.1 Printed Circuit Boards	38
3.3.2 Materials for Sample Holders	41
4 Experimental Runs	43
4.1 Summary of Experimental Runs	45
4.2 First Experimental Run: <i>Cr RDR (with Cr pads) in IRRAD</i>	46
4.2.1 Description	46

Contents

4.2.2	Material	46
4.2.3	Layout	47
4.2.4	Readout	48
4.2.5	<i>First Experimental Run - Results</i>	48
4.3	Second Experimental Run: <i>Cr RDR (with Al pads) in IRRAD</i>	50
4.3.1	Description	50
4.3.2	Material	50
4.3.3	Layout	51
4.3.4	Readout	52
4.3.5	<i>Second Experimental Run - Results</i>	52
4.4	Third Experimental Run: <i>Cr/Cu/Al RDRs in JSI/LHC/IRRAD</i>	53
4.4.1	Description	53
4.4.2	Material	54
4.4.3	Layout	55
4.4.4	Readout	56
4.4.5	<i>Third Experimental Run - Results</i>	59
	4.4.5.1 <i>JSI-1 Experiment Results</i>	59
	4.4.5.2 <i>LHC-TAN Experiment Results</i>	62
	4.4.5.3 <i>IRRAD-1 Experiment Results</i>	64
	4.4.5.4 <i>Third Experimental Run - Results Summary</i>	66
4.5	Final Experimental Run: <i>Cu RDR with SiO₂ in JSI&IRRAD and SEM</i>	67
4.5.1	Description	67
4.5.2	Material	68
4.5.3	Layout	68
4.5.4	Readout	69
4.5.5	Irradiation Tests Results	72
	4.5.5.1 <i>JSI-2 Experiment Results</i>	72
	4.5.5.2 <i>IRRAD-2 Experiment Results</i>	73
4.5.6	Morphological Analysis	74
4.5.7	<i>Final Experimental Run - Results Summary</i>	77
5	Models for the Radiation Enhanced Oxidation of Copper RDRs	79
5.1	Behavioral Model	80
5.2	Analytical Model	82
5.3	Empirical Model	83
5.4	Dosimeter Calibration Steps and Model Validation	85
6	Conclusions and Perspectives	89
6.1	Conclusions	90
6.2	Future Work	94
6.3	Perspectives	95
A	Irradiation Facilities Database	97

B Materials for Sample Holders	99
C Copper Expansion during Oxidation	105
D Non-linear Model for the Radiation Enhanced Oxidation	107
E RDR Process Flow	109
Bibliography	117
Glossary	119
List of publications	123
Curriculum Vitae	125

INTRODUCTION

The European Organization for Nuclear Research (CERN), founded in 1954 on the Franco-Swiss border near Geneva, is the world's largest particle physics laboratory. Today CERN hosts a complex system of interconnected particle accelerators that allow to achieve collisions at energies unreachable in any other place in the world. Thanks to the state-of-the-art experiments developed by an international community of scientists, groundbreaking discoveries were made increasing our knowledge on the sub-nuclear particles and their interactions. The latest major machine that started its operation in 2008 is the Large Hadron Collider (LHC). With its 27 km long ring, the LHC can accelerate particles to an energy of 7 TeV per beam, thus achieving collisions at 14 TeV.

In 2012, thanks to the LHC, the matrix of particles and interactions constituting the *Standard Model*, has been expanded by identifying a new particle whose behavior, interaction and decay, follows the theory published in 1964 [1] of the Higgs boson.

After this announcement, the LHC has continued its operation by yearly increasing its luminosity (rate of collision events) in order to collect more statistically accurate measurements of the Higgs boson. In fact the production of Higgs bosons requires not only very high collision energies, but also, due to its relatively small cross section (likelihood of interaction), it requires to record a large number of collisions. For this reason, CERN is currently updating the LHC into its next phase: the High Luminosity LHC (HL-LHC). While maintaining the same 27 km long tunnel, the HL-LHC will have more powerful magnets allowing it to increase the number of particles per spill, thus increasing the luminosity. Moreover, thanks to the updated and faster detectors, it will be possible to trigger the electronics at a faster rate thus increasing the possible amount of recorded data.

While the HL-LHC will provide a more precise platform to further study the Higgs boson, a completely new machine will be required to explain observations such as the evidences of the *dark matter*, and the prevalence of matter over *antimatter*. This is why CERN and the worldwide physics community, is discussing what will be the next generation accelerator and where it will be built.

Among the most ambitious projects there are two proposed machines: the Circular Electron-Positron Collider (CEPC) to be built at Beijing's Institute of High Energy Physics (IHEP) in China [2], and the Future Circular Collider at CERN [3]. Both accelerators are envisioned to be installed in a 100 km long tunnel, and to include intermediate steps: first a lepton collider (electron/positron) with the CEPC at IHEP and FCC-ee at CERN. Then to a hadron collider (proton/proton), with the Super proton-proton Collider (SppC) at IHEP and FCC-hh at CERN.

Chapter 1. Introduction

Both machines are targeting to achieve collision energies around 100 TeV (with their hadron versions), thanks to the upgraded magnets and the very long 100 km ring. As example, the planned layout of the path proposed for the FCC intercepting the current LHC is shown in Figure 1.1.

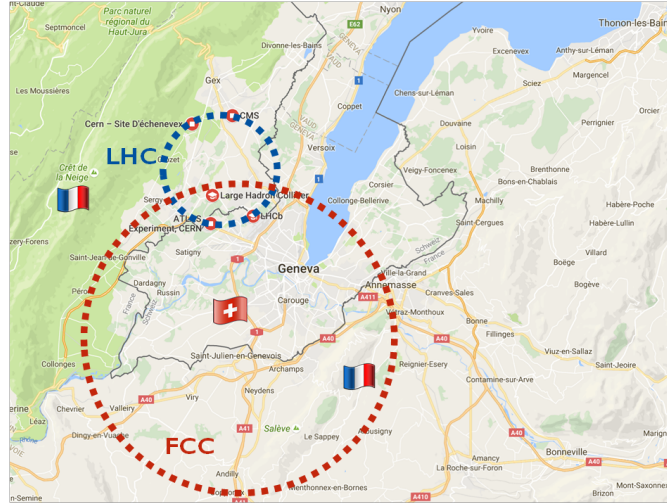


Figure 1.1 – Projection of the proposed "lakeside" location for the 100 km long FCC ring, intercepting the LHC. (Google Maps ©)

Given the extremely high cost of digging such a long tunnel, the CEPC and the FCC are likely to be mutually exclusive projects, but the challenges and technologies that need to be developed are in common to both projects. For this reason, CERN has established a feasibility study across an international community, independently on where such machine would be built, to address the technical aspects of such a next-generation accelerator by:

- Setting the main targets for the different FCC machines (FCC-ee, FCC-hh);
- Defining the performance goals for the accelerator and experiments;
- Investigating the existing state-of-the-art technologies and identify the required key R&D goals.

With respect to the latter point, many key R&D projects have been identified such as new superconducting magnets to reach 16 Tesla magnetic fields, new high power RF-cavities at 100 MW, more efficient cryogenic systems, new advanced detector technologies, new dosimetry systems, as well as new techniques and procedures for the Radiation Hardness Assurance (RHA).

Particle accelerators generate a great amount of radiation in the proximity of the interaction points, as well as along the whole accelerator ring. The absolute levels of radiation vary greatly across different sections of a particle collider, but do always pose a challenge for any system, device or material that will be located in such radioactive environment. In general, as higher

the rate of collision within the interaction point the higher will be the accumulating exposure to radiation of the elements surrounding it. Similarly, the higher the energy of the accelerated particle, the greater will be the radiation released in the tunnel as well as the broader will be the particle shower generated after each collision.

As schematized in Figure 1.2 with each major upgrade, going from LHC to HL-LHC and then through the different options of the FCC (with low and high luminosity), due to the increase of the target energy and luminosity a significant rise is expected in the radiation levels (expressed as particle fluence (Φ) and total ionizing dose (TID)), thus setting exponentially increasing challenges.

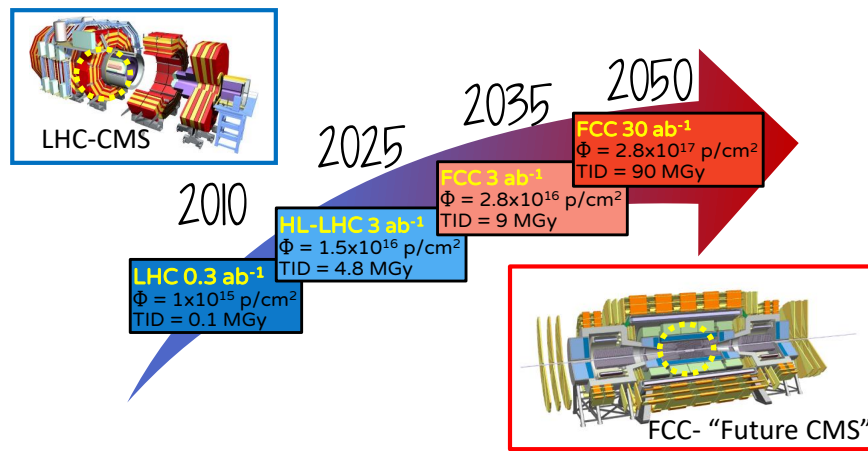


Figure 1.2 – Simulated particle fluence (Φ) and total ionizing dose (TID), integrated over 10 years, in the inner detectors for different upgrade runs and luminosity (in yellow) of CERN accelerators.

Two complementary approaches can be implemented to cope with this increasing radiation levels. Firstly, the dangers of radiation-induced failures can be removed or mitigated by wisely positioning critical equipment in less radioactive areas, and/or by installing proper shielding where possible. Secondly, specific fault tolerant and radiation resistant electronics and equipment can be designed, or, when possible, use of off-the-shelf components (COTS) which performance in a radioactive environment has been a priori characterized and validated. For this latter step, established RHA procedures allow to have a common qualification process adapted to the specific needs of the experiments, ensuring that the selected electronics and materials can keep their design specifications even after exposure to the radiation in the collider environment.

For that reason, similarly to the RHA procedures established for the LHC, a new RHA program for the FCC (Special technologies - Work Package 11) was started with the aim to update the currently used LHC measures and adapt them to the more challenging FCC. The following main tasks were considered within the FCC Special Technologies work package:

- *TASK 1 - Field conditions and radiation levels at FCC:* evaluate the radiation environments in the FCC tunnel and experiments, and provide best layout options with optimized shielding for the different sections of the FCC.
- *TASK 2 - FCC Qualification Protocols:* define an updated set of qualification protocols and evaluate the shortcomings and possible upgrades of current CERN irradiation facilities and testing infrastructure.
- *TASK 3 - Equipment needs for the accelerator, particle detectors and service systems:* identify which technologies will be used in the FCC and propose RHA strategies to cope with the radiation levels they will be exposed to.
- *TASK 4 - State of the art and development efforts on radhard components for HL-LHC:* continue the ongoing development of radiation-hard technologies for the High-Luminosity LHC project, and increase its potential to match the FCC requirements.
- *TASK 5 - New Technologies:* identify the challenges and technological showstoppers and develop new FCC-compatible technologies.

The main results from this work package have been collected and published in the conceptual design report (CDR) submitted in January 2019 to the European Union [4]. In particular this thesis contributed with inputs covering the Task 2 by studying the irradiation tests facilities currently available at CERN and proposing FCC-driven upgrades, and Task 5 by researching a novel dosimetry technique for ultra-high radiation monitoring and providing a concrete proposal on a new radiation sensor based on metal thin films.

1.1 Motivation and Aim of This Study

Every material, device, or system that is placed in a radiation environment is inevitably subject to several radiation triggered effects, that may affect their functionality during the experiment lifetime. In order to guarantee a radiation-hard design and build models to predict radiation induced failures, specific irradiation tests must be performed in similar radioactive environments. While many effects of radiation are known and can be simulated, irradiation tests are still necessary to experimentally assess the correct functionality and endurance of a device or system at the radiation rates and levels expected. For this scope different types of irradiation facilities have been built to provide infrastructures to reproduce such radiation environments as well as allowing for accelerated tests of multiple components. Moreover, during the irradiation tests, but also during the operation of a system, dedicated dosimetry devices are required to measure and monitor the radiation levels.

With the upcoming HL-LHC upgrade and possible greater machines like the FCC, special test facilities and dosimetry technologies will be required to match the expected higher levels of radiation. This thesis project was focused on the FCC-driven requirements for irradiation facilities and dosimeters, with the main objectives summarized as following:

- Analysis of the usability of current dosimetry techniques, irradiation facilities, materials,

methods and related limitations;

- Research of a novel approach and technology for ultra-high radiation monitoring (up to FCC-levels), with extensive tests and characterization in different types of radiation environments.
- Development of a prototype of working sensor, providing models that explain and predict its functioning in an ultra-high radiation field.

1.2 Thesis Outline

The thesis is organized as follows:

Chapter 2 provides an introduction of the basic radiation quantities and describes the radiation environment in the current Large Hadron Collider at CERN as compared to the extreme radiation levels expected in the Future Circular Collider. Afterwards, a list of the currently available radiation monitoring technologies is provided, highlighting their limitations with respect to the identified FCC-driven requirements, thus justifying the need of a novel solution. After, a literature review on known radiation effects on metals is given, justifying the choice to proceed with the study of such novel dosimetry technology based on thin metal films. Finally the Radiation Dependent Resistor is introduced as new dosimeter concept and the motivations behind the material selection are given.

The equipment and radiation testing methods are described in **Chapter 3**. First the test facilities, where the irradiation experiments were performed, are described, and then the tools used for the electrical and morphological characterizations are detailed. Finally a list of the different solutions that were developed to meet the stringent requirements and challenges of testing at extreme radiation levels are shown and discussed.

The experimental part is reported in **Chapter 4**. The four experimental runs are enlisted and described. The irradiation tests results are discussed for each phase, concluding with the set of electrical and morphological characterizations that allowed to identify a radiation-enhanced oxidation as working principles of the copper Radiation Dependent Resistor.

In **Chapter 5** the results from the experimental runs are used to model the radiation-enhanced oxidation. First a behavioral model is given to relate the standard copper oxidation at different atmospheric conditions, with a radiation triggered oxidation. Then an analytical model is proposed to mathematically describe the growth of copper oxide as dominated by the integrated particle fluence, followed by an empirical model to predict the increase of resistance of an RDR when exposed to radiation, providing a unique lumped coefficient accounting for the radiation-enhanced oxidation.

Finally **Chapter 6** summarizes the conclusions of this thesis, provides suggestions for future experimental work, and explores the possible future applications for the Radiation Dependent Resistor technology.

RADIATION DAMAGE AND DOSIMETRY TECHNIQUES

This chapter introduces the main quantities and units related to radiation that are used in this thesis.

Next, the different radiation environments in the current Large Hadron Collider (LHC) and its foreseen upgrades including the Future Circular Collider (FCC), are discussed in terms of the extreme radiation challenges.

Afterwards, the different types of currently used technologies for radiation monitoring are given, detailing their limitations with respect to the identified FCC-driven requirements.

Following, an overview of the main radiation effects in metals described in literature justifying the choice of metals as potential active layer of a novel dosimetry technology.

Finally, the material selection discussion and the radiation damage simulations are described.

Contents

2.1 Radiation Quantities and Effects	8
2.2 Radiation Environment in the FCC	10
2.3 Dosimetry Techniques	13
2.3.1 FCC-driven dosimetry requirements	14
2.4 Radiation Damage on Metals	16
2.5 New Dosimeter Concept	18
2.5.1 Material Selection	18
2.5.2 Radiation Damage Simulations	21

2.1 Radiation Quantities and Effects

Several units and standards are defined by the International Systems of Units (SI) to describe the different physical quantities connected with radiation. In this thesis, the quantities *Energy* and *Luminosity* are used to quantify the performance of different particle accelerators, while *Dose* and *Particle Fluence* are used to quantify the ionizing and non-ionizing effects of radiation on matter. These quantities are described in the following paragraphs.

Energy

In the context of particle accelerators, the maximum achievable energy or the highest achievable collision energy, is a common figure of merit used to compare different accelerator machines. This value is measured in electron volt eV which is the energy gained by the charge of one electron under the effect of a potential difference of one volt. In particle colliders, energy is transferred to the accelerating particles by means of strong radio-frequency (RF) cavities, finally reaching the desired levels for the specific application. For example, the LHC accelerates particles up to 7 TeV achieving proton-proton collisions at 14 TeV. Producing collisions at higher energy levels allows to explore different ranges of particle masses, thus allowing the discovery of new constituents of matter.

Luminosity

In accelerator physics, the luminosity L is the ratio between the number of meaningful events (particle interactions N) per unit time over the cross section (likelihood of such interaction to occur σ):

$$L = \frac{1}{\sigma} \frac{dN}{dt} \quad [cm^{-2}s^{-1}] \quad (2.1)$$

Luminosity has the dimensions of events per area and unit time, and can also be expressed in *barns* per second $b^{-1}s^{-1}$ (barn is a unit of area equal to $10^{-28} m^2$). Integrating the luminosity over the time (e.g. 10 years lifetime of a particle accelerator experiment) gives the integrated luminosity L_{int} (or just L) used to describe the performance of a particle accelerator. For a given luminosity, known the energy, size, and angle of the two colliding particle beams, as well as their rate of collision, is possible to trace back the number of particle collisions. For example, in the LHC, a luminosity of $1 fb^{-1}$ ($10^{-43} m^2$) [5] is equivalent to approximately 10^{14} proton-proton collisions.

Dose and Total Ionizing Dose

The dose D , is a measure of kinetic energy released by a particle to a unit of mass and is defined as the mean energy transferred by a charged particle dE to the medium, per unit of mass dm :

$$D = \frac{dE}{dm} \quad [Gy] \quad (2.2)$$

The unit of absorbed dose is joule per kilogram, and the SI unit of absorbed dose is the Gray (Gy), where $1 \text{ Gy} = 1 \text{ J/Kg}$.

The absorbed dose depends on the specific material being subject to the ionizing radiation, therefore the dose D is often followed by the name of the material as for example Gy(air), Gy(SiO₂), etc. In this thesis, the absorbed dose is usually expressed as Gy in silicon (Si) and when considering the radiation effects on electronics is quantified in terms of total ionizing dose (TID). The TID is defined as the integral of the energy deposited in matter through ionizing processes. These can be triggered by electromagnetic interactions of high-energy photons (e.g. x-rays and γ -rays), or by the release of energy by particles such as electrons and positrons along their interaction tracks [6, 7]. In electronics, accumulating TID can induce permanent charging effects in the oxides of the circuitry (gates, insulators, etc.), leading to loss of performance, or even permanent failure.

An additional effect induced by ionizing radiation are Single Event Effects (SEE). These phenomena cover both destructive and non-destructive effects. In the first case, the local release of energy within a logic gate by an incident particle, determines a bit-flip or temporary saturation of the transistor (a soft-error or Single Event Upset), that requires issuing a reset or rewrite in order to recover the chip. In the second case of destructive effects, the energy released locally can build up current paths which in turn can evolve in a burn-out of the chip due to latch-up.

Particle Fluence and Displacement Damage

The particle fluence Φ , is the ratio between the number of particles dN intersecting the cross-sectional area of a sphere dA :

$$\Phi = \frac{dN}{dA} \quad [cm^{-2}] \quad (2.3)$$

The particle fluence rate per unit time ϕ (or flux), is expressed as:

$$\phi = \frac{d\Phi}{dt} \quad [cm^{-2}s^{-1}] \quad (2.4)$$

where $d\Phi$ is the increment of particle fluence in the time interval dt .

Practically, the quantities Φ and ϕ , are often expressed for a particular type of particle, and energy. In the context of this thesis, the following units are used:

- *Total 23 GeV proton fluence*: integral of the total number of protons at 23 GeV crossing the area dA , expressed as $p_{23\text{GeV}}/\text{cm}^2$, or simply as p/cm^2 .
- *Total Neutron fluence*: integral of the total number of neutrons at any energy crossing the area dA , expressed as n_{tot}/cm^2 , or simply as n/cm^2 .
- *Total High Energy Hadrons (HEH) fluence*: integral of the total number of hadrons (subatomic composite particles as baryons (e.g. protons, neutrons) and mesons (e.g. pions, kaons)) at any energy crossing the area dA , expressed as p_{HEH}/cm^2 .

Particle fluence is responsible for the displacement damage (DD), which is directly connected to the total non-ionizing energy loss (NIEL).

The release of non-ionizing energy is quantified by means of displacements per atom (DPA) which represents the ratio between the number of atoms displaced from their normal lattice sites as a result of a given number of bombarding charged (protons) or not-charged (neutrons) particles [6, 7], and the total number of atoms. In electronics, increasing DD leads to an increase of the bulk resistivity (or varies the doping) impacting the silicon performance and leading to failures.

2.2 Radiation Environment in the FCC

The radiation environment encountered in high energy particle accelerators, as the current LHC and future FCC, differs completely from the one found in medical applications or in space. In fact in particle accelerators a mixed radiation field is generated, composed of neutrons, photons and charged hadrons. Such complex and very intense radiation environment is due to sub-particle showers generated by the proton-proton collisions occurring inside the detectors, and also due to the highly energetic particles circulating along the accelerator ring. This mixed radiation field is responsible for the damage to equipment and detectors that consequently suffer a diminution of performance over time, or can even end up in dangerous failures, due to accumulation of ionizing and non-ionizing radiation.

As previously shown in Figure 1.2, and listed in Table 2.1 below, the consecutive upgrades from the LHC to the final version of the FCC, together with the increase of the machine performance in terms of maximum energy and achieved luminosity, will also lead to an increase of the maximum radiation levels (fluence and dose).

Machine	Collision Energy (TeV)	Luminosity (ab^{-1})	Fluence (p/cm^2)	Dose (MGy)
LHC	14	0.3	1.0×10^{16}	0.1
HL-LHC	16	3	1.5×10^{16}	4.8
FCC-hh	100	3	2.8×10^{16}	9
FCC-hh*	100	30	2.8×10^{17}	90

Table 2.1 – *Maximum levels of Fluence and Dose, integrated over 10 years of operation, within the inner detectors of current and future synchrotron machines at CERN (with FCC-hh* being the final high luminosity version of the FCC) [8, 9].*

While collision energies will rise of a factor of 7, luminosity is planned to rise by a factor of 100, resulting in an increase of several orders of magnitude of the radiation levels, as predicted with FLUKA (Monte Carlo simulator) [8, 9].

Figures 2.1 and 2.2 show these simulations performed after 10 years of operation inside the core of the massive FCC detector. The first Figure 2.1 displays the expected integrated dose in

the detector surrounding the particles crossing point ($Z=0$ is the collision center), with peaks reaching almost hundreds of MGy in different sections. The second Figure 2.2 displays the same detector cross section with the expected cumulative particle fluence, with locations reaching levels higher than 10^{17} n/cm².

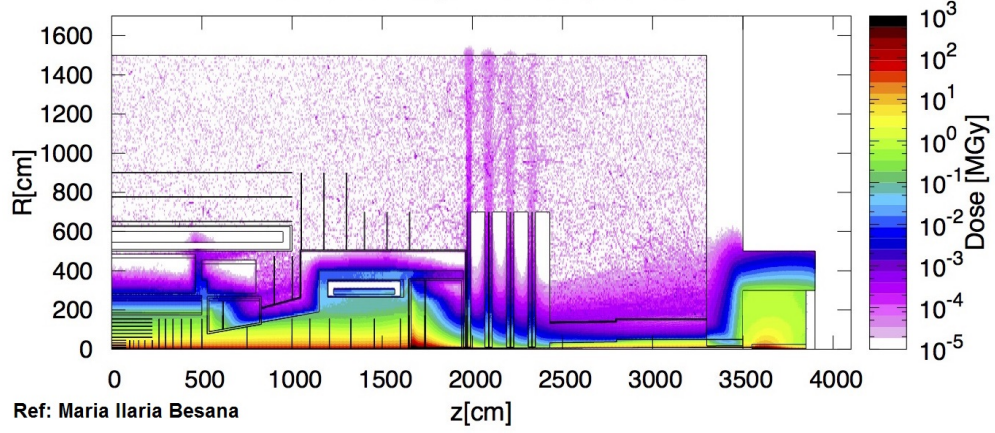


Figure 2.1 – FLUKA simulations of the expected cumulative dose in the core of a FCC detector after 10 years of operation.

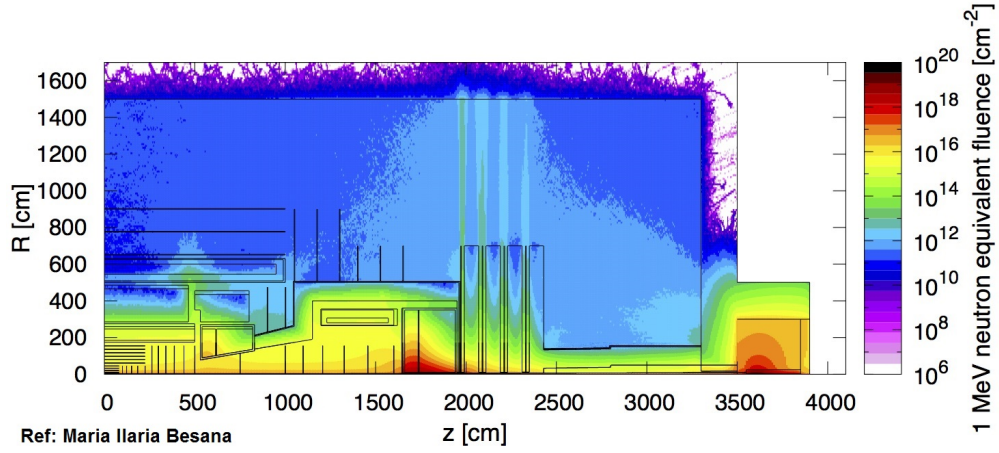


Figure 2.2 – FLUKA simulations of the expected cumulative particle fluence in the core of a FCC detector after 10 years of operation.

Figures 2.3 and 2.4 show the FLUKA simulations performed for 1 year of operation in one of the arc sections of the FCC ring. In this case, the radiation levels for both dose and particle fluence are more relaxed than the case of the FCC detector, but still hundreds of times higher than the equivalent arc section in the LHC.

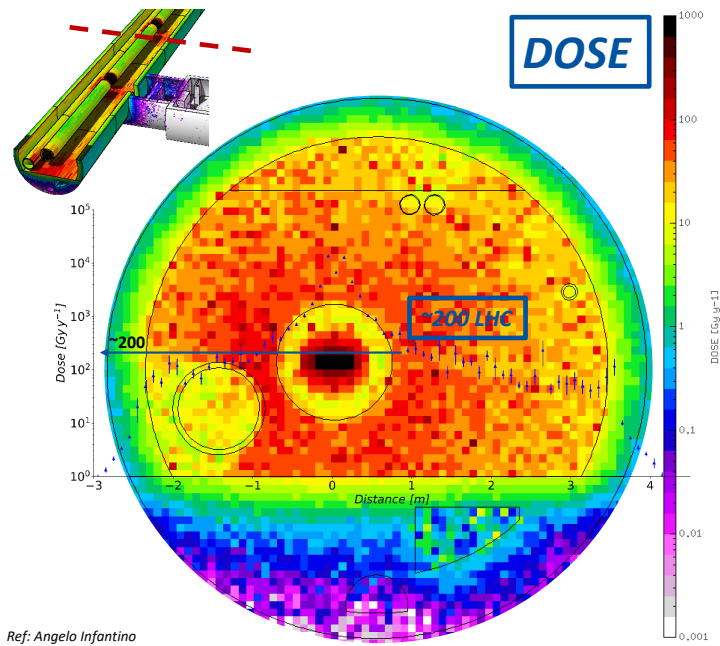


Figure 2.3 – FLUKA simulations of the expected cumulative dose over one year of operation, in the arc cross section of the FCC tunnel, showing a peak level 200 times higher than in the LHC.

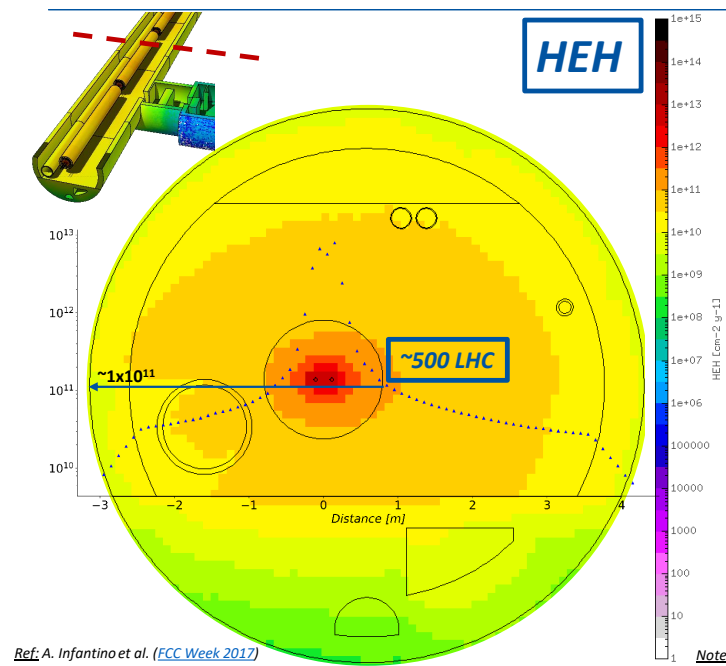


Figure 2.4 – FLUKA simulations of the expected cumulative particle fluence over one year of operation, in the arc cross section of the FCC tunnel, showing a peak level 500 times higher than in the LHC.

2.3 Dosimetry Techniques

Dosimeters are devices designed to detect and measure radiation directly or indirectly by relating a measurable quantity to the experienced radiation. Many different types of dosimeters are today available on the market, each with specific fields of application and range of usability. As part of the initial research of candidate technology for dosimetry at FCC radiation levels, the following technologies were analyzed:

- *Ionization Chambers*: gas filled cavities where the direct ionization of the gas due to incident radiation generates a current proportional to the dose rate. Chambers with different gas mixtures and size can provide different sensitivities with a common dynamic range up to 1 Gy/s [10]. An electrometer is required to measure the charge collected by the gas chamber over a fixed time interval.
- *Film Dosimetry*: special plastic materials which get polymerized upon exposure to radiation changing their optical absorbance at specific wavelengths. On the market there are different types of films with varying material composition and thicknesses, targeting different dynamic ranges. Gafchromic films (GaF) are usually used up to relatively low integrated doses (<1 kGy) [11], while other radiochromic films like the FWT can measure up to 200 kGy [12]. The readout of films is performed using densitometers, spectrophotometers or even scanners.
- *Luminescence Dosimetry*: special ceramic materials capable of absorbing radiation and consequently releasing it in form of light (phosphorescence). These devices come in different forms, shape and compositions depending on the target application and dynamic range. Optically Stimulated Luminescence (OSL) dosimeters allow dose measurements between few mGy to 100 Gy, while Thermoluminescent Dosimeters (TLD) and Radio-Photoluminescence (RPL) sensors can be used to measure doses from 0.1 Gy to 1 MGy [13]. The readout of a TLD requires to heat up the dosimeter to stimulate the phosphorescence, while an OSL requires an optical system to excite the ceramic (a laser) and detecting the resulting emitted light. Similarly a RPL requires an UV source for the excitation.
- *Plastic Scintillators*: similar to luminescence dosimeters where the energy absorbed from the incoming radiation is emitted as a light signal, but made of plastic. While TLD and OSL need an external stimuli to release the accumulated energy, in plastic scintillators the luminescence occurs during the irradiation, allowing to measure the dose rate (as for ionization chambers). Typical dynamic range is between dose-rates of 10 to 10^6 kGy/s [14, 15]. The readout is performed using a photomultiplier tube (PMT) which converts the emitted light into a readable electrical signal.
- *Polymer Alanine Dosimetry*: this technology is based on an amino acid (alanine) which forms stable free radicals when irradiated. Alanine dosimeters can be compressed in different tablets or pellets of different shape and size. The dynamic range of such dosimeter goes from few Gy to 100 kGy [16]. The readout is performed with a electron spin resonant spectrometer which allows to measure the concentration of the radicals.

- *Diamond Dosimetry*: these dosimeters exhibit a decrease of electrical resistivity proportional to the dose rate. This effect is due to the creation of electron-hole pairs and the drift of this charge towards the electrodes when applying a biasing voltage. Diamond dosimeters have an excellent radiation hardness up to the MGy level [17].
- *Fricke Dosimetry*: also known as ferrous sulfate dosimeters, in these devices the ionizing radiation induces an oxidation of ferrous ions into ferric ions. The total dose can be then obtained by measuring the increasing concentration of ferric ions by means of a spectrophotometer. The dynamic range of Fricke dosimeters can range from few Gy to 400 Gy [18].
- *Semiconductor Dosimetry*: these silicon based dosimeters are MOSFETs (or RadFETs) and pin diodes, used to measure ionizing and non-ionizing radiation respectively. These devices show an increase of threshold voltage (MOSFETs) or leakage current (diodes) proportional to the integrated radiation. The dimensions of the active layer (gate oxide, base length) determine the dynamic range, with RadFETs operating from few mGy to 100 kGy, and diodes measuring fluence from 10^8 to 10^{15} p/cm² [19]. The readout is performed electrically with a multimeter by sourcing a constant current and reading the developed voltage.

These technologies are evaluated upon the FCC-driven requirements as discussed in the next Section 2.3.1.

2.3.1 FCC-driven dosimetry requirements

The choice of a specific dosimetry technology depends on several factors that are strictly connected with the application. Unfortunately, there is no technology that can satisfy all the specifications at the same time.

For this reason, the following list of requirements were identified as key parameters for a sensor to be used during irradiation tests at FCC levels, and at the FCC tunnel and experiments:

1. *Dynamic range*: the technology has to cover the radiation levels expected in the FCC (shown in Table 2.1) covering up to the maximum expected integrated dose and fluence (over 10 years of operation) of 90 MGy and 2.8×10^{17} p/cm² respectively.
2. *Device lifetime*: the device has to be structurally able to withstand the extreme radiation environment without deterioration and, once installed in the FCC, without requiring a replacement during 10 years.
3. *Readout range*: the readout of the device has to be possible online and at a long distance (>100 m) with the minimum number of cables and connections.
4. *Readout technique*: the best readout technique can be considered an electrical for its easier implementation. Optical readout is less preferable due to the higher installation and equipment cost. Chemical readout is to avoid for difficult implementation in an online system.
5. *Device size*: the radiation sensor has to be easy to handle with dimensions smaller than

few mm³.

6. *Unit cost*: since the dosimeters will be installed in great number along the 100 km tunnel, cost should be in the range of few CHF/unit.

Figures 2.5-A and 2.5-B, display the dynamic range of some of the previously mentioned dosimeter technologies that are today used in the LHC, highlighting in yellow the areas of interest for the FCC, calling for a new class of MGy and Ultra-high-fluence dosimetry.

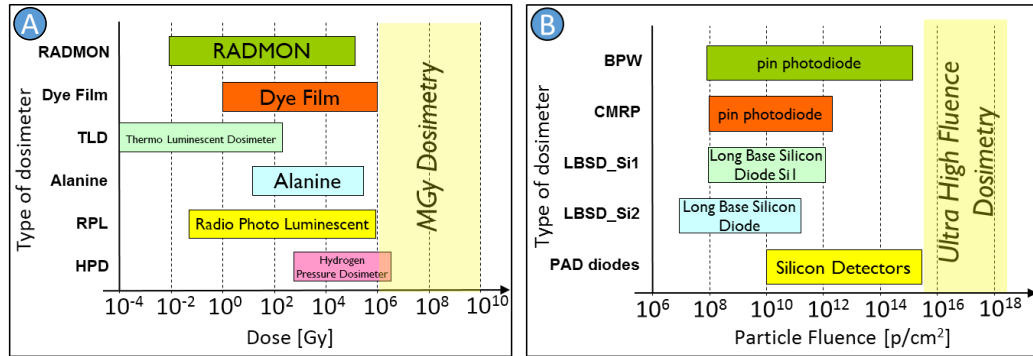


Figure 2.5 – List of currently available radiation sensors for dose monitoring (A) and fluence monitoring (B) with respect to their operational range, with highlighted areas for MGy Dosimetry and Ultra High Fluence Dosimetry.

Additionally, in the table below, each of the dosimetry technologies listed in the beginning of this Section 2.3, is rated against the FCC-driven requirements:

Dosimetry Technology	FCC device lifetime (>10 years)	Readout range (> 100m)	Readout technique (electrical)	Dynamic range (> MGy)	Device size (~mm)	Unit cost (<10 CHF/u)	Score
Ionization chamber	★★	★★★	★★★	★★	★	★	★
Film Dosimetry	★	★	★★	★	★★	★★★	★
Luminescence Dosimetry	★★	★★★	★	★	★★	★★	★
Polymer Alanine Dosimetry	★	★	★	★★	★★	★★	★
Plastic Scintillators	★	★★	★★★	★★	★★	★★★	★★
Diamond Dosimetry	★★★	★★★	★★	★★★	★★★	★	★★
Fricke Dosimetry	★★	★★	★	★	★	★★	★
Semiconductor Dosimetry	★★	★★★	★★★	★★	★★★	★★★	★★★

★ BAD ★★ MIDDLE ★★★ GOOD

Figure 2.6 – A taxonomy table of main dosimetry technologies with respect to their applicability in the FCC.

Thanks to this comparison table is clear how every dosimetry technology has some major advantages, but none of them scores a *good* rating in all the fields. Nevertheless,

semiconductor-based dosimeters (comprising RadFETs and pin diodes) have scored the best marks in most of the identified key parameters, thanks to the excellent readout range (>100 m), preferable readout technique (electrical) as well as optimal cost and device size. On the other hand, the "*FCC device lifetime*" and "*Dynamic Range*" are rated as *middle*, since RadFET and pin diode dosimeters suffer from the intrinsic limitations of silicon, becoming unusable due to the radiation induced defects (TID and DD) after being exposed for too long to radiation. Differently, diamond dosimetry show excellent performance in "*FCC device lifetime*" and "*Dynamic Range*", mainly because of the higher radiation hardness of carbon with respect to silicon.

While extending the research towards a diamond dosimeter for the FCC could have clearly brought to good results, the main limiting factor of diamond dosimetry, the extreme cost, violates another key parameter which is extremely important for a technology that will be exploited extensively during the irradiation tests and installed in great numbers within the 100 km long accelerator.

Following the results listed in Figure 2.6, the target for the new technology was to develop a dosimeter similar in the working principle to silicon based and diamond based dosimeters, but using a material more resistant to radiation than silicon and cheaper than diamond. As a result, it was chosen to explore a completely new class of materials as active layer of a potential FCC dosimeter: *metals*.

In fact, as will be detailed in the following Section 2.4, experimental results in literature have reported that metals show relatively good radiation hardness, but also display a measurable resistivity increase when exposed to high levels of radiation.

2.4 Radiation Damage on Metals

There are two main mechanisms in which radiation interacts with materials such as metals:

1. by releasing energy through ionization;
2. by means of elastic atomic collisions (primary knock-on atom) followed by a cascade of atomic displacements.

In the first case, through ionization, the interacting particle releases energy along its path generating electron-hole pairs. Differently from organic compounds in which chemical bonds get damaged (radiolysis), or from oxides where a charging effect occurs, in metals, ionizing radiation does not lead to any permanent effect since the released energy induces only a transient effect where the stripped electron (ionized) gets immediately replaced by another free-electron available in the conduction band of the metal [20].

In the second case, as schematized in Figure 2.7-A, the transfer of recoil energy by direct interaction with the metallic atom via displacement damage induces vacancies and interstitials. On the macro-scale, non-ionizing radiation can produce visible and measurable

changes, as for example the swelling of neutron-irradiated bar of steel [21] depicted in Figure 2.7-B, or the increase of resistivity of copper [22] plotted in Figure 2.7-C.

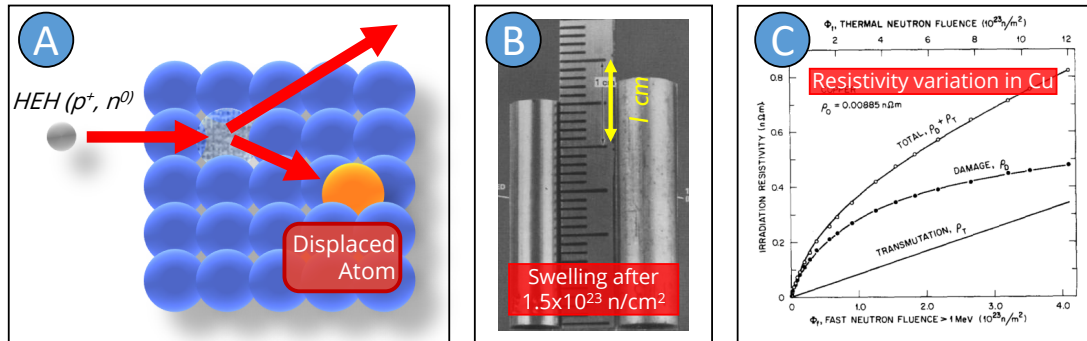


Figure 2.7 – A) Schematic view of a primary-knock-on-atom (displacement damage) induced by an incoming high energy hadron (HEH) like proton or neutron hitting the metal lattice and creating a local vacancy and interstitial. B) Example of swelling induced on a stainless steel bar by extreme neutron irradiation in a nuclear reactor [21]. C) Example of resistivity variation due to extreme neutron irradiation in a nuclear reactor, observed on a copper sample [22].

In fact, displacement damage in metals has been extensively studied in the past while developing materials and technologies for accelerator physics[23, 24, 25], nuclear power plants [26], and space applications [20].

In these publications different material properties are shown to change under the impact of very high radiation and can be enlisted as follows [27]:

- *Physical Properties:*
 - Decrease of thermal conductivity.
 - **Increase of electrical resistivity.**
- *Chemical Properties:*
 - Phase transformation in the metal.
 - Changes in the local chemical composition.
- *Mechanical Properties and Dimensions:*
 - Loss of ductility.
 - Hardening.
 - Swelling with creeps and fractures.
- *Transmutation products:*
 - Gas production (H, He) causing void formation, bubbling and embrittlement.

Among these effects, particular focus in this thesis was given to previous studies where change of electrical resistivity induced by radiation was observed and correlated with the number of vacancies and interstitials produced by the non-ionizing radiation [22, 28, 29].

Other work on radiation damage was also performed to study the conductivity stability in

commercial tantalum and nickel-chromium resistors in a neutron environment [30], and in a low energy proton environment on tantalum resistors [31]. In both studies some of the tested resistors were found to change their conductivity in a greater extent than other, attributing this difference to the type of resistor and variability in their fabrication.

It is important to notice that these literature works have all been performed on relatively large and thick metal samples (several cm^3 and with thicknesses $>100\text{ }\mu\text{m}$) and the change of resistivity was seen as material degradation leading to the unwanted properties changes previously listed.

On the other hand, the change of resistivity due to radiation is the core operating principle of the dosimetry technique presented in this thesis, and for this reason, as will be discussed in detail in the following chapters, the research was performed on different metals, micro-fabrication techniques, and form factors to shortlist the parameters that most affect the sensitivity to radiation at levels expected in the Future Circular Collider.

2.5 New Dosimeter Concept

Upon the evaluation of the existing dosimetry technologies enlisted in Figure 2.6, the target for a new dosimeter was set to develop a device similar in the working principle to silicon based and diamond based dosimeters, but using a material more resistant to radiation than silicon and cheaper than diamond, such as metals. In addition, as discussed in the literature review in Section 2.4, research has shown that among the radiation induced effects observed in metals, very high particle fluence was found to be responsible of measurable changes in the resistivity of certain tested metals.

This observation prompt to consider metals as promising material capable of relating radiation levels to a measurable electrical parameter as it is today for silicon-based technologies.

The proposed sensor, hereafter called Radiation Dependent Resistor (RDR), was made by sputtering thin layers of metal on silicon wafers and consecutive lithography and etching, into measurable resistive structures. The selected materials for the produced RDRs were aluminum, chromium and copper (see Section 2.5.1 below).

Such design was a result of several iterations that allowed to optimize the fabrication process, as well as the device sensitivity to radiation, and will be discussed in details in Chapter 4.

2.5.1 Material Selection

In order to select the most appropriate metal to be used as active layer of the Radiation Dependent Resistor, the following factors were taken into account:

- *Activation*: the metal should have a low activation (induced radioactivity) to reduce the exposure of the personnel handling the dosimeters after irradiation.
- *Availability*: only metals available as sputtering targets at the EPFL cleanroom were considered.
- *Adhesion Layer*: the metal for the active layer should adhere optimally to the oxidised silicon substrate without the need of complicated stacks.
- *Self-passivating*: the metal should not oxidise at ambient temperature.
- *Bonding*: the metal should allow direct wire bonding to an external support.
- *Cost*: the metal should be largely available to lower the final cost of the dosimeter.

In Figure 2.8 the dose rate of different materials exposed to one week of proton irradiation are plotted against their decay time. Additionally, in Table 2.9 the available sputtering targets at the EPFL Centre of Micronanotechnology (CMi) are enlisted.

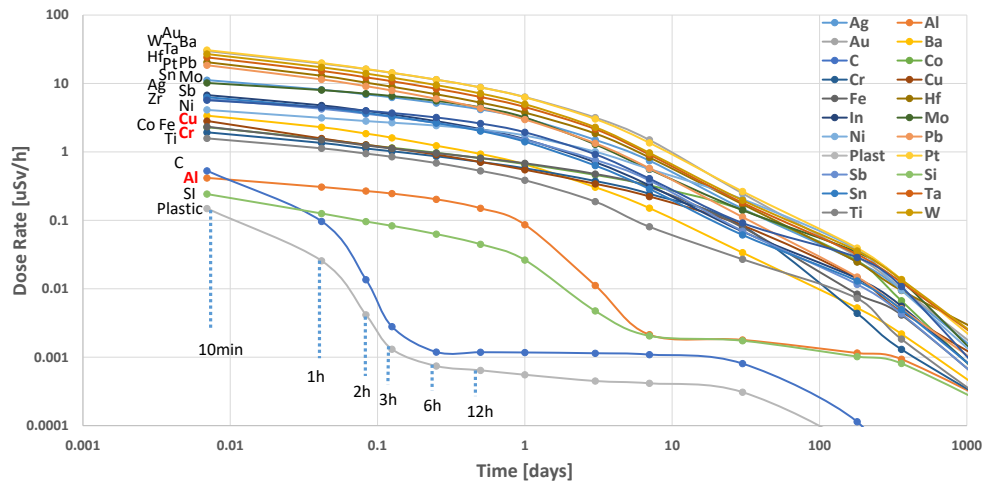


Figure 2.8 – Simulated dose rate decay in time of different materials irradiated for one week in IRRAD up to a total proton fluence of $5 \times 10^{15} \text{ p/cm}^2$ (by R. Froeschl).

Chapter 2. Radiation Damage and Dosimetry Techniques

N.	Material	Full Name	Sputtering Machine
1	Ag	Silver	DP 650
2	Al	Aluminium	SPIDER 600, DP 650
3	Au	Gold	DP 650
4	Cr	Chromium	DP 650
5	Cu	Copper	DP 650
6	Ge	Germanium	DP 650
7	Ir	Iridium	DP 650
8	Mo	Molybdenum	SPIDER 600, DP 650
9	Nb	Niobium	SPIDER 600
10	Pd	Palladium	DP 650
11	Pt	Platinum	SPIDER 600, DP 650
12	Ru	Ruthenium	SPIDER 600
13	Sb	Antimony	DP 650
14	Sn	Tin	DP 650
15	Ta	Tantalum	SPIDER 600, DP 650
16	Ti	Titanium	SPIDER 600, DP 650
17	W	Tungsten	SPIDER 600, DP 650

Figure 2.9 – List of targets available at EPFL-CMi for the Alliance-Concept DP650 and Pfeiffer SPIDER 600 sputtering machines.

A subset of metals was selected by considering these two first main criteria. The possible choices were then compared to each other in Figure 2.10, including the additional criteria previously listed:

Material	Full name	Activation after 1 week irradi.	Adhesion layer required	Self-passivating	Bonding	Cost	Score
Ag	Silver	★	★★★★★	★★★★★	★★★★★	★★	★★★★
Al	Aluminium	★★★★★	★	★★★	★★★★★	★★★★★	★★★★★
Au	Gold	★	★	★★★★★	★★★★★	★	★★★
Cr	Chromium	★★★★★	★★★★★	★★★★★	★	★★★	★★★★★
Cu	Copper	★★★	★	★★★	★★★★★	★★★★★	★★★★★
Ge	Germanium	★★★	★	★★	★	★★	★
Ir	Iridium	★	★★★★★	★★★★★	★	★	★★
Mo	Molybdenum	★★★	★	★★★	★	★★★	★★★
Nb	Niobium	★★★	★	★★★	★	★★★	★★★
Pd	Palladium	★★	★	★★	★	★★★	★
Pt	Platinum	★	★	★★★★★	★	★	★
Ru	Ruthenium	★★★	★	★★★★★	★	★	★★
Sb	Antimony	★★★	★	★★	★	★★★	★★★
Sn	Tin	★★★★★	★	★★	★	★★★	★★★★
Ta	Tantalum	★★	★	★★★★★	★	★★	★★
Ti	Titanium	★★★★★	★★★★★	★	★	★★★	★★★★
W	Tungsten	★	★	★★★	★	★★★	★

★ WORSE ★★ BAD ★★★ MIDDLE ★★★★ GOOD ★★★★★ BEST

Figure 2.10 – Metal selection scorecard.

From this analysis, three metals *chromium*, *aluminum*, and *copper* gained the highest score and were short-listed as optimal candidates for our application. These metals were chosen not only for their availability as targets for the sputtering machine, and for their relatively low level of induced radioactivity with respect to metals with higher atomic number, but also for their suitable properties for microfabrication, such as self-passivating, good adhesion with

SiO₂ covered substrate, bondability (Al on Cr for wire-bonding pads) and cost.

2.5.2 Radiation Damage Simulations

Before the realization of the first RDR prototypes, simulations were performed to assess the amount of displacement damage induced by extreme particle fluence in the different selected metals.

Popular simulators used for calculating the radiation-matter interaction, such as SRIM [32], could not be used due to their intrinsic limitation to ions of energies below 2 GeV, but also due to a non-convergence in targets where the nuclear interaction length is much larger than the target thickness. For these reasons, the FLUKA Monte Carlo tool [33, 34] has been used. The FLUKA scorecard used for the displacements-per-atom (DPA) calculation is DPA-SCO [35]. The DPA accounts for every atom displaced from its initial location in the lattice, due to a primary or secondary impinging particle which recoil energy is higher than the lattice binding energy.

To reach faster convergence of the simulation tool, the target was chosen with an area of 1x1 mm² with 100 µm thickness. Even if the designed RDRs have a larger area, the simulated DPA remains constant for varying x and y dimensions (section ortogonal to the beam) assuming a uniform distribution of the incident beam or irradiating field. Similarly, even if the designed RDR have thicknesses varying between 50 nm and 1000 nm, the simulated DPA can be considered independent on the thickness, since in these simulations only highly energetic particles are considered (thus having constant probability of interaction on targets with thickness much thinner than the interaction length of few cm [36]).

Table 2.2 lists these simulation results in terms of total DPA integrated over an irradiation period up to 10¹⁷ particles/cm² in the following different irradiation environments:

- *DPA by protons*: simulated using the parameters for the table *IRRAD 5* with the nominal beam at the IRRAD proton facility at CERN [37], described in Section 3.1.2.1. The resulting DPA first simulated per mono-energetic 23 GeV proton is reported in the table normalized to 10¹⁷ p₊/cm².
- *DPA by neutrons*: simulated using the parameters for the central irradiation channel of the JSI TRIGA nuclear reactor [38] running at full power, described in Section 3.1.2.2. The resulting DPA first simulated as flux over the high energy neutrons spectrum is reported as fluence normalized to 10¹⁷ n₀/cm².
- *DPA by mixed-field*: simulated using the nominal parameters of the LHC beam and the spectrum calculated within the Neutron Absorber installed at the LHC-point 1, described in Section 3.1.2.3. The resulting DPA first simulated over an LHC luminosity of 50 fb⁻¹ is reported on the table as fluence of high energy particles 10¹⁷ p_{HEH}/cm² considering an average fluence of ~10¹² p/cm² every 1 fb⁻¹;

Chapter 2. Radiation Damage and Dosimetry Techniques

Material	DPA Protons (DPA/ 10^{17} p ₊ /cm ²)	DPA Neutrons (DPA/ 10^{17} n ₀ /cm ²)	DPA Mixed Field (DPA/ 10^{17} p _{HEH} /cm ²)
Aluminum (Al)	0.75×10^{-4}	3.21×10^{-3}	3.80×10^{-2}
Chromium (Cr)	2.61×10^{-4}	1.91×10^{-3}	3.00×10^{-2}
Copper (Cu)	3.85×10^{-4}	1.74×10^{-3}	2.80×10^{-2}

Table 2.2 – DPA simulations for a $1 \times 1 \times 0.1$ mm³ target in proton (CERN IRRAD), neutron (JSI TRIGA), and mixed (high energy particles at LHC-TAN) environments, after an integrated fluence of 10^{17} p₊/cm², 10^{17} n₀/cm², and 10^{17} p_{HEH}/cm², respectively. (Simulations performed by Robert Froeschl (CERN-HSE/RP), Klemen Ambrožič (JSI), and Andrea Tsinganis (CERN-EN/STI)).

While all the values have been normalized to a similar amount of particles (10^{17}) only a qualitative comparison is possible between the different environments. On the other hand, the simulations shows relative differences between materials: aluminum experiences the largest DPA in a neutron and mixed-field environment, copper has the largest DPA in a proton environment, while chromium is in the middle for all the radiation types. Another expected result is the relatively similar order of magnitude of DPA for all the cases, but with lower values for protons, and higher for mixed-field composed mainly by neutrons.

Nevertheless, upon these results none of the selected metals can be considered to behave significantly differently from the others in the different radiation environments. Therefore it was concluded to proceed with production using all three metals, and then to verify the simulation results during the Experimental Runs with irradiation experiments in different radiation environments.

The discussion of the realization of such new metal-based dosimeter continues in Chapter 4, while the following Chapter 3 details the experimental equipment (including the irradiation facilities) and methods that were used for this research.

EXPERIMENTAL EQUIPMENT AND METHODS

This chapter encloses a collection of tools and methods that were required to perform this research.

First the irradiation facilities available at CERN are listed followed by a list of shortcomings and FCC-driven required upgrades. Secondly the specific test facilities where the irradiation experiments were performed are described.

Then the tools used for the electrical and morphological characterizations are detailed. Finally a list of the different solutions that were designed and developed to meet the stringent requirements and challenges of testing at extreme radiation levels, such as radiation hard printed circuit boards and sample holders, are shown and discussed.

*This chapter is based on the publications "**Irradiation Facilities at CERN**", published on IEEE RADECS 2017 conference proceedings, doi: 10.1109/RADECS.2017.8696163, by B. Gkotse, G. Gorine et al. [39], and on the AIDA-2020 report "**Radiation-hard instrumentation for the CERN Proton Facility**" available at URL: cds.cern.ch/record/2663195 by J. Bronuzzi, B. Gkotse, M. Glaser, G. Gorine, I. Mateu, and G. Pezzullo [40].*

Contents

3.1 Irradiation Facilities	24
3.1.1 Irradiation Facilities at CERN	24
3.1.2 Deployed Irradiation Facilities	28
3.2 Characterization Methods	34
3.2.1 Tools for Electrical Characterization	34
3.2.2 Scanning Electron Microscope for Morphological Characterization	37
3.3 Radiation Hard Tools for Ultra-High Radiation Tests	38
3.3.1 Printed Circuit Boards	38
3.3.2 Materials for Sample Holders	41

3.1 Irradiation Facilities

When designing a system that will be subject to radiation, special care must be taken in preventively validate that it will withstand and correctly operate in such radioactive environment.

For this reason, electronic equipment and components require a comprehensive qualification against various radiation-induced effects [41] to be carried out in dedicated testing infrastructures called irradiation facilities.

Several irradiation facilities were built worldwide with the purpose of offering testing conditions that can trigger the different radiation effects, as well as provide a controlled environment with known radiation spectra.

With respect to the High Energy Physics (HEP) domain, irradiation facilities are mainly used for the following tasks:

- *Radiation damage studies*: from basic research on radiation effects on materials, to specific evaluations of degradation of materials intended to be used in radioactive environments.
- *Test and development of prototypes*: irradiation tests of final assemblies and/or electronic equipment and components before installation in their final positions to study their performance degradation after long exposure/ageing due to TID, NIEL, or their functional degradation due to Single Event Upset (SEU), latch-up, etc.;
- *Test and calibration of devices*: irradiation of dosimeters and of radiation monitoring and measurement devices, for calibration purposes, as well as to provide benchmark data for Monte Carlo particle transport codes.

In the framework of this thesis, irradiation facilities are the core testing locations where to study the effects of radiation on metal micro-structures and to evaluate the RDR performance as potential FCC-dosimeter.

3.1.1 Irradiation Facilities at CERN

Several irradiation facilities are today available at CERN for applications in dosimetry, metrology, intercomparison of radiation protection devices, benchmark of Monte Carlo codes and radiation damage studies to electronics. In the last decades, most of these facilities have been upgraded to fulfill the always evolving requirements such as the need to emulate the LHC and HL-LHC radiation environment.

The main irradiation facilities available at CERN, are:

- *IRRAD*: the Proton IRRADiation Facility uses the 23 GeV proton beam coming from the Proton Synchrotron (PS) to study the effects of ionizing and non-ionizing radiation on

the performance of detectors, calorimeters, electronics as well as study the impact of radiation on materials. With an average of 5×10^{12} p/cm²/spill, a fluence of 5×10^{15} p/cm² can be achieved on a 5x5 mm² area over one week of irradiation. Since this facility was extensively used for testing the devices discussed in this thesis, more details are provided in Section 3.1.2.1.

- *GIF++*: at the Gamma Irradiation Facility (GIF++) tests can be performed with a high energy charged muon beam (with 10^4 muons/spill) from the Super Proton Synchrotron (SPS) accelerator in parallel with a 14 TBq Cesium137 source (with 1 Gy/h at 1 meter). This facility was built specifically to allow testing muon chamber detectors for the HL-LHC upgrade and evaluate their aging and performance in muon detection when exposed to strong gamma radiation.
- *CHARM*: at the Cern High energy AcceleRator Mixed field facility (CHARM), the same 23 GeV beam crossing IRRAD is driven on a copper or aluminum target to generate a mixed-field environment similar to the one encountered in the LHC tunnel. In CHARM electronics racks and other electronic equipment are tested at different field intensities to evaluate their sensitivity to radiation (SEE events) and failure cross sections.
- *HiRadMat*: the High-Radiation to Materials facility is designed to test the effects of high-intensity LHC-type pulsed beams on material samples or accelerator component assemblies. Irradiations can be carried using protons or ions from the SPS and the beam can be collimated to very small spots (<1 mm²) achieving ultra high energy densities.
- *CERF*: the CERN-EU high-energy Reference Field provides a mixed radiation field by using the SPS beam against a copper target. The resulting field resembles the environment encountered in the vicinity of high-energy particle accelerators as well as at commercial flight altitudes. At CERN this facility is widely used for testing of radiation protection instrumentation and bench-marking of Monte Carlo codes.
- *CALLAB*: the CALibration LABoratory is a state-of-the-art facility that houses several irradiation sources such as Am-Be, Cs-137, Co-60, Sr-90 and Kr-85, offering a wide range of dose rates and energies as required to fulfill most of the CERN calibration needs.
- *CC60*: this facility uses a 10 TBq Cobalt60 source for the qualification of components against TID effects. The dose rate ranges from few Gy/h to 300 Gy/h by changing the distance of the device under test from the irradiator.
- *VESPER*: the Very energetic Electron facility for Space Planetary Exploration missions in harsh Radiative environments uses pulsed electron beam from the CTF3 (CLIC Test Facility) linear accelerator for testing SEE, TID and DD on electronic components. Setting the beam at different energies (60 - 200 MeV) and fluxes (6×10^7 - 4.5×10^{12} e/cm²/s) allows to achieve dose rates in silicon in the range from few mGy/s to kGy/s.
- *X-Ray Facilities*: given the relatively low cost of X-ray tubes, at CERN there are many setups providing this kind of irradiation test.

The main parameters of these facilities are resumed in Table 3.1 and additional details can be found in [42, 43].

Facility	Particle Type	Energy	Intensity/ Activity	Beam Spot	Beam Details
IRRAD	p^+	23 GeV	10^{13} p/cm ² /h TID: 10 kGy/h	12x12 mm ² (FWHM)	2-6 spills/min
CHARM	mixed	n (thermal) HEH > 100 MeV	10^7 - 10^{11} HEH/cm ² /h TID: 0.01-100 Gy/h	Field from target	2-6 spills/min
GIF++	γ, μ	662 keV + 100 GeV muon	14 TBq (1 Gy/h at 1m)	Conical + 100x100 mm ²	Continuous + spill/SPS cycle
CC60	γ	1.17 MeV, 1.33 MeV	10 TBq (3 Gy/h at 1m)	Conical	Continuous
CERF	mixed	n^0 (<10-100-MeV) + HEH	10^8 particles/spill	Field from target	spill/SPS cycle
HiRadMat	p^+ or Pb	440 GeV p^+ /spill 173 GeV/n Pb/spill	3×10^{13} (p^+) 4×10^9 (Pb)	1x1 mm ²	spill/SPS cycle
VESPER	e^-	200 MeV	1×10^8 e^- /spill	20x12 mm ²	0.8-5 Hz
CALLAB	γ, β, n , xray	Several	From 100 MBq to 3 TBq	Several	Continuous

Table 3.1 – List of irradiation facilities available at CERN with their main parameters.

3.1.1.1 CERN Irradiation Facilities Upgrades Required for FCC

One of the greatest challenges of the FCC, as detailed in Section 2.2, will be the extreme radiation environment, several orders of magnitude higher than in the current LHC. With respect to the testing infrastructure, today's CERN facilities, which were optimized for the LHC and HL-LHC specific requirements, will need to be upgraded or renewed to support the new FCC-driven requirements.

The main requirements for an FCC-compliant irradiation facility can be resumed in the following two points:

1. the facility has to allow to test an object (material, device, system, etc.) up to the required FCC radiation levels, in a reasonable time.
2. the facility has to provide enough testing area to accommodate a large number of objects to be irradiated in parallel.

For the first requirement, mostly driven by the detectors development teams where the highest levels of radiations are expected, an FCC-compliant facility ideally has to provide an FCC-level irradiation within few weeks of experiment. This is in fact the time frame that is accounted for nowadays by the developers of new technologies for the HL-LHC. To be noted that issues known as *dose rate effects* may occur at these new facilities and ad-hoc calibrations will be required to relate accelerated testing with today's slower tests.

3.1. Irradiation Facilities

For the second requirement, mostly driven by the machine community where COTS and other equipment for the accelerator are used, an FCC-compliant facility has to provide a similar accelerator-like background radiation as well as allow for parallel testing to collect statistics on SEE and calculate failure cross sections. In fact, the greater amount of equipment that will be installed in the FCC, as well as the harsher radiation environment, will require much stricter qualification protocols to ensure the same, or ideally lower, failure rate than in today's LHC.

When searching for facilities compatible with the test requirements set by the research in this thesis, many shortcomings were identified in the current irradiation facilities available at CERN. Figure 3.1 enlists the considered CERN facilities describing their main purpose, as well as their shortcomings and possible solutions, when comparing their testing capabilities to the FCC-driven requirements.

Name	Main Purpose	FCC-driven targets (10 years operation)	Possible solution
IRRAD	Study of IEL and NIEL effects on performance of detectors , calorimeters and FE electronics for HEP experiments.	TID : 90 MGy, Φ : 2.8×10^{17} p/cm ² . → one test takes ~1 year. Issue : low flux.	Increase flux to reach target fluence faster.
CHARM	Test of COTS electronics in an LHC-like environment for SEE evaluation such as failure cross sections and system sensitivity to radiation.	TID : 100 Gy, Φ : 7.9×10^{10} p/cm ² . → low levels, but 4x more systems for a 100 km FCC. Limit on parallel tests ~1 year. Issue : not enough space.	Larger irradiation bunker to test more racks in parallel.
GIF ⁺⁺	Evaluation of detection performance and aging of muon chamber detectors in ionizing dose environment.	TID : 10 kGy. → one test takes >1 years. Issue : both space and dose-rate.	Larger irradiation bunker to test bigger equipment + stronger gamma source.
CC60	Validation and test of electronic components and systems to ionizing radiation .	TID : 10 MGy. → one test takes >1 year. Issue : both space and dose-rate.	Stronger source.
VESPER	Characterizing electronic components to SEE , TID and DD , for the operation in a Jovian space-environment.	TID : 10 MGy. Issue : facility not equipped for wafer level testing, and small irradiation table.	Upgrade of testing infrastructure.

Figure 3.1 – List of irradiation facilities available at CERN that will be used for the FCC, with details on their performance as compared to the FCC-driven requirements [39].

In conclusion, these two clear shortcomings of the current CERN irradiation facilities were identified:

- **Need of faster irradiations**: today's fluxes and dose rates are too low. The proposed solution is an increase of the number of spills dedicated for irradiations, and an update of the current Co60 and Cs137 sources with stronger ones. This will allow to reach FCC-levels faster.
- **Need of larger irradiation areas**: on average the amount of equipment that will be installed in the 100 km long FCC will increase exponentially, thus requiring bigger irradiation bunkers in order to allow the irradiation of more systems in parallel.

These limitations of the CERN irradiation facilities, as will be explained in the next Section 3.1.2, prompted the search of external facilities that could match the testing requirements for the developments discussed in this thesis. In parallel, this raised the need of having a repository

which the members of the high energy physics community could use to search for other irradiation facilities suitable for their irradiation requirements. For this reason, a database of irradiation facilities was developed to be used also by the future FCC community.

While lists of available irradiation facilities existed, they were often outdated and not maintained. Thanks to this database these old websites were decommissioned in favor of the newly developed one. This database contains today an essential but exhaustive collection of information from more than 200 irradiation facilities available at CERN, in the EU and worldwide. The result of this work can be seen online at [44] and is detailed in Appendix A.

3.1.2 Deployed Irradiation Facilities

While the testing infrastructure at CERN allows a wide choice of radiation fields and intensities, often external facilities are required to fulfill specific requirements. In fact, already in the framework of this thesis, several months of irradiation were required to reach an FCC-equivalent level in a CERN radiation facility. For this reason, along with CERN facilities (with the IRRAD Proton Facility and the Neutron Absorber (TAN) element in LHC-Point 1), also accelerated irradiation tests (that lasted one week each), were performed in a Nuclear Reactor at Jožef Stefan Institute (JSI) in Ljubljana (Slovenia).

The detailed descriptions of these facilities are given in the sections below, while the performed experiments will be described in Chapter 4.

3.1.2.1 CERN IRRAD Proton Facility

All the produced prototypes presented in this thesis that were tested with protons, were irradiated at the CERN Proton Irradiation Facility (IRRAD). The IRRAD proton facility is located on the T8 beam-line at the CERN PS East Hall (building 157) where the primary proton beam with a momentum of 24 GeV/c is extracted from the Proton Synchrotron (PS) ring, as shown in Figure 3.2-A.

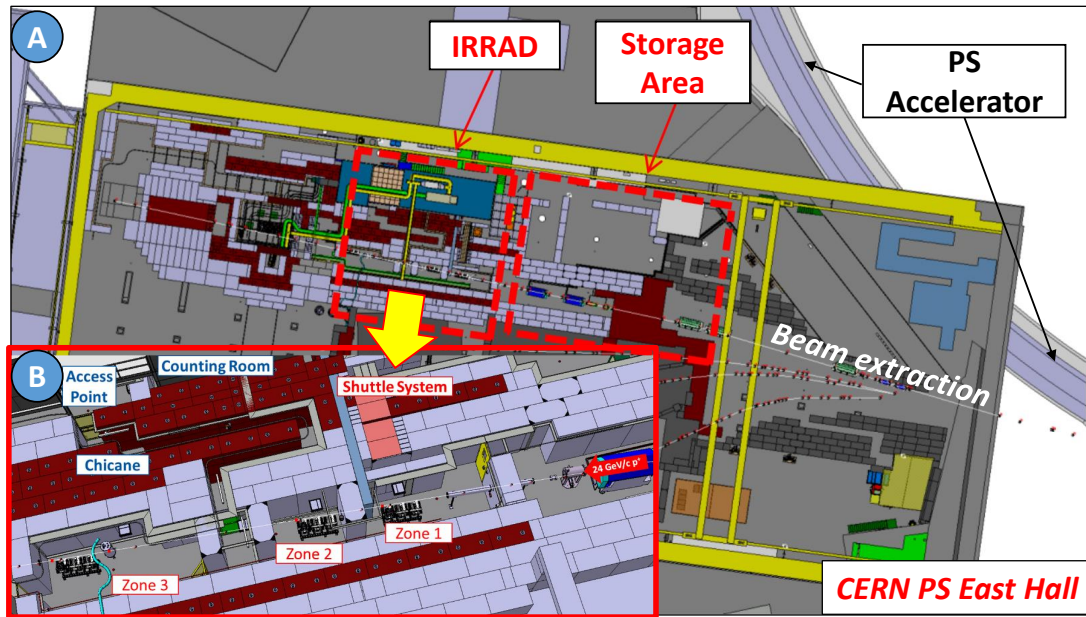


Figure 3.2 – A) Overview of the CERN Experimental East Area, with the location of the IRRAD facility irradiation areas. B) A close-up of the IRRAD bunker where the 24 GeV/c proton beam travels from right to left, crossing the three irradiation zones.

The typical proton beam size is of $12 \times 12 \text{ mm}^2$, and for special irradiations it can be defocused to obtain a non uniform shape or an overall bigger size beam-spot. The beam is sent into the IRRAD facility in spills (bunches of protons) of $\sim 400 \text{ ms}$ duration, every 10 seconds on average. During standard operation, every spill contains about $5 \times 10^{12} \text{ protons/cm}^2$, but such quantity can be varied by the CERN Control Center (CCC) to go as low as 10^{12} p/cm^2 to $8 \times 10^{12} \text{ p/cm}^2$ without requiring dedicated re-calibration of the extraction magnets.

In order to precisely position samples inside the proton beam, the irradiation bunker is equipped with remotely controlled tables (shown in Figure 3.3-A). The IRRAD tables can move with a $\pm 0.1 \text{ mm}$ precision in the transversal plane with respect to the beam-axis and they can rotate on their axis to be aligned with the beam up to an angle of $\pm 0.025^\circ$ [45]. In addition, a remotely controlled conveyer (IRRAD1 shuttle, shown in Figure 3.3-B) is available for the irradiation of smaller and passive samples with a maximum overall dimensions of $5 \times 5 \text{ cm}^2$. The main advantage of such conveyer is that it can be moved from the outside area to the irradiation position without the need of physically accessing inside the irradiation bunker, thus without stopping the beam.

For all the tables, a dedicated HW and SW user interfaces have been developed allowing the users to remotely control the systems in an easy and user-friendly manner, as well as to monitor the positions of the samples and the environmental conditions of the IRRAD facility in real-time. All these information are displayed on dedicated web pages accessible to the users [42].

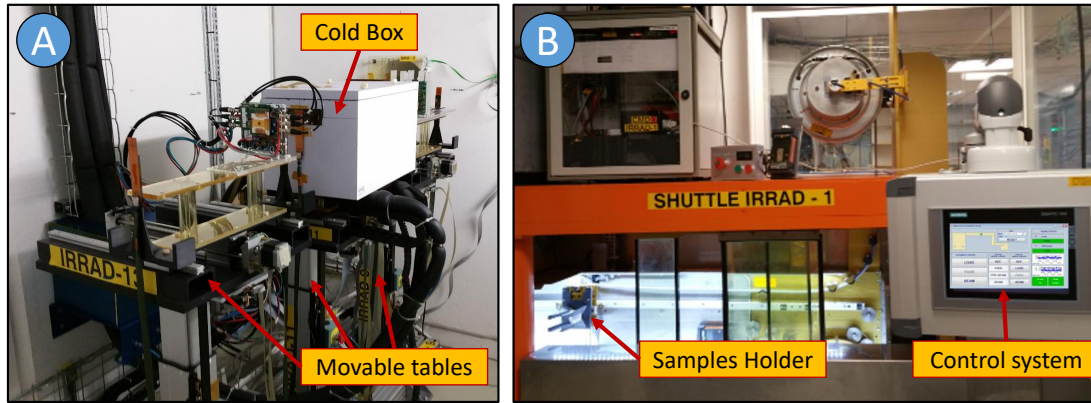


Figure 3.3 – A) Picture taken in the IRRAD Zone 2, with three movable tables and one of the cold boxes for cold irradiation experiments. B) Picture of the IRRAD1 shuttle system.

Figure 3.2-B shows the IRRAD facility irradiation area where the IRRAD tables are located, within three irradiation zones:

- **Zone 1:** first zone to be crossed by the beam thus having the cleanest irradiation conditions, in terms of beam size and spectral contamination from secondary particles. This zone is dedicated to the irradiation of low atomic number (low-Z) samples as thin silicon devices and particle detector test structures. All the irradiation experiments discussed in this thesis were performed in this zone.
- **Zone 2:** intermediate zone equipped with the largest amount of cabling connected to the control room. This zone is dedicated to irradiation tests of electronic equipment under power and with more complex active readouts.
- **Zone 3:** last zone of IRRAD used for the highest-Z samples, such as dense materials used in the construction of calorimeter detectors. Being the farthest from the access door of the irradiation bunker, it's the safest place where to irradiate samples that are expected to become very radioactive. This zone is used to test larger samples, since the beam reaches a size of about $20 \times 20 \text{ cm}^2$.

Irradiations at negative temperatures are also possible in IRRAD for both active and passive tests. Shown in Figure 3.3-A, cold boxes allowing for cold irradiation experiments down to $-25 \text{ }^\circ\text{C}$, are installed on Table 5 and 11, respectively in Zone 1 and 2. The temperature on these tables is continuously monitored and notification alarms are sent in case of temperature variations. Another setup for cold irradiations is the cryostat in Zone 3. Here, irradiations of samples kept at cryogenic temperatures (down to 1.9 K) are possible using such cryostat filled with liquid Helium (LHe) [46].

In this thesis, all the described experiments were performed installing the samples on the IRRAD7 table in Zone 1, where the beam focusing is most compatible with the size of the tested devices. During the five months long irradiations performed in 2017 and 2018, the table was dedicated to the experiments for this thesis only.

3.1.2.2 JSI TRIGA Nuclear Reactor

The nuclear reactor at the Jožef Stefan institute, shown in Figure 3.4, is a 250 kW TRIGA (Training, Research, Isotopes, General Atomics) Mark II research reactor [38].

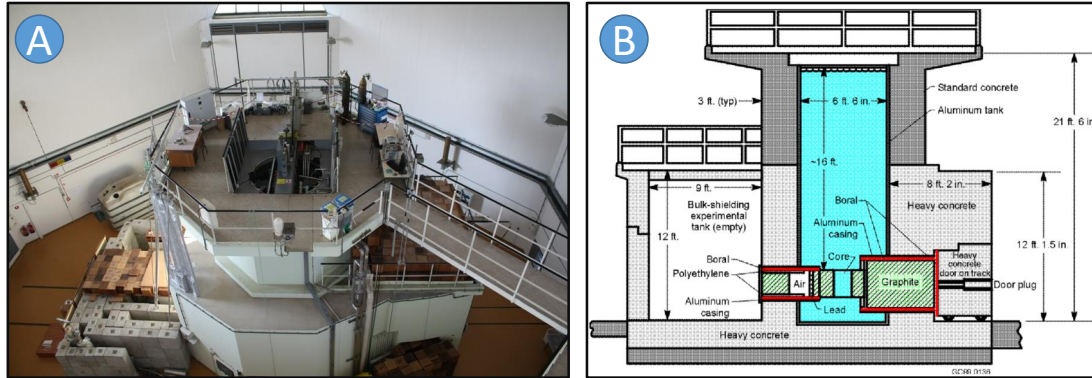


Figure 3.4 – A) Photo of the TRIGA Mark II reactor at JSI. B) Cross-section of the reactor facility.

In this facility, irradiations are performed by placing samples into the reactor core using dedicated irradiation channels. The neutron flux experienced by the samples is dependent on the position in the reactor core, and is proportional to the reactor operating power that can range from 250 W to 250 kW. The monitoring of the reactor's condition and setting of the power is done from the control room shown in Figure 3.5-A.

As shown in Figure 3.5-B three positions were available for irradiation tests during the period of interest:

1. *Central Channel (CC)*: found in position A1 of the core, is located in the exact center of the reactor, surrounded by fuel elements. The flux reached at full power in this position is the most intense reaching about $5 \times 10^{12} \text{ n/cm}^2/\text{s}$.
2. *Lateral Channel (LC)*: found in position F1 of the core, is located on the side of the reactor. In such position the flux at full power is less intense reaching levels in the order of $1.5 \times 10^{12} \text{ n/cm}^2/\text{s}$.
3. *Triangular Channel (TriC)*: the biggest irradiation channel, obtained by merging three positions (D8,E10,E11) allows irradiating big objects, with a flux about $3.5 \times 10^{12} \text{ n/cm}^2/\text{s}$ at full power.

A detailed description of these irradiation positions with the characterization in terms of neutron spectra and fluxes are reported in [47].

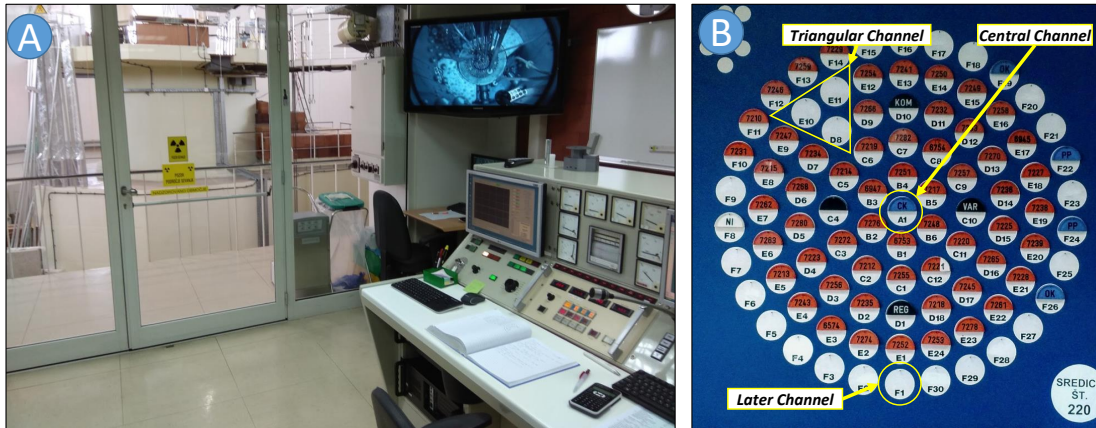


Figure 3.5 – A) Picture of the reactor control room with the monitor showing the reactor core. B) JSI TRIGA Mark II reactor core configuration of fuel elements, control rods, and irradiation channels, during the irradiation tests performed for this thesis.

The JSI reactor was chosen for the experiments described in this thesis, as it was accessible through the Transnational Access funding within the AIDA-2020 [48], and also because this TRIGA reactor is a reference center for neutron irradiation of CERN dosimeters and detectors [49].

3.1.2.3 LHC Neutron Absorber (TAN)

The LHC tunnel is composed of several different elements that are used to accelerate (RF cavities) and bend/focus (superconducting magnets) particles within the circular path. In four interaction points (IP) the two counter rotating particle beams are focused to collide generating the particle showers that are then studied in the different detectors surrounding the interaction points. In order to prevent the LHC superconducting magnets close to the interaction points to fail due to radiation and heating, special neutral beam absorbers (Target Absorber for Neutrals, TAN) are located in the LHC [50]. The function of the TAN is to absorb the particle showers leaving the interaction points, as neutrons and photons, before they could enter into the tunnel, potentially damaging the superconducting magnets.

Shown in Figure 3.6-A, a picture of such TAN element in the LHC tunnel, with its schematic view in Figure 3.6-B.

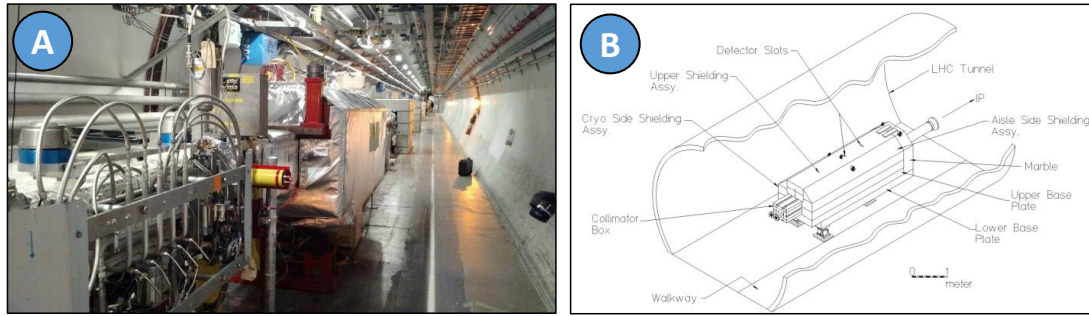


Figure 3.6 – A) Picture of the TAN element as seen looking towards the ATLAS experimental cavern. B) Schematic of the TAN [51].

Located also inside the TAN are the Beam Rate of Neutrals (BRAN) monitors, which are ionization chambers that are used to measure the luminosity of the accelerator [52]. The BRAN monitors have been developed to withstand extreme radiation levels estimated to reach several MGy per year [53].

Such location resulted being a perfect spot where to perform an irradiation test in a *real* accelerator environment, very similar to the extreme levels that will also be encountered in the FCC. For this reason, profiting of the LHC winter shutdown, when some of the BRAN elements were stored in the RP buffer zone (as shown in Figure 3.7-A), it was possible to prepare two sensors bars and to insert them in front of the ionization chambers, as shown in Figure 3.6-B. Before the restart of the LHC, the BRAN with the sensors bars was inserted inside the TAN as shown in Figure 3.6-C. The sensors were then connected to the ATLAS service cavern via spare cables left from the BRAN monitors.

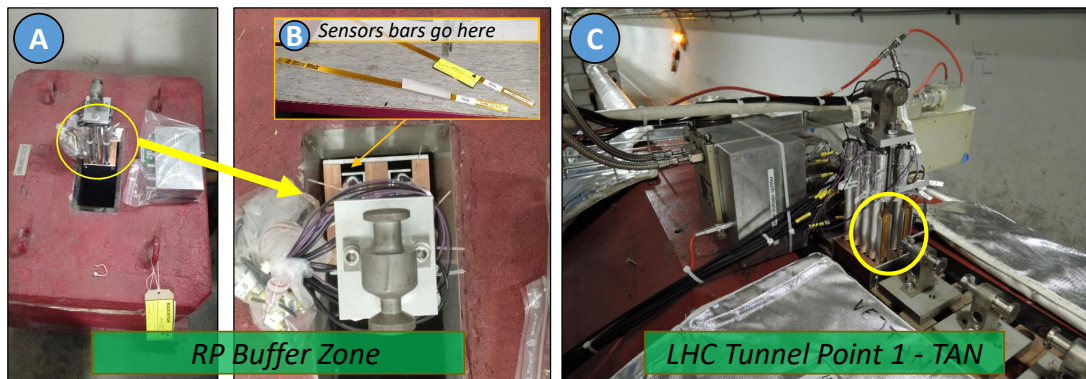


Figure 3.7 – A) Iron block in the RP buffer zone of Point 1 where the BRAN monitors are stored during the LHC winter shutdown. B) The sensor bars are installed inside the BRAN monitor, ready to be transported into the LHC tunnel. C) Picture of the BRAN monitor installed inside the TAN absorber in Point 1 [credits: S.Jakobsen]

As will be explained in Section 4.4, and as shown in Figure 3.8-A, the tested PCBs were placed on the bottom part of the sensors bar, while several passive dosimeters were placed all along

Chapter 3. Experimental Equipment and Methods

the bar. The readout of the Gafchromic (GAF) films (shown in Figure 3.8-B) allowed to have a profile of the radiation levels and to estimate the total dose integrated by the PCBs.

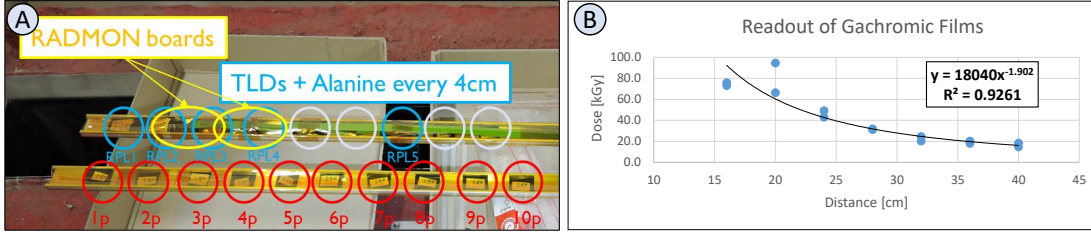


Figure 3.8 – A) Picture of the sensor bar with several passive dosimeters. B) Readout of the GAF films along the bar (first films burnt due to high radiation).

Additionally, Monte Carlo simulations were performed and compared to the experimental data. These results, together with the values extrapolated from the GAF films, are enlisted in Table 3.2.

	Distance on sensor bar	Simulated Dose for 50 fb^{-1}	GAF films extrapolation
PCB1	2 cm	6 MGy	4.8 MGy
PCB2	6 cm	1 MGy	0.6 MGy

Table 3.2 – Radiation levels cumulated over 50 fb^{-1} of ATLAS luminosity as simulated and extrapolated for PCB1 and PCB2.

3.2 Characterization Methods

In this section the different characterization methods and tools that were used in this thesis are described.

3.2.1 Tools for Electrical Characterization

Probe Station for on-chip measurements

Figure 3.9 shows the setup installed in the preparation area of the IRRAD Control Room to perform optical inspections with the microscope, and electrical measurements directly on devices before and after irradiation.

The Suss PM8 probe station is inside a dark-box, shielded from EM interference and light. Measurements are performed by a Keithley 4200A-SCS semiconductor parameter analyzer allowing for IV characterizations, with a current ranging from 10 aA to 1 A and a voltage ranging from 0.2 μV to 210 V. The 4200A-SCS allows also to perform CV measurements in the range

from 1 kHz to 10 MHz with up to ± 210 V DC bias, without the need of reconnecting the cabling thanks to the automatic CVIV Multi Switch unit. The probe station is also equipped with a thermo-chuck for measurements from 5°C to 125°C.

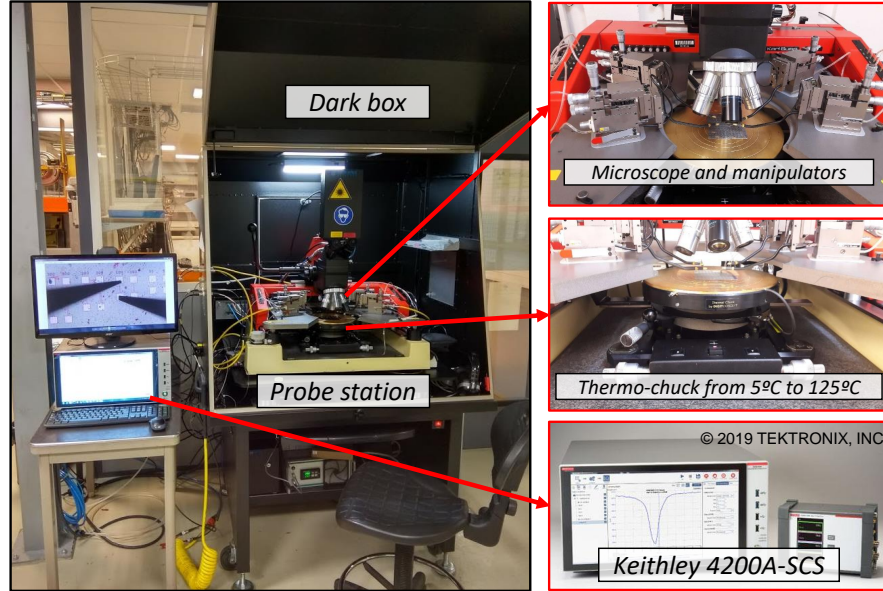


Figure 3.9 – Probe station setup in the IRRAD Control Room.

Test-bench for remote&online electrical measurements

In order to measure the radiation sensors tested in this thesis, a setup capable to source a constant current and read the developed voltage was assembled as shown in Figure 3.10.

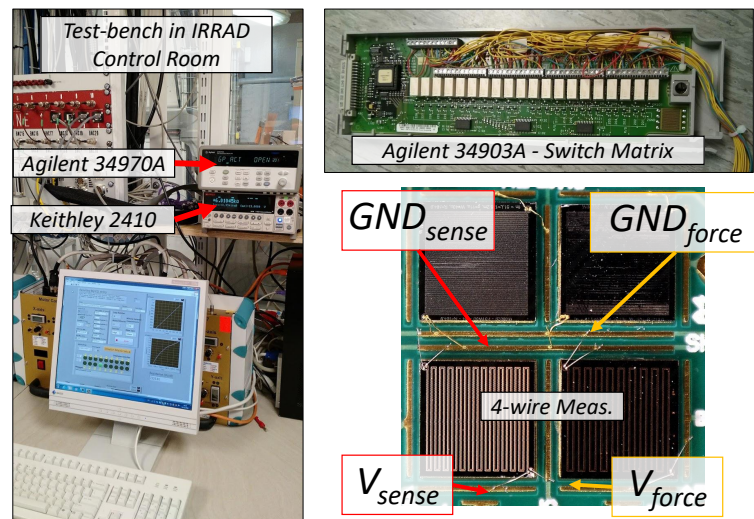


Figure 3.10 – Readout test-bench installed in the IRRAD Control Room.

The different connections between the blocks are shown in Figure 3.11, and are:

- *Keithley 2410*: this Source Meter Unit (SMU) can supply (or measure) a wide range of currents from 1 pA to 1 A, and a wide range of voltages from 100 nV to 1100 V. It allows accurate measurements over 2 or 4 wires. It can be fully controlled via the GPIB.
- *Agilent 36970A*: GPIB addressable switch unit that can be equipped with up to three switch module cards (34903A).
- *Agilent 34903A*: this add-on board for the switch unit (36970A) can be custom-rewired to allow redirecting the I&V from the SMU into one selected device at a time. Thanks to the 20 relays, a single switch board can address up to 4 FCC-RADMON.
- *PC with Labview*: a custom graphical user interface (GUI) was written to automatically set the SMU, select the device under test, perform the readout, and save the data into the database.

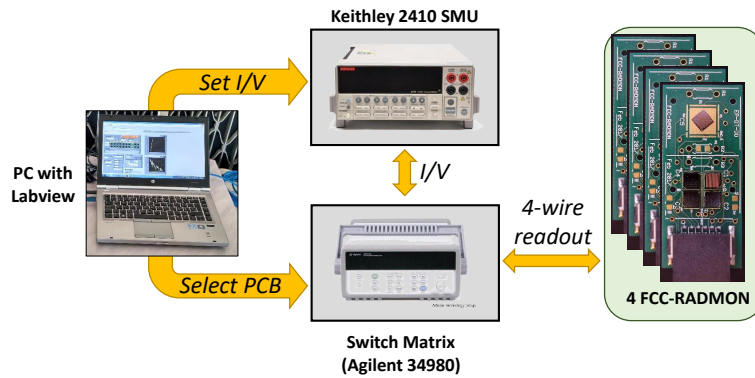


Figure 3.11 – Schematic view of the connections between blocks of the FCC-RADMON readout test-bench.

Labview software and database logging

The LabVIEW control panel, shown in Figure 3.12, allows to set up all the acquisition parameters (number of channels, time delays, bias current levels, repetition time, etc.) and save the acquired data on a file locally and in an online MySQL database.

Both raw and processed data are saved in the database, including: timestamp, label, set sweep min current, set sweep max current, readout voltages, calculated resistance, calculated temperature (from NTC sensor), etc.

Using the GPIB connection, at a chosen period (from every minute to every hour), the Labview software controls the Agilent 34970A equipped with a 34901A switch matrix, to select one sensor at a time, and driving the Keithley 2410 SMU, it issues a 50-points current sweep from 0 μA to 100 μA . Then the developed voltage together with the resistance value calculated as the slope of the performed I-V curve, are all saved in the database.

Even if the readout was performed on sensors over long cables (30 m in IRRAD, >500 m at LHC-TAN (over thicker cables) and 10 m in JSI) any introduced DC measurement error was minimized thanks to a 4-wire readout configuration shown in Figure 3.10.

An example of readout data retrieved from the database and displayed "live" on a dedicated web page is shown in Figure 3.12.

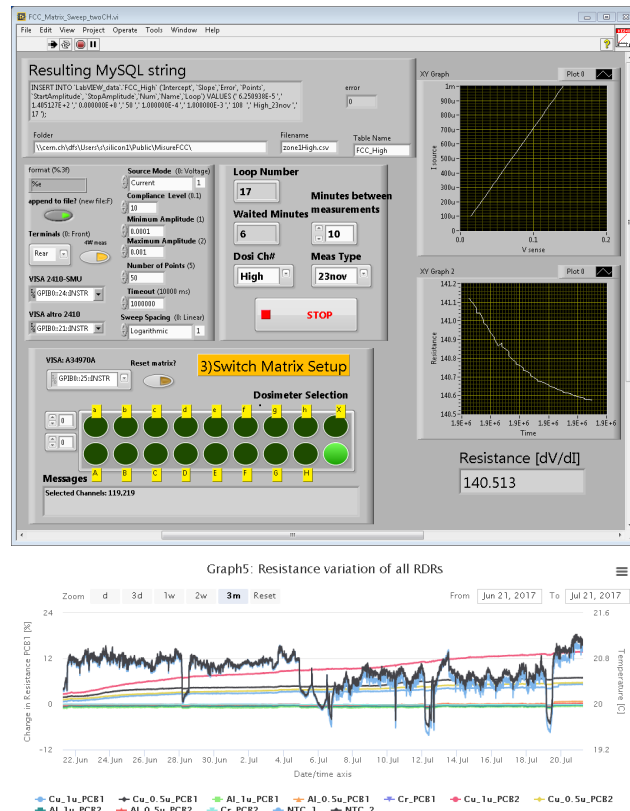


Figure 3.12 – On the top, screenshot of the LabView™ interface used to drive the automatized online measurement. On the bottom, example of readout data (dosimeters resistance increase in color and temperature in blue and black) retrieved from the database and displayed "live" on a dedicated web page.

3.2.2 Scanning Electron Microscope for Morphological Characterization

In order to assess the changes on the microstructures tested during this thesis research, detailed morphological characterizations were carried out by means of imaging with a Zeiss XB540 Scanning Electron Microscopy (SEM) combined with a Focused Ion Beam (FIB). The Secondary Electron Secondary Ion (SESI) detector was used for conventional imaging while the FIB was used to perform cross sectional milling and reveal cross sections of the different metal coatings on the samples.

In Figure 3.13 the picture of the microscope is shown, positioned in a climate-controlled room in order to maintain a constant temperature and humidity and to minimise vibrations induced by noise. A Faraday cage is also used to reduce the influence of neighbouring magnetic fields. Upon request, the room can be classified by the CERN Radiation Protection to allow analyzing

and storing radioactive samples.



Figure 3.13 – Picture of the Zeiss XB540 microscope of the CERN Engineering department MME group. (Image: CERN)

The standard morphological characterization performed on the samples for this thesis started with a FIB cross sectional milling, across the whole width of the devices. Milling is performed first by the deposition of a platinum (Pt) barrier on the surface of the sample at a milling current of 300 pA in order to protect the sample surface and ensure a sharp cross sectional surface. Then, coarse milling at 7 nA is used to dig into the material. A final polishing of the resulting cross sectional surface is normally performed at 1.5 nA.

SEM imaging of the surface and the obtained cross sections were then performed at an imaging current of 2 nA and an imaging voltage from 5 kV to 10 kV. For this thesis, images were captured at 1500 \times , 5000 \times , 20000 \times and 50000 \times magnifications.

3.3 Radiation Hard Tools for Ultra-High Radiation Tests

Due to the increasing radiation levels encountered during irradiation testing at FCC-levels, specifically qualified materials have to be used for all the objects directly inserted in the radiation field such as the printed circuit boards (PCB) and sample-holders. In this Section the selected radiation-hard materials relevant to this thesis are shown and described.

3.3.1 Printed Circuit Boards

During one of the first irradiation tests, when a high fluence of 10^{17} p/cm² was reached, a failure in the PCB was experienced. As shown in Figure 3.14-A, the failure was due to the PCB

being burnt and corroded by the proton beam during irradiation, resulting in the breaking of the bonding wires. It was found out that the problem had occurred due to chlorine (Cl) contained in the standard PCB material (FR4 substrate, with Cl to reduce flammability), that because of the high fluence had bubbled out corroding the surface.

The solution was found in collaboration with the colleagues from the *Centre de Physique des Particules de Marseille* CPPM who were also experiencing similar problems while testing devices in IRRAD at HL-LHC radiation levels.

As shown in Figure 3.14-B, the first Dosimeter Holder PCB designed for this thesis, has been produced with a different halogen-free and low phosphorus content PCB substrate DS-7402 manufactured by Doosan [54], that has not shown degradation during irradiation.

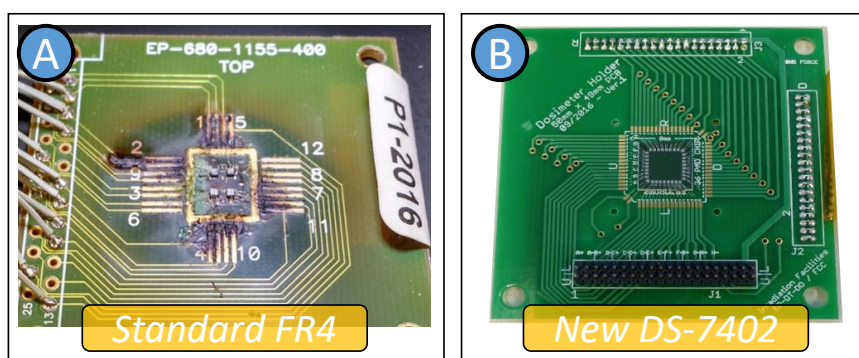


Figure 3.14 – A) Damaged standard FR4 PCB after irradiation test performed in IRRAD at FCC radiation levels. B) New rad-hard Dosimeter Holder PCB produced with a thinner halogen-free DS-7402 substrate with a wire bonded chip.

For compatibility reasons, a second design was made for the Dosimeter Holder PCB, resulting in the new FCC-RADMON shown in Figure 3.15-B. This FCC-RADMON PCB, follows the same layout of the *integrated sensors carrier* [55] currently employed for the PH-RADMON (from which the name FCC-RADMON was chosen) installed in the LHC experiments and shown in Figure 3.15-A. The FCC-RADMON mainly differs from the PH-RADMON by the substrate material, DS-7402 instead of standard FR4, and by the revised layout for wire bonding a larger number and bigger devices.

The new PCB offers space for bonding up to four 3x3 mm² and one 5x5 mm² chips, along with several positions for discrete through-hole and surface mount device (SMD) components (such as an on-board NTC temperature sensor). In the PCB configurations shown in Figure 3.15-B, five 3x3 mm² chips were mounted and wire bonded in a 4-wire measurement schema, and an SMD NTC soldered in the center. The connection to the readout system was then performed with a 12 channel insulation-displacement contact (IDC) cable using the same connector (produced by ERNI) as the current PH-RADMON system [56].

During this thesis project several FCC-RADMON PCBs were successfully irradiated up to $>1 \times 10^{18}$ neutrons/cm² in a TRIGA nuclear reactor and $>1 \times 10^{17}$ protons/cm² with a 23 GeV

Chapter 3. Experimental Equipment and Methods

proton beam, without showing any major degradation of the substrate.

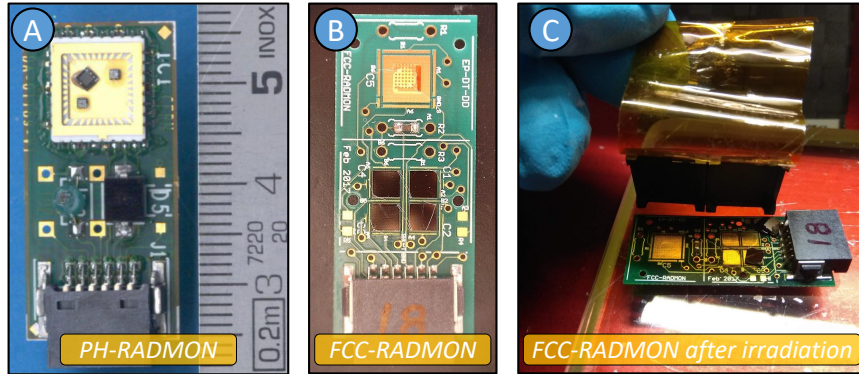


Figure 3.15 – A) PH-RADMON integrated sensor carrier for the LHC experiments. B) FCC-RADMON rad-hard PCB produced with a thinner halogen-free substrate with wire bonded chips. C) Same FCC-RADMON PCB (with chips dismounted for SEM analysis) after an irradiation test up to $>10^{17}$ p/cm² showing no major degradation.

The schematic and layout of the latest FCC-RADMON PCB are shown in Figure 3.16 and Figure 3.17.

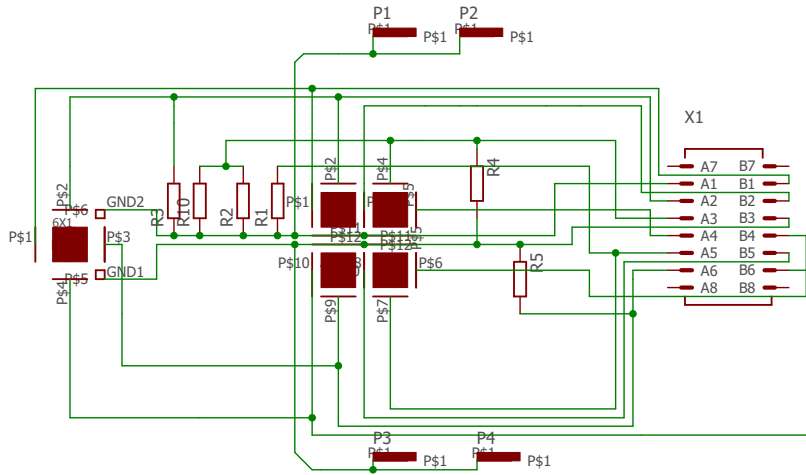


Figure 3.16 – Schematic of the FCC-RADMON PCB.

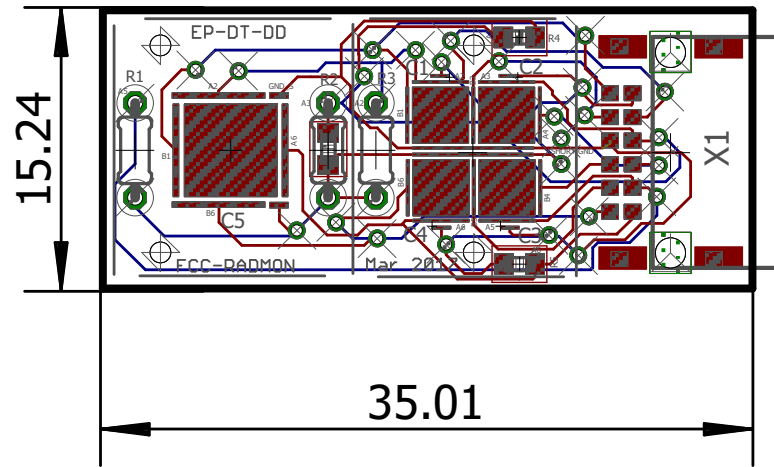


Figure 3.17 – Layout of the FCC-RADMON PCB.

3.3.2 Materials for Sample Holders

As for the PCB in the previous section, also the supports used as carriers for samples during the irradiation tests at FCC-levels, displayed degradation. In fact, as shown in Figures 3.18, the standard cardboard sample holders used in IRRAD start showing degradation when the irradiation exceeds a total proton fluence of $>10^{16}$ p/cm².

While cardboard made sample-holders offer several advantages such as low cost and versatile solution adaptable to the sample size and shape, with the increasing radiation levels required by HL-LHC and FCC experiments, the following drawbacks of the cardboard sample-holders were identified:

1. Very strong deterioration after long irradiations ($>1 \times 10^{16}$ p/cm²), with loss of mechanical strength;
2. Higher risk of contamination due to cardboard embrittlement.
3. Not reusable, generating a lot of radioactive waste.
4. Higher radioactivity (due to unavoidable impurities in the cellulose).

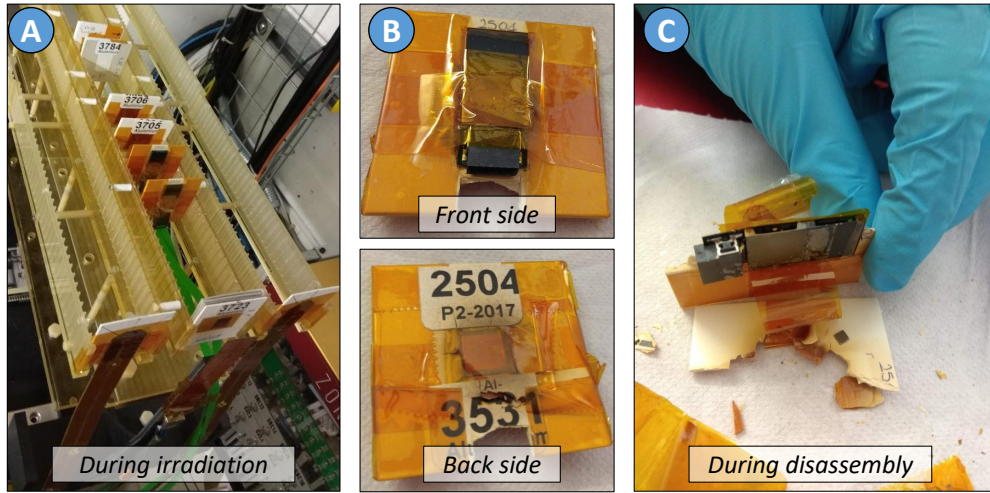


Figure 3.18 – A) Sample holders installed on an irradiation table. B) and C) Front and back side of a sample holder irradiated at FCC-levels displaying extreme embrittlement during disassembly.

These facts motivated the research for an new version of sample holders to be used as support of the devices and PCBs tested in this thesis, as well as for any future HL-LHC and FCC developments, in IRRAD and in other irradiation facilities. After an extensive irradiation test campaign in different radiation environments, as shown in Figure 3.19, carbon fiber supports were selected for irradiating samples of the RDR discussed in this thesis. More details on the sample holder material testing is reported in Appendix B.

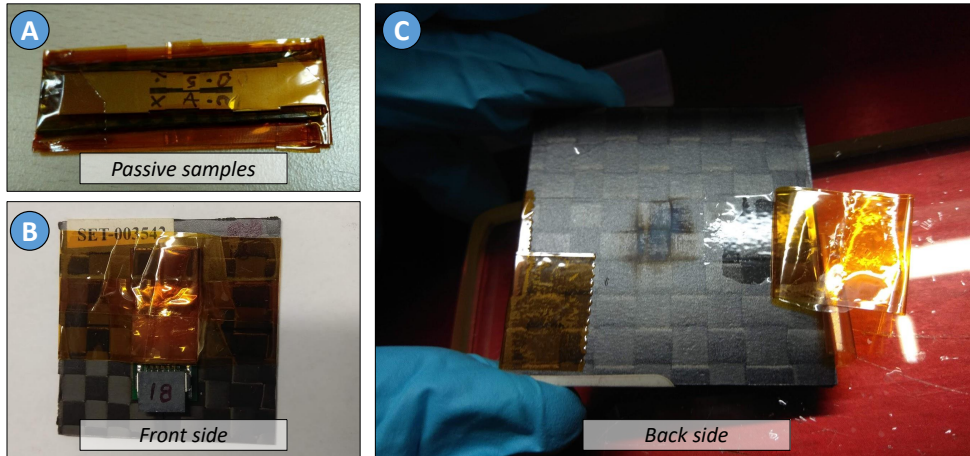


Figure 3.19 – A) Carbon fiber support used for passive (offline) irradiation of silicon chips at JSI Nuclear Reactor. B) Front side of an FCC-RADMON PCB installed on a carbon fiber sample holder irradiated in IRRAD up to FCC-levels. C) Back side showing minimal degradation in the area corresponding to the beam and no embrittlement.

EXPERIMENTAL RUNS

This chapter discusses the Experimental Runs of this thesis and their results. An overall of four major Experimental Runs were carried out, with results that helped, after each run, to refine and optimize the production and testing procedures. Finally the Experimental Runs demonstrated the applicability of a metal dosimeter for measuring very high radiation levels by means of increase of resistance. The results of this chapter are the input for the Radiation Enhanced Oxidation model (detailed in Chapter 5).

This chapter is based on the paper "Ultra High Fluence Radiation Monitoring Technology for the Future Circular Collider at CERN", published on IEEE Trans. Nucl. Sci., vol.65, 01/2018, doi: 10.1109/TNS.2018.2797540, by G. Gorine, G. Pezzullo, I. Mandic, A. Jazbec, L. Snoj, M. Capeans, M. Moll, D. Bouvet, F. Ravotti and J.M. Sallese [57].

Contents

4.1 Summary of Experimental Runs	45
4.2 First Experimental Run: Cr RDR (with Cr pads) in IRRAD	46
4.2.1 Description	46
4.2.2 Material	46
4.2.3 Layout	47
4.2.4 Readout	48
4.2.5 First Experimental Run - Results	48
4.3 Second Experimental Run: Cr RDR (with Al pads) in IRRAD	50
4.3.1 Description	50
4.3.2 Material	50
4.3.3 Layout	51
4.3.4 Readout	52
4.3.5 Second Experimental Run - Results	52
4.4 Third Experimental Run: Cr/Cu/Al RDRs in JSI/LHC/IRRAD	53
4.4.1 Description	53
4.4.2 Material	54
4.4.3 Layout	55
4.4.4 Readout	56
4.4.5 Third Experimental Run - Results	59
4.5 Final Experimental Run: Cu RDR with SiO₂ in JSI&IRRAD and SEM	67

Chapter 4. Experimental Runs

4.5.1	Description	67
4.5.2	Material	68
4.5.3	Layout	68
4.5.4	Readout	69
4.5.5	Irradiation Tests Results	72
4.5.6	Morphological Analysis	74
4.5.7	<i>Final Experimental Run - Results Summary</i>	77

4.1 Summary of Experimental Runs

The goal of the irradiation experiments performed during this thesis project, was to prove that electrically measurable radiation effects on metals could be used to quantify the integrated radiation. Multiple experiments were carried out with different RDR structures to study and to model the destructive effects produced by radiation in metals.

During the time of this thesis project, four distinct Experimental Runs were carried out. Figure 4.1 summarizes these Experimental Runs each characterized by a different material used as active layer (among the three metals chosen in Section 2.5.1) and an optimized design of the RDR layout, with optimal readout setup.

Figure 4.1 also distinguishes eight different experiments, characterized by a specific irradiation test (or SEM/FIB observation of the RDR cross-sections) which was performed to correlate the electrical readout with the effects of radiation on the thin metal films.

	DESCRIPTION	METAL	LAYOUT	READOUT	RESULTS
1 st Exp. Run	IRRAD-0 Proton irradi. <ul style="list-style-type: none">▪ First concept of RDR	<ul style="list-style-type: none">▪ Cr with Cr pads.▪ t = 100 nm.	<ul style="list-style-type: none">▪ 22x22 mm² chips.▪ 9 chips per wafer.▪ 24 devices per chip.▪ Variable W and L.	<ul style="list-style-type: none">▪ Manual readout using probe-station.	<ul style="list-style-type: none">✓ Variable length RDRs are better.✓ Cr pads not usable for online readout.
2 nd Exp. Run	IRRAD-0 Proton irradi. <ul style="list-style-type: none">▪ Bondable RDRs for remote readout.	<ul style="list-style-type: none">▪ Cr with Al pads.▪ t = 50 nm.	<ul style="list-style-type: none">▪ 8x8 mm² chips.▪ 40 chips per wafer.▪ 17 devices per chip.▪ Only variable L.	<ul style="list-style-type: none">▪ SMU+Switch matrix.▪ PCB compatible with IRRAD sample-holder.▪ 48-channel cables..	<ul style="list-style-type: none">✓ Device area and thickness are too small.
3 rd Experimental Run	JSI-1 Neutron irradi	<ul style="list-style-type: none">▪ RDRs with greater area.▪ Radiation effects on different metals. <ul style="list-style-type: none">▪ Cr with Al pads.▪ Al with Al pads.▪ Cu with Cu pads.▪ t = 500, 1000 nm.	<ul style="list-style-type: none">▪ 3x3 mm² chips.▪ 300 chips per wafer▪ 1 device per chip.▪ Larger W x L	<ul style="list-style-type: none">▪ SMU+Switch matrix.▪ Smaller PCB.▪ 12-channel cables	<ul style="list-style-type: none">✓ Need of on-board temperature sensor.✓ The layout is OK✓ The readout is OK✓ The most prominent metal is Copper.✓ Copper oxidation?
	LHC-TAN Mixed field irradi				
	IRRAD-1 Proton irradi				
4 th Experimental Run	JSI-2 Neutron irradi	<ul style="list-style-type: none">▪ Focus on Copper.▪ Impact of SiO₂ passiv. <ul style="list-style-type: none">▪ Cu with Cu pads▪ t = 500 nm.▪ Different deposition tech.▪ SiO₂ passivation.	<ul style="list-style-type: none">▪ 3x3 mm² chips.▪ 525 chips per wafer▪ 1 device per chip.▪ Larger W x L.	<ul style="list-style-type: none">▪ SMU+Switch matrix.▪ Smaller PCB.▪ 12-channel cables.▪ Temperature sensor.	<ul style="list-style-type: none">✓ Metal type, Layout & Readout are OK✓ Increase of resistance measured only for non passivated RDR.✓ Oxidation imaged only in non-passivated RDR.✓ Collected data and images used for analysis and model definition of the RDR.
	IRRAD-2 Proton irradi.				
	SEM/FIB Observation of the RDR cross section with SEM/FIB	ANALYZED SAMPLES from 4 th Experimental Run: <ul style="list-style-type: none">▪ Non-irradiated reference copper RDRs.▪ Passivated and Non Passivated RDRs from JSI2.▪ Passivated and Non Passivated RDRs from IRRAD2.			

Figure 4.1 – Summary of the four Experimental Runs and eight experiments discussed in this chapter.

4.2 First Experimental Run: *Cr RDR (with Cr pads) in IRRAD*

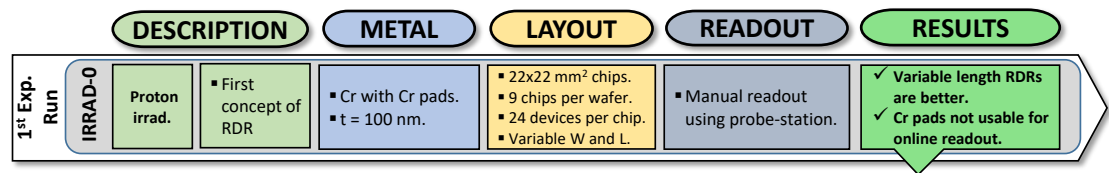


Figure 4.2 – Summary of the First Experimental Run.

4.2.1 Description

The *First Experimental Run* comprises the first proton irradiation experiment performed on a set of chromium RDRs, obtained from the first batch of micro-fabricated wafers.

As mentioned in the introduction of this thesis (Section 2.4), no previous research was ever done on radiation effects on metal films focusing on amplifying the resistance variation using as signal for a dosimeter.

This first Experimental Run allowed to go through all the test steps from design, through micro-fabrication, till irradiation test, and allowed to collect a significant number of lesson-learnt for the optimization of the successive experiments.

Overall these devices have been irradiated with protons in IRRAD for 5 weeks to a fluence of $\sim 7.6 \times 10^{16}$ p/cm² equivalent to a dose in silicon of ~ 20 MGy. No resistance measurement was performed during irradiation, and measurements were attempted on the highly-radioactive samples using a self-made shielded installation directly in the IRRAD storage area.

4.2.2 Material

As discussed in Section 2.5.1, three metals were selected as valid materials for the active layers of the RDRs, but, as shown in Figure 4.3, only chromium was used in this *First Experimental Run*. Only Cr was first chosen since it has a much better adhesion properties compared with copper and aluminum (as shown in Figure 2.10).

An initial thickness of 100 nm was chosen for the active layer, while a second lithography was performed to create the 300 nm thick chromium interconnections and contact pads. The 100 nm thickness was chosen to obtain a device electrical resistance in the range from few Ω to few k Ω .

Contact pads were necessary to allow correct probing (to avoid scratching away the active layer), and chromium was chosen for the interconnection and contact pad layer (and not the more common aluminum) to introduce as little as possible different materials in the final device stack.

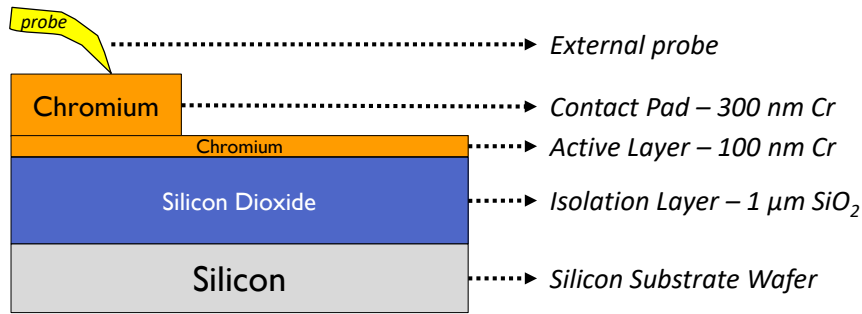


Figure 4.3 – Cross section of the fabricated device for the First Experimental Run with active metal layer made of Cr.

4.2.3 Layout

The size of the single RDR chip was chosen to have an active layer compatible with the proton irradiation beam size ($5 \times 5\ \text{mm}^2$) and an overall die size easily mountable on a cardboard sample-holder commonly used in IRRAD for chip irradiations.

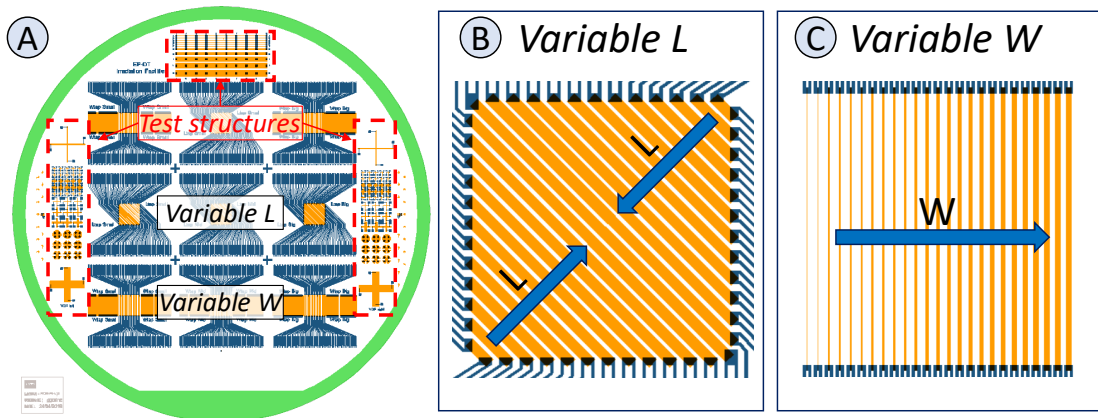


Figure 4.4 – A) Wafer layout of RDRs designed for the First Experimental Run with active metal and contact pad layers made of Cr. B) One chip with 24 Variable L devices. C) One chip with 24 Variable W devices.

Figure 4.4 shows the layout of wafers produced for the *First Experimental Run*, with the following structures:

- *Test structures*: different type of 2-pad straight resistors (Figure 4.4-A, on top in red) and Van der Pauw structures for precise 4-wire resistivity measurements (Figure 4.4-A, on both sides in red).
- *Chips*: Up to nine $22 \times 22\ \text{mm}^2$ chips per wafer, each with tapered interconnection tracks (Figure 4.4-A in blue) connecting the $0.25 \times 2\ \text{mm}^2$ contact pads with the inner $5 \times 5\ \text{mm}^2$

devices (Figure 4.4-A in orange).

- *Devices:* Up to 24 different resistive structures for each chip, some with variable length L (Figure 4.4-B, from $500\ \mu\text{m}$ to $7000\ \mu\text{m}$) and constant width W ($100\ \mu\text{m}$), and some with variable W (Figure 4.4-C, $4\ \mu\text{m}$ to $100\ \mu\text{m}$) and constant L ($5000\ \mu\text{m}$).

The different designed geometries (W,L) allowed obtaining final RDR resistances spanning from $5\ \Omega$ to $1.5\ \text{k}\Omega$.

4.2.4 Readout

The tapered-interconnections were designed to be compatible with a 48 pin probe-card, but measurements were carried out using a manual probe-station, because producing in-time a dedicated probe-card was not possible. Before irradiation, the probe-station from the CERN Solid State Detectors (SSD) lab was used (Figure 4.5-A). Chips were irradiated in passive mode (without cabling) on IRRAD7 table (Figure 4.5-B). After irradiation, due to the high radioactivity of the samples, instead of using the SSD probe-station, a custom setup was assembled in the IRRAD storage area (Figure 4.5-C), by combining micro manipulators to contact the irradiated chips, with blocks of shielding to reduce the exposure while performing the measurement.

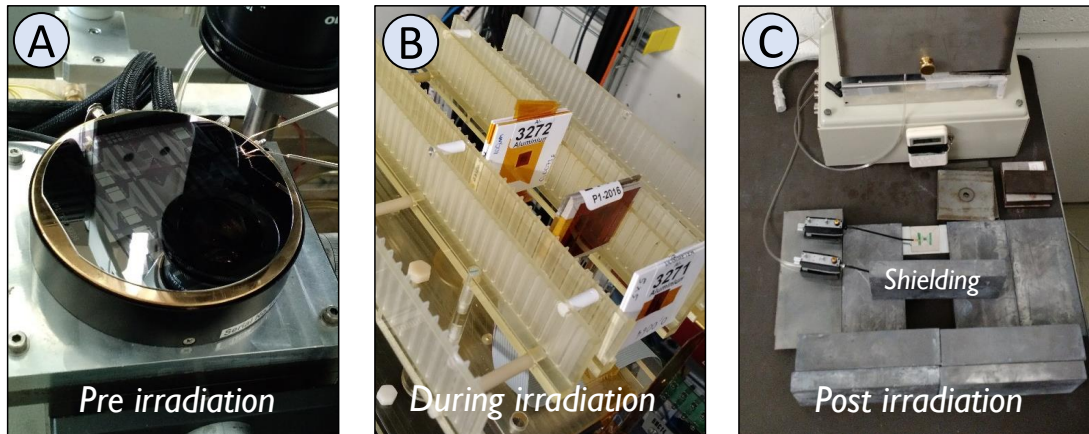


Figure 4.5 – A) One wafer being measured before irradiation using the probe-station available at CERN SDD lab. B) RDR chips installed on the irradiation table inside IRRAD. C) Post irradiation measurement setup assembled in the IRRAD storage area, in order to attempt measuring irradiated samples behind a shielding.

4.2.5 First Experimental Run - Results

This Experimental Run allowed to develop the first process flow of an RDR and to perform the first chip measurements before and after the irradiation test.

After successfully completing the whole fabrication process, and after wafer dicing, some

4.2. First Experimental Run: Cr RDR (with Cr pads) in IRRAD

selected chips were measured before irradiation using the probestation in Figure 4.5-A. These resistance measurements allowed to highlight a strong difference between chips with the *Variable L* topology from the one with *Variable W*. As plotted in Figure 4.6, where resistance measurements were used to extrapolate the resistivity value for each device, the *Variable L* topology results in a much narrower distribution on resistivity values with varying device area, whereas *Variable W* topology shows a strong unwanted area dependency. Such difference can be explained by the fact that process variations in the lithography, given the same device area, have a greater impact on the longer sides (like for *Variable W* device) then on shorter sides (like for *Variable L* devices) of the rectangular active area. For this reason, the *Variable L* topology was chosen for all the following productions and Experimental Runs.

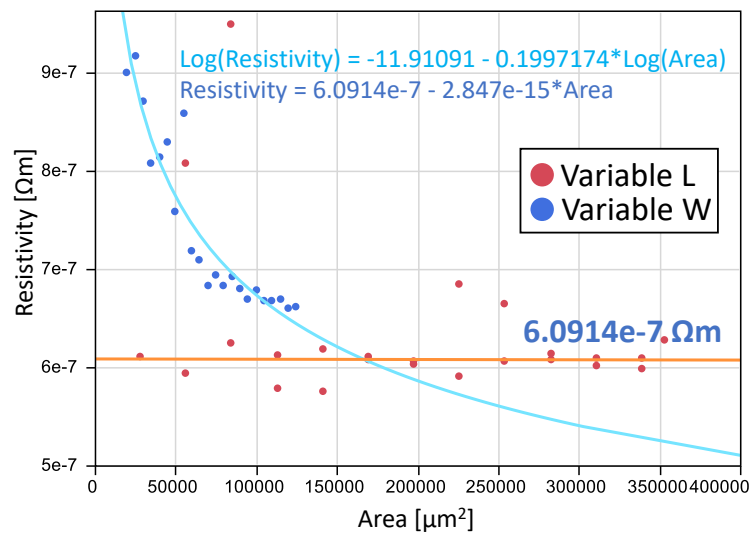


Figure 4.6 – Extrapolated resistivity values from pre-irradiation measurements performed on RDR chips with Variable Length (in red) and Variable Width (in blue).

In this *First Experimental Run* we also realized that collecting only one data point after irradiation was not enough to conclude if the resistivity of the RDRs has changed due to radiation or due to the not constant measurement conditions. Moreover, it was also not possible to perform intermediate measurements during irradiation (for example by temporarily stopping the beam once a week), since, regardless the added shielding around the manual probe-station in Figure 4.5-C, the RDRs resulted too radioactive to be handled and measured precisely. For this reason, the additional result for this *First Experimental Run* was the understanding that the electrical measurements had to be performed online during the irradiation test and remotely with proper cabling.

Through this *First Experimental Run*, the whole chain of tools was designed and developed:

- a first full-wafer layout;
- a complete fabrication process;

- a dedicated test PCB;
- the first attempts of irradiation and electrical measurements.

The variable L topology together with the revised plan for online and remote electrical measurement lead to a completely new design for the *Second Experimental Run*.

4.3 Second Experimental Run: *Cr RDR (with Al pads) in IRRAD*

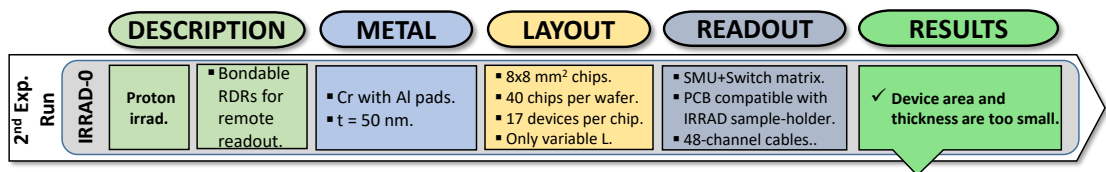


Figure 4.7 – Summary of the Second Experimental Run.

4.3.1 Description

The *Second Experimental Run* comprises the second proton irradiation experiment performed on a new set of chromium RDRs differing from the first set by having a wire-bondable contact pad in aluminum and titanium as adhesion layer. Such modification was introduced to allow online and remote resistance monitoring. These devices have been wire bonded on standard chip-carrier PCBs used at CERN for irradiation tests.

Differently from the previous experiment, the layout was modified to include only *Variable L* RDR topology and fixing the W.

An irradiation with protons in IRRAD was then performed for 3 weeks to a fluence of 1.5×10^{16} p/cm².

Resistance measurements were performed online during irradiation.

4.3.2 Material

Also for this *Second Experimental Run* only wafers with an active layer made of 50 nm chromium were used. A shift from the previous 100 nm thickness was justified by the need of increasing by a factor of two the initial resistance of all the devices to be compatible with the range of the new online readout.

Additionally, the contact pads were changed from chromium to 200 nm aluminum, to allow wire bonding. As shown in Figure 4.8 an extra 10 nm thick titanium (Ti) layer was added under the aluminum pad to enhance its adhesion and avoid a contact-failure during the wire bonding process.

4.3. Second Experimental Run: Cr RDR (with Al pads) in IRRAD

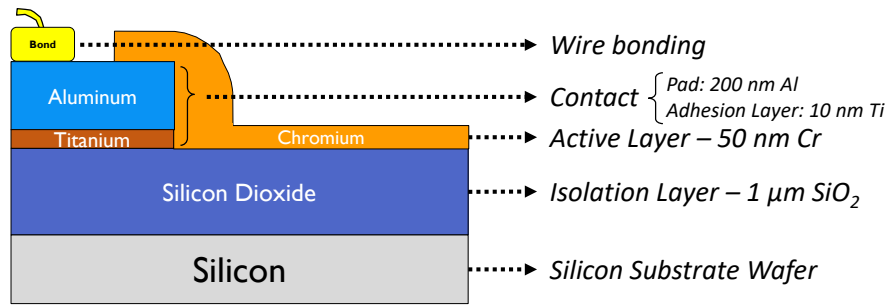


Figure 4.8 – Cross section of the fabricated device during the Second Experimental Run with active metal layer made of Cr and wire-bondable contact pad made of Al (with Ti adhesion layer).

4.3.3 Layout

The size of the single RDR chip from the *Second Experimental Run* was decreased with respect to the previous phase since the interconnection routing was not anymore required and substituted with bondable contact pads.

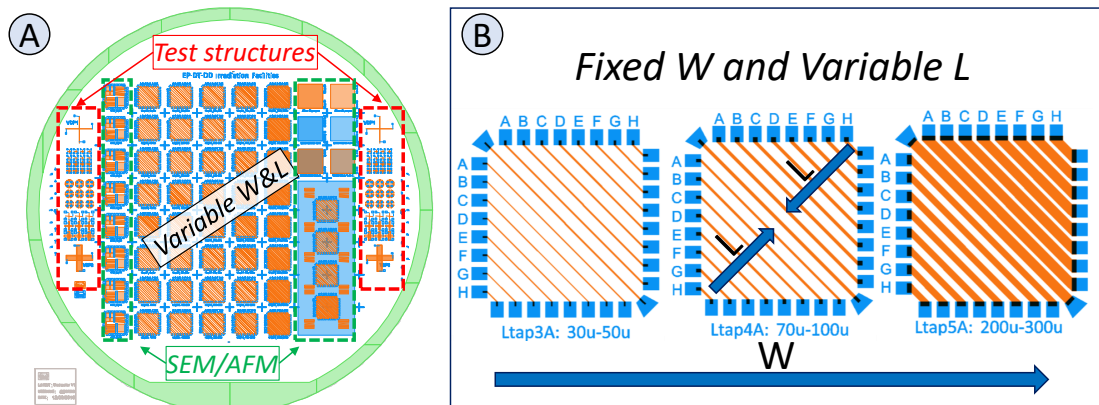


Figure 4.9 – A) Wafer layout of RDRs designed for the Second Experimental Run with active metal made of Cr and contact pads in Al and Ti adhesion layer. B) Example of chips with 17 Variable L devices with three different W.

Figure 4.9 shows the layout of wafers produced for the *Second Experimental Run*, with the following structures:

- *Test structures*: several test resistors (Figure 4.9-A, on both sides in red), as well as structures for possible future surface characterization with SEM and AFM techniques (Figure 4.9-A, on both sides in green).
- *Chips*: Up to 42 chips ($8 \times 8 \text{ mm}^2$) per wafer, with an inner device area of $5 \times 5 \text{ mm}^2$

Chapter 4. Experimental Runs

(Figure 4.4-A in orange), and on all sides, arrays of $0.4 \times 0.5 \text{ mm}^2$ Al contact pads (with Ti adhesion layer).

- *Devices*: Up to 17 different resistive structures for each chip, with *Variable L* (on the same chip) and different fixed width (for each chip), as shown in Figure 4.9-B.

The different designed geometries (W,L) allowed obtaining final RDR resistances spanning from 10Ω to $3 \text{ k}\Omega$.

4.3.4 Readout

With respect to the previous Experimental Run, the readout procedure has been shifted from manual and offline using a probe station, to automatic and online with the test-bench already described in Section 3.2.1. This change was possible by wire-bonding the RDR chip directly on a dedicated PCB as shown in Figure 4.10. Details on the realization and choice of the special radiation-hard substrate for the PCB were discussed in Section 3.3.1.



Figure 4.10 – A) One $5 \times 5 \text{ cm}^2$ FCC-Dosi-Holder PCB with wire-bonded RDR chip installed on the irradiation table inside IRRAD, and connected via the FCC-IDC-2-DB37 PCB to the readout system in the IRRAD control room. B) Screenshot of the LabView™ interface used to drive the automatized online measurement.

4.3.5 Second Experimental Run - Results

With respect to the *First Experimental Run*, this experiment has confirmed that the microfabrication of wafers with the *Variable L* topology can results in chips with a uniform resistivity among devices with different area.

It has also allowed changing the initial full-chromium design to one compatible with wire-bonding by implementing the contact pads in aluminum.

4.4. Third Experimental Run: Cr/Cu/Al RDRs in JSI/LHC/IRRAD

The combination of a radiation-hard PCB with the wire-bonded RDR, together with the automated readout system, allowed to constantly monitor the RDR resistance during the whole irradiation.

The collected data did not show any significant increase of resistance in any of the 17 monitored devices. This was explained by the too short irradiation time (only 3 weeks) which did not allowed reaching an integrated radiation fluence high enough to induce a measurable damage in the active layer of the RDR. To be able to match the RDR sensitivity to lower levels of integrated fluence such as the ones obtainable in few weeks in IRRAD, a change in the interaction volume had to be implemented. For this reason, the area (W and L) and the thickness, designed for all the next Experimental Runs, have been increased by a factor of 10, with initial resistances as high as 10 k Ω .

4.4 Third Experimental Run: Cr/Cu/Al RDRs in JSI/LHC/IRRAD

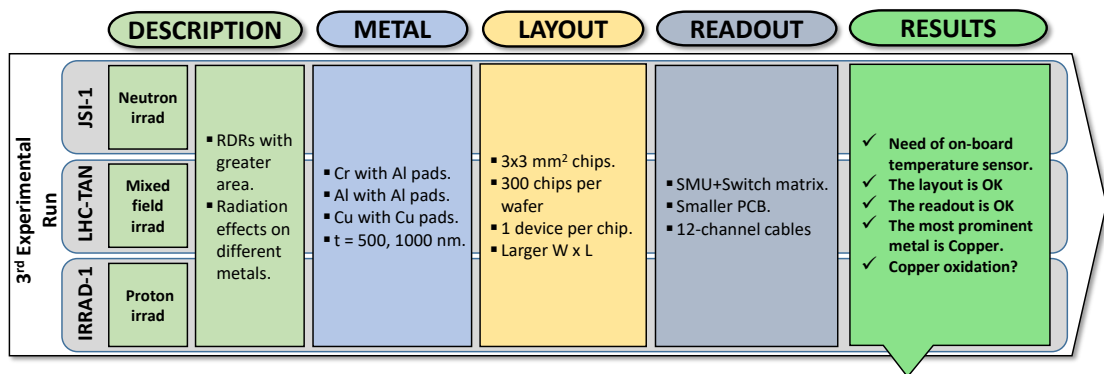


Figure 4.11 – Summary of the Third Experimental Run.

4.4.1 Description

The *Third Experimental Run* comprises three irradiation experiments:

- *JSI-1*: irradiation experiment in the JSI-TRIGA nuclear reactor, performed over 5 days of irradiation up to a total neutron fluence of 1×10^{18} n/cm². The irradiation was performed at variable temperatures reaching up to 80°C during the reactor operation and cooling down to 20°C overnight.
- *LHC-TAN*: irradiation experiment in the mixed radiation field of the Neutron Absorber in the LHC-Point 1, performed over 8 months of irradiation up to an estimated dose of 5 MGy. The irradiation was performed at a continuously varying temperature (25°C \pm 5) dependent on the number of collisions happening in the ATLAS detector.
- *IRRAD-1*: irradiation experiment in the IRRAD proton facility, performed over 5 months

Chapter 4. Experimental Runs

of irradiation up to a total proton fluence of 1.2×10^{17} p/cm². The irradiation was performed at constant temperatures around 21°C.

All experiments were done using the same layout, material, and readout, but in different radiation environments.

The new layout was obtained modifying the one of the *Second Experimental Run* to produce single devices with greater area for a greater sensitivity to radiation.

Differently from previous Experimental Runs, chromium RDR were tested alongside aluminum and copper, as decided during the material selection phase (see Section 2.5.1). While all PCBs were always hosting all three materials, due to limitations of the beam-size (*IRRAD-1*) or of the number of readout channels (*LHC-TAN*) not all the RDRs were irradiated uniformly.

Finally the readout was also changed, with a revised PCB allowing for testing fewer, but bigger single devices.

The selected devices for these experiments are enlisted in Table 4.1.

Material:	Al	Cr	Cu	Al	Cu
Thickness:	1000 nm	500 nm	500 nm	500 nm	1000 nm
PCB1-JSI1	621.9 Ω	1502 Ω	148.2 Ω	525.7 Ω	141.7 Ω
PCB2-JSI1	211.0 Ω	906.4 Ω	67.9 Ω	242.9 Ω	55.4 Ω
PCB1-LHC-TAN	92.7 Ω	2474 Ω	121.5 Ω	159.2	225.7 Ω
PCB2-LHC-TAN	36.4 Ω	1529 Ω	211.6 Ω	71.7 Ω	171.1 Ω
PCB1-IRRAD1	29.1 Ω	838.3 Ω	50.4 Ω	51.0 Ω	29.6 Ω
PCB2-IRRAD1	49.2 Ω	1502 Ω	56.2 Ω	116.9 Ω	29.7 Ω

Table 4.1 – Initial resistance values of RDRs on FCC-RADMON PCBs before irradiation at JSI, LHC-TAN, and IRRAD.

4.4.2 Material

For this *Third Experimental Run* wafers with an active layer made of chromium, aluminum and copper were used.

In order to increase the sensitivity of these devices the thickness was increased from the 50 nm of the *Second Experimental Run* to 500 nm (and 1000 nm), and to compensate for the resulting lower initial resistance, much longer L were designed as described in the following *Layout* section.

For the chromium wafers, an additional lithography step was performed to include aluminum contact pads (as shown in Figure 4.12-A). On the other hand the 500 nm thick (or 1000 nm) aluminum and copper wafers did not require an extra contact pad layer since both were directly wire-bondable.

Furthermore, as also shown in Figure 4.12, for all the three cases a titanium adhesion layer of 10 nm was included between the silicon dioxide and the active layer to guarantee adhesion (for Al and Cu) or uniform layout among all samples (for Cr).

4.4. Third Experimental Run: Cr/Cu/Al RDRs in JSI/LHC/IRRAD

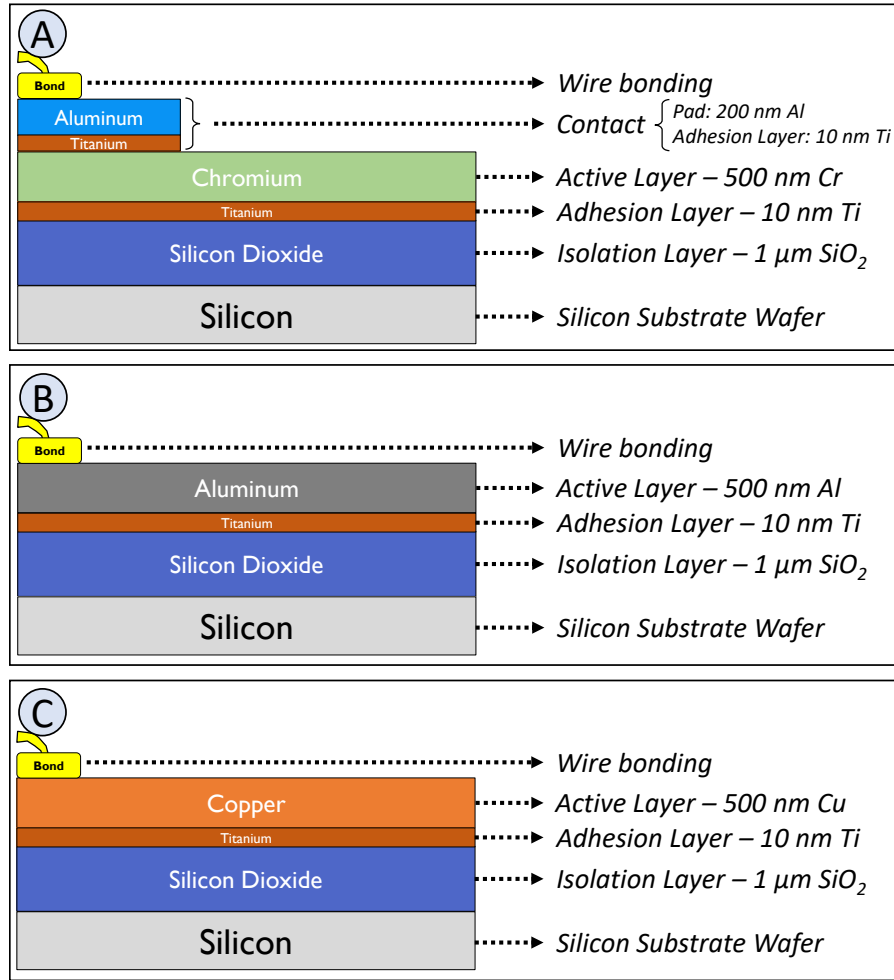


Figure 4.12 – Cross sections of the fabricated devices during the Third Experimental Run with active metal layer made of Cr (A), Al (B), and Cu (C). Wafers with an active layer thickness of 1000 nm were also produced for Cu and Al RDRs.

4.4.3 Layout

The size of the single RDR chip from the *Third Experimental Run* was decreased with respect to the previous phase from 8x8 mm² to 3x3 mm² but the single device area has been increased from 0.5 μm^2 to 7.5 μm^2 to enhance the sensitivity to radiation.

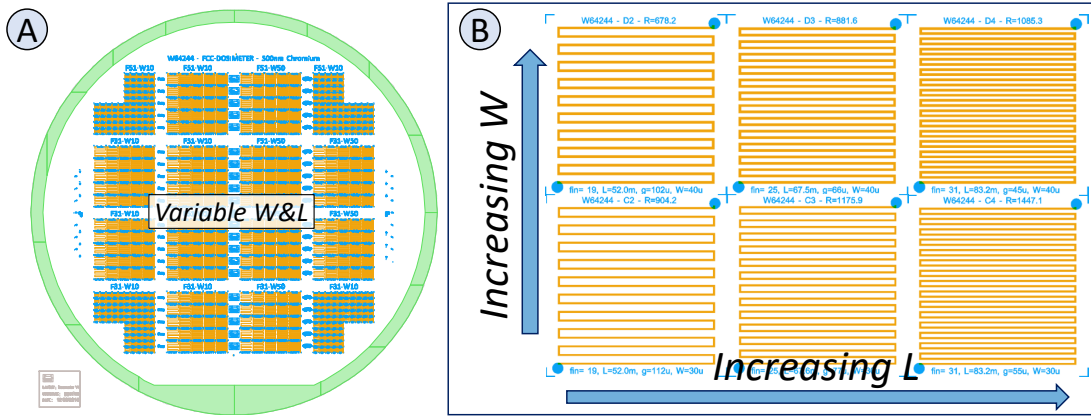


Figure 4.13 – A) Wafer layout of RDRs designed for the *Third Experimental Run* with the matrix of 16 macro groups of chips (in orange). B) Example of redesigned serpentine-shaped RDR chips, within a macro group, where the device width increases from bottom to top, and the length increases from left to right.

Figure 4.13 shows the layout of wafers produced for the *Third Experimental Run*, with the following structures:

- *Test structures*: 4 macro-groups of several test resistors (Figure 4.13-A, corner macro-groups).
- *Macro-groups*: 12 macro-groups per wafer, of which 6 macro-groups with varying width from 2 to 10 μm in steps of 2 μm , and 6 with width varying from 10 to 50 μm in steps of 10 μm .
- *Chips with Single Device*: Up to 300 different resistive structures for each wafer with varying width (2 to 50 μm) and lengths (from 6 to 150 mm) as shown in Figure 4.13-B.

The differently designed geometries (W,L) allowed obtaining final RDR resistances spanning from few Ω to hundreds Ω (for Cu and Al) and to k Ω (for Cr).

4.4.4 Readout

As for the previous Experimental Run, the readout procedure during all the irradiation experiments of the *Third Experimental Run* has been performed online with the automatic test-bench described in Section 3.2.1.

With respect to the 5x5 cm² PCB used in the *Second Experimental Run* where only one single chip was wire-bonded per board, now, a newly designed 1.5x3.5 cm² FCC-RADMON PCB (see Section 3.3.1) was used with 5 wire-bonded chips per board. This change was required to allow having on a single PCB, chips that come from different wafers (Cr, Al, Cu).

Moreover, the redesign of the PCB support was also required due to the new adapted layout of single-chip/single-device, that was implemented to increase the RDR sensitivity as explained

4.4. Third Experimental Run: Cr/Cu/Al RDRs in JSI/LHC/IRRAD

in the previous paragraph 4.4.3.

In Figure 4.14-C is shown an example of such PCB ready for irradiation at the TRIGA nuclear reactor. Additionally, in Figure 4.14-D, a similar PCB is shown, with also 5 RDR chips and an additional on-board NTC temperature sensor.

In the *Third Experimental Run* the selection of RDRs for the irradiation test was performed by screening several wafers (shown in 4.14-A) though a pre-selection by direct on-wafer measurements with a probe-station (shown in Figure 4.14-B).

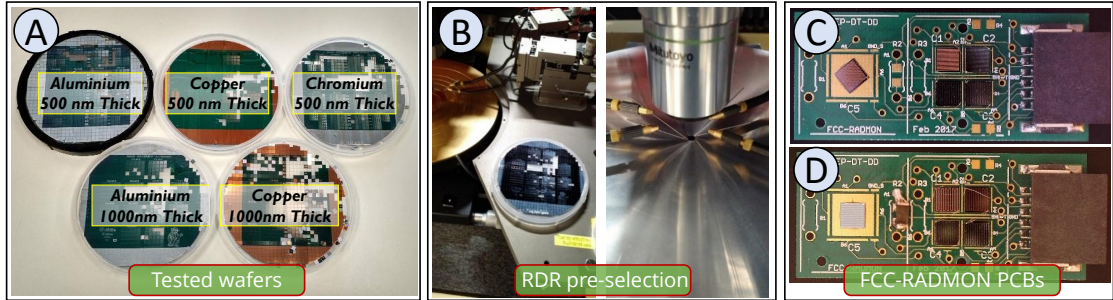


Figure 4.14 – A) Picture of five produced wafers, with some of the chips removed for the electrical characterization. B) Pre-selection and electrical characterization of RDR chips from each wafer. C) a FCC-RADMON PCB for the neutron irradiation with 5 wire-bonded RDRs, one from each wafer. D) FCC-RADMON PCB for the proton irradiation, also with 5 RDRs and an extra on-board NTC temperature sensor mounted in position R2.

For the *JSI-1* irradiation experiment at the TRIGA nuclear reactor, the FCC-RADMON PCBs have been inserted in a dedicated cylinder (shown in Figure 4.15-A) in order to prevent them from scratching along the irradiation channel while being pulled down into the reactor core (shown in Figure 4.15-B).

Using 10 m long cables, these samples were connected to the automated readout test-bench located on the top of the reactor, as shown in Figure 4.15-C.

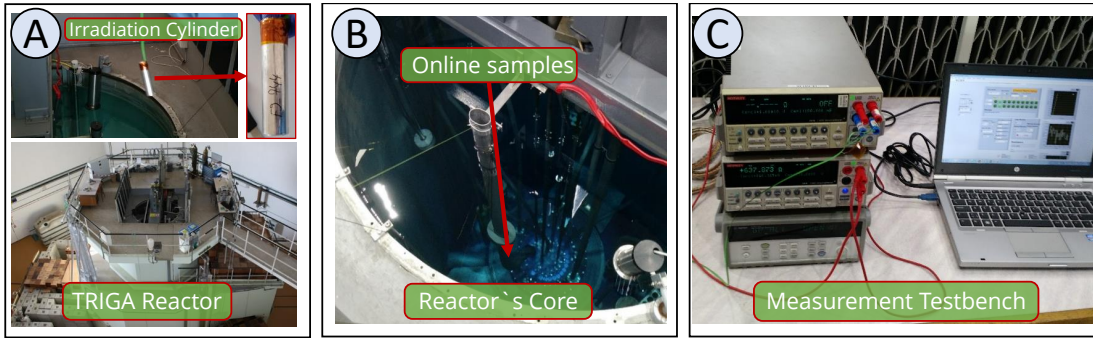


Figure 4.15 – A) Picture of the aluminum irradiation cylinder containing two FCC-RADMON PCBs stuck back-to-back. B) Picture of the nuclear reactor's core with the opening of the irradiation channel through which the cylinder with the online samples was pulled down. C) The set of tools for the automated readout test-bench as described in Section 3.2.1 running on a portable laptop.

For the *LHC-TAN* mixed-field irradiation experiment in the TAN, the FCC-RADMON PCBs have been prepared on an aluminum sensor bar having a size compatible with the luminosity monitors (Beam Rate of Neutrals, BRAN) of Point 1.

As shown in Figure 4.16-A, one PCB was mounted closer to the end of the bar (closer to the beam-pipe) while the other is inserted in the upper part. In order to perform a profile of the radiation inside the TAN, the sensor bar was populated with several passive dosimeters (films, TLDs, alanines).

Before the start of the LHC-run, the bar was inserted inside the TAN shown in Figure 4.16-B, while the connections to the automated test-bench were done through a converter breadboard connected to some free channels taken from the BRAN, as shown in Figure 4.16-C.

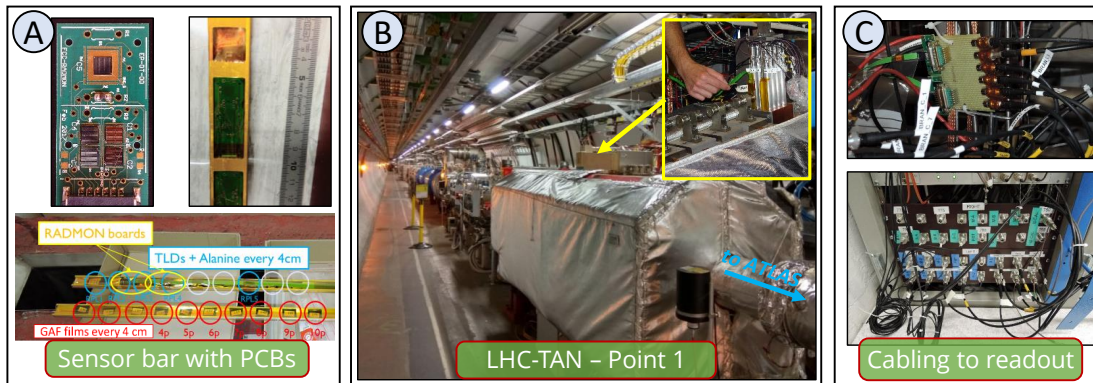


Figure 4.16 – A) The aluminum sensor bar with mounted two FCC-RADMON PCBs and several other passive dosimeters. B) Picture of the TAN in Point 1, with a closeup of the place where the sensor bar was inserted. C) The breadboard used to wire the FCC-RADMON to the BRAN patch panel connected directly to the ATLAS service cavern.

4.4. Third Experimental Run: Cr/Cu/Al RDRs in JSI/LHC/IRRAD

For the *IRRAD-1* irradiation experiment at the IRRAD proton facility, the FCC-RADMON PCBs were mounted on a standard cardboard support (shown in Figure 4.17-A) to be then easily installed on the irradiation table (shown in Figure 4.17-B). Using the patch-panels connecting the irradiation area with the IRRAD control room (with 30 m of cables), the FCC-RADMONs were constantly monitored by the automated readout test-bench shown in Figure 4.17-C.

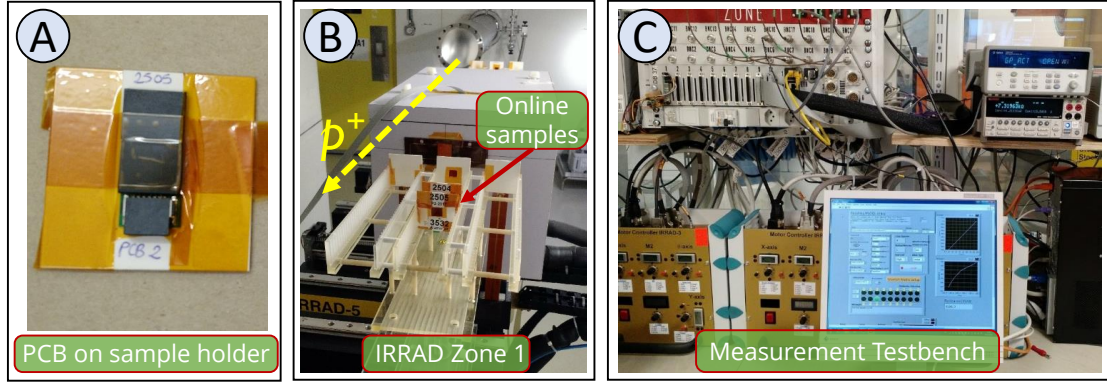


Figure 4.17 – A) Picture of the FCC-RADMON PCBs mounted on the card-board sample holder. B) Picture of the irradiation table in IRRAD zone 1 with samples. C) The set of tools for the automated readout test-bench as described in Section 3.2.1.

4.4.5 Third Experimental Run - Results

4.4.5.1 JSI-1 Experiment Results

For this experiment two FCC-RADMON PCBs were tested inside the aluminum cylinder shown in Figure 4.15-A. The cylinder was inserted into the central channel before turning ON the reactor and measurements from each dosimeter were taken every minute.

In Figure 4.18, the change in resistance (in %) of the measured RDRs is shown against the increasing total integrated neutron fluence (Φ_n). Only data points sampled when the reactor was ON are plotted in this Figure 4.18.

All devices have shown a significant change, with resistance values increased by 5% for the chromium samples, and up to 30% for the aluminum samples. However, such abrupt rise of resistance is not only induced by displacement damage, but connected with the temperature variation in the irradiation channel. This correlation with temperature can clearly be seen in Figure 4.19, where the temperature variation of the reactor fuel (dotted black line), is compared with the signal from the measured RDRs and plotted against time (over the total 120 hours). The intermittent sudden decreases (and increases) in resistance perfectly correlate to the points when the reactor was driven from full power to zero (and back).

In this experiment, the FCC-RADMON boards did not include a temperature sensor due to the limited number of available channels on the PCBs (12 total channels as described in

Section 3.3.1). In order to assess the temperature reached inside the irradiation channel during the reactor operation, a dedicated measurement was performed using a PT100 temperature probe. This test, executed during two hours of operation at full power, has shown an inner channel temperature rising from about 25 °C to >65 °C rapidly after reaching the standard "full-power" operating regime of the reactor. Also a temperature drift of about 0.5 °C/hour has been observed, meaning that at the end of a full day of irradiation (10 hours) the irradiation channel can easily reach >70°C.

The temperature variations, during the irradiation and online measurements, are clearly affecting the resistance value of all the RDRs, as visible in Figure 4.18 (negative spikes), and in Figure 4.19 (the square wave, corresponding to the overnight shutdowns of the reactor).

While the damage was not permanent for the aluminum and chromium samples, where the overnight annealing lead to almost full recovery, the copper RDRs (in particular *Cu-0.5u* and *Cu-1.0u* of PCB1) have shown a very promising result. As observable in Figure 4.19, no loss in the monitored resistance is occurring once the reactor restarts. This is further confirmed, by the overnight almost-flat plateau (longer segments between square waves), where no considerable annealing is occurring. In fact, the resistance value goes back to the value it was before the night stop, and continues then to grow with increasing fluence.

At the end of the irradiation week, the two copper RDR devices (*Cu-0.5u* and *Cu-1.0u* of PCB1) have shown an overall increase of resistance of 13.5% (*Cu-0.5u*) and 16.5% (*Cu-1.0u*) with respect to their initial values (in Table 4.1). Such increase was substantially higher during the first hours of irradiation (up to 1×10^{17} n/cm²), where the sensitivity of the two copper RDRs was of $5.6 \Omega/\Phi_n$ (*Cu-0.5u*) and $7.7 \Omega/\Phi_n$ (*Cu-1.0u*) with $\Phi_n = 10^{17}$ n/cm². However, close to the end of the irradiation (from 5×10^{17} n/cm² to 1×10^{18} n/cm²) the resolution dropped for both to $0.5 \Omega/\Phi_n$.

It is interesting to notice that the changes in resistivity of the 500 nm thick (*Cu-0.5u*) and the 1000 nm thick (*Cu-1.0u*) samples are very similar, indicating no big impact of the thickness on the final device sensitivity. On the other hand, a dependence of the sensitivity on the geometry has been observed when comparing the two mentioned copper RDRs of PCB1, with respect to the other two copper RDRs on PCB2. The firsts are longer RDRs (larger L due to more fingers, 51 instead of 31), and narrower (smaller W with 10 μm instead of 30 μm). This suggests that a greater sensitivity can be achieved with devices which initial resistance is higher, and where an interaction with an incoming particle will lead to a greater variation due to the thinner W.

This experiment has shown that copper experiences a permanent increase of resistance when irradiated in a nuclear reactor. Two possible and probably entangled causes were identified: the extreme particle fluence inducing permanent damage in the metal lattice, and/or the possible growth of the native oxide layer due to the high temperatures reached during irradiation.

4.4. Third Experimental Run: Cr/Cu/Al RDRs in JSI/LHC/IRRAD

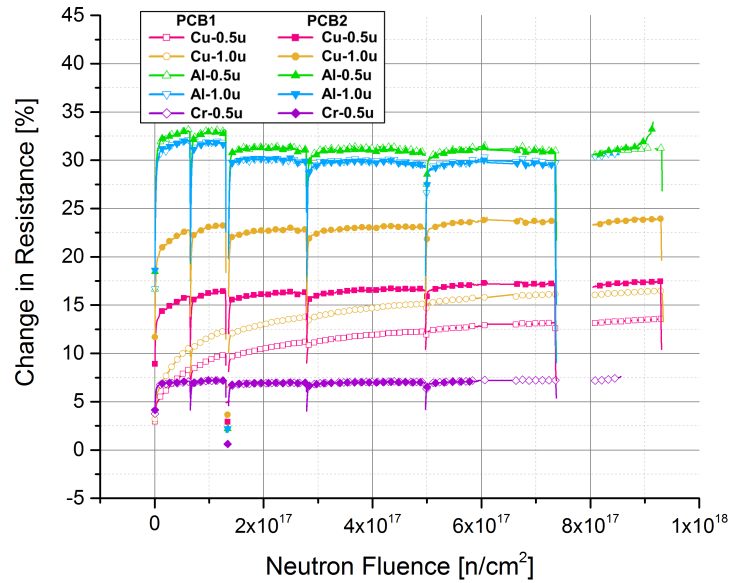


Figure 4.18 – Resistance variation from the initial value in % vs. the integrated neutron fluence, for each RDR on PCB1 and PCB2. The negative peaks correspond to the overnight ON-OFF-ON transitions of the reactor induced by abrupt changes in temperature. The void before $8 \times 10^{17} \text{ n/cm}^2$ is due to data loss during acquisition while the interrupted curves towards the end of the irradiation are due to a failure of the cable at $9.4 \times 10^{17} \text{ n/cm}^2$.

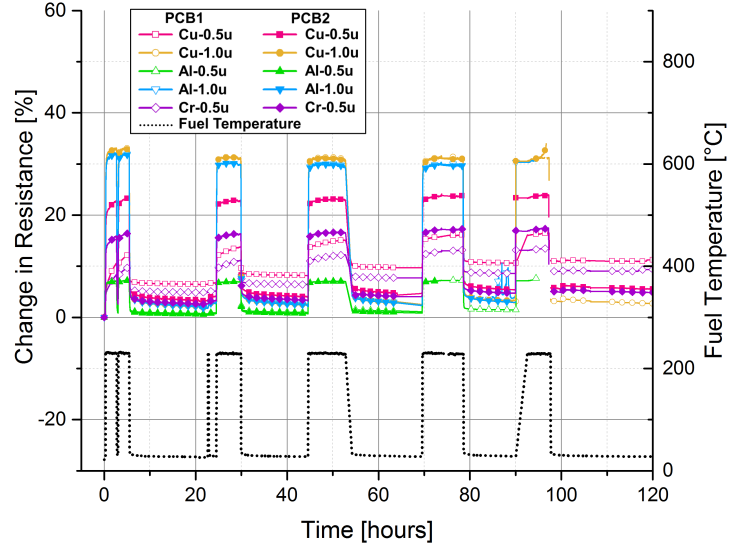


Figure 4.19 – Resistance variation from the initial value in % (left y-axis) compared with the temperature variations of the fuel elements of the reactor (black) over all the 5 days (120 h) of irradiation test (right y-axis). The points where the black curve is low at 25°C correspond to the overnight stops where the reactor was switched off, while all the RDRs either experienced annealing (like the Al and Cr samples) or stayed flat (like the Cu samples).

4.4.5.2 LHC-TAN Experiment Results

For this experiment two FCC-RADMON PCBs were mounted on an aluminum bar, as previously shown in Figure 4.16-A, and installed inside the TAN element in LHC Point 1, next to the BRAN luminosity monitors (Figure 4.16-B).

In order to estimate the radiation field experienced by the RDRs, together with several passive dosimeters, a set of RadFET dosimeters were installed in the same position as the PCBs. Since the limited range of operation of the RadFETs, as shown in Figure 4.20, only the first month of data was considered valid. From this plot it was possible to estimate a conversion factor between the luminosity and dose in the two PCBs position within the TAN element as follows:

- In PCB1 position (closer to the beam-pipe): 40 kGy per $0.5 \times 10^3 \text{ pb}^{-1}$, by directly looking at the REM130 data-points.
- In PCB2 position (farther to the beam-pipe): 10 kGy per $0.5 \times 10^3 \text{ pb}^{-1}$, by averaging the readout from the two REM250.

Such values are aligned with the radiation profile extrapolated from the passive dosimeters and simulations previously shown in Figure 3.8.

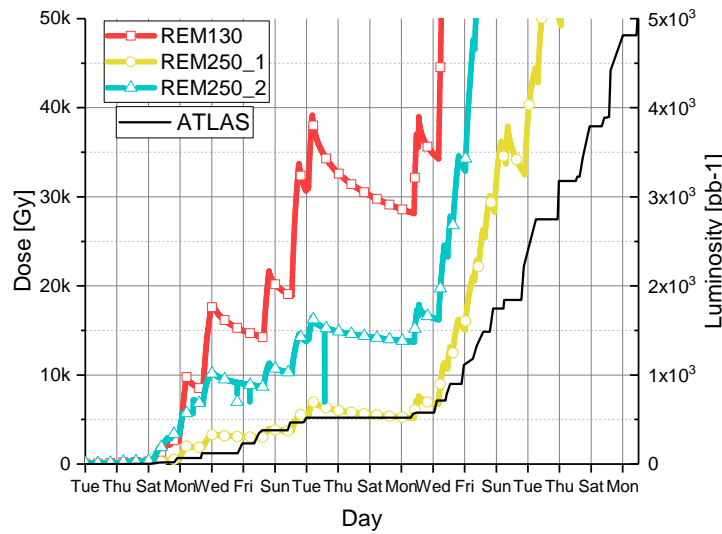


Figure 4.20 – REM250 and REM130 (RadFETs) dosimeters response to the mixed-field in the TAN element during the first days of LHC operation. The REM130 is on PCB1 (closer to the beam-pipe) while the REM250s are on PCB2 (farther from the beam-pipe). This data is used to estimate the dose (and fluence) that the RDR experienced during the whole test.

In Figure 4.21, the change in resistance (left y-axis, in %) of the measured RDRs is plotted over the time of LHC operation. In this graph, the luminosity data taken from the ATLAS

experiment was used as reference, and is plotted in black (right y-axis). All devices from PCB2 (including the NTC sensor) were functioning for the whole irradiation. Instead all signals of PCB1, a part from one, were interrupted probably due to an issue during the insertion of the sensor bar, which damaged the connecting cable. Substitution of the damaged cable was not possible since access to the LHC tunnel was already not permitted.

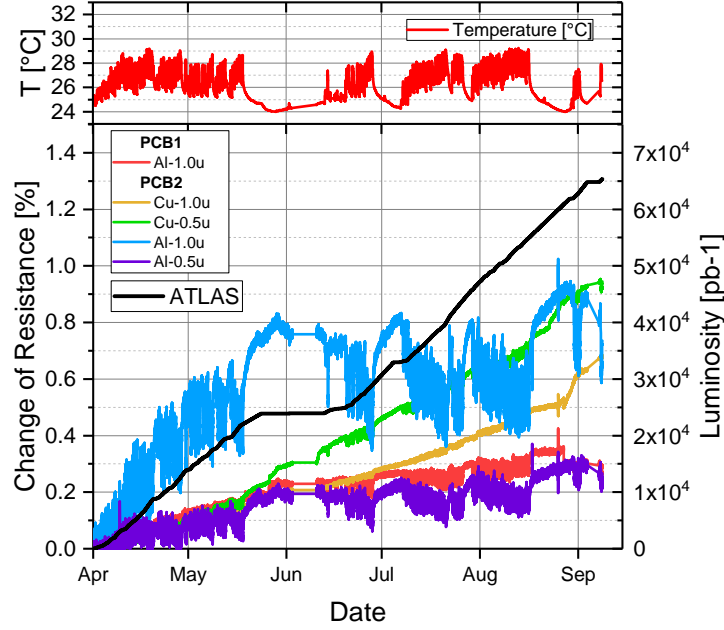


Figure 4.21 – Resistance variation from the initial value in % vs. time, for one functioning RDR on PCB1 and all RDRs on PCB2. The RDR data is compared with the integrated ATLAS luminosity (\propto particle fluence) over the same period of time. The temperature sampled with an NTC on PCB2, is shown in the top inset.

All devices have shown a change of resistance values and, as for the case of JSI, a strong correlation is seen between the temperature fluctuations and the resistance values. Since in this experiment an on-board NTC temperature sensor was soldered, a compensation of the temperature induced resistance variation was possible. In this way, as visible in Figure 4.21, the temperature induced fluctuations were well compensated for the copper samples. A similar compensation was evaluated for the aluminum samples, but that was less effective due to an apparently less accurate temperature coefficient calibration that was performed before the irradiation. Nevertheless, a good correlation can be seen between the increasing luminosity and the change of resistance.

By taking the dose/luminosity conversion factor (for PCB2) discussed before, the change of RDR resistance was plotted against dose as shown in Figure 4.22. With this plot, is possible to see that the estimated overall dose that the PCB2 has experienced during the irradiation was about 1.5 MGy, which can be considered as equivalent to a particle fluence in the order of few 10^{16} p/cm². At such relatively low particle fluence, with respect to JSI, the increase of resistance by 1% is comparable to the data measured in the nuclear reactor.

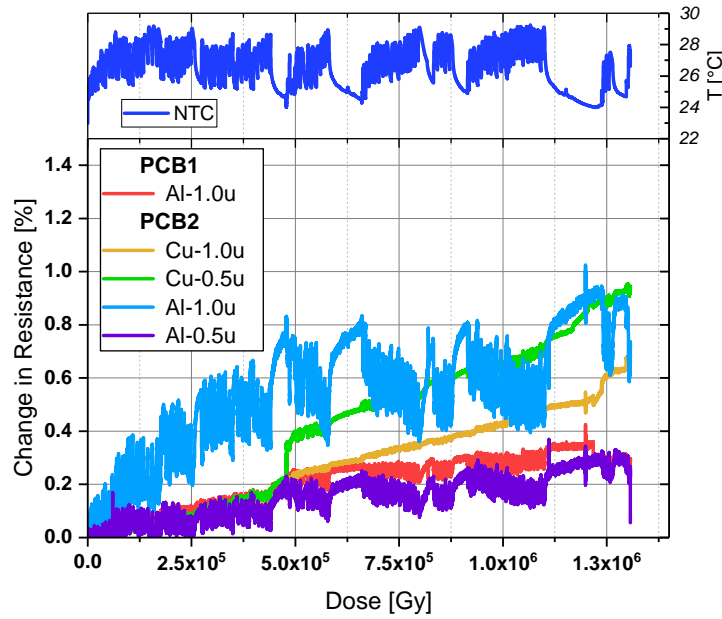


Figure 4.22 – Resistance variation from the initial value in % vs. dose, by applying a luminosity/dose conversion factor of 20 Gy/pb^{-1} as extrapolated from Figure 4.20. The abrupt increase of one RDR around $5 \times 10^5 \text{ Gy}$ is probably due to an error in the readout due to a forced reboot of the system. The temperature sampled with an NTC on PCB2, is shown in the top inset.

This irradiation experiment in a real accelerator mixed-radiation environment confirmed that RDR show a measurable resistance change, and, as for the experiment in *JS11*, it confirmed that copper samples have a larger sensitivity and more stable signal than aluminum, also in a mixed-field environment.

4.4.5.3 IRRAD-1 Experiment Results

For this experiment two FCC-RADMON PCBs were mounted on card-board sample holders, as shown in Figure 4.17-A, and installed on the irradiation table in IRRAD.

Since the IRRAD beam spot is about 10 mm in diameter, only the four RDRs located next to the connector were irradiated, while the fifth RDR (on both PCBs is the chromium sample) was getting only the tails of the Gaussian distributed beam, thus collecting a negligible total fluence with respect to the other sensors. Not measuring the Cr samples allowed freeing channels for the readout of NTC temperature sensors (as shown in 4.14-D). In addition, one of the sensors (*Al-0.5* of PCB1) experienced a failure after two months of irradiation at about $3.7 \times 10^{16} \text{ p/cm}^2$.

Figure 4.23 shows the change of resistance with increasing proton fluence for the seven RDRs (of copper or aluminum with 500 or 1000 nm thickness). The measured on-board temperature resulted stable at about 21°C ($\pm 0.5^\circ\text{C}$) over the whole irradiation period. This means that no resistance increase can be attributed to temperature variations.

4.4. Third Experimental Run: Cr/Cu/Al RDRs in JSI/LHC/IRRAD

Moreover, a set of identical RDRs were kept under measurements in the laboratory, over the same period of time at similar room temperature but without radiation, and no resistance increase was there recorded.

Therefore, the measured variation of resistance shown in Figure 4.23 can be attributed only to the impinging protons that are inducing a noticeable measurable damage. As for the results in for the JSI-1 experiment, also here the copper samples are the ones most affected by the particle fluence. In particular, the 500 nm thick copper RDR on PCB1 (*Cu-0.5u*) is showing the greater variation of almost 50 % with respect to its starting resistance, while the aluminum samples stop at about 2.5 %.

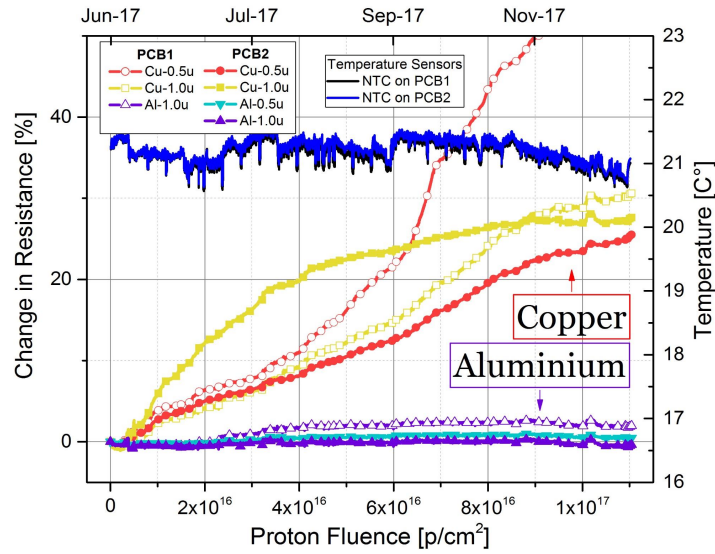


Figure 4.23 – On the left y-axis, the resistance variation from initial value in % vs the integrated particle fluence. On the right y-axis the temperature measured during the irradiation test using on-board NTC sensors (on PCB1 in black, and on PCB2 in blue).

Overall, in the range between $1 \times 10^{16} \text{ p/cm}^2$ and $5.2 \times 10^{16} \text{ p/cm}^2$ the copper RDR of PCB2 have shown an initial sensitivity of $2.1 \Omega/\Phi_p$ reduced to $0.68 \Omega/\Phi_p$ towards the end, whereas the copper samples of PCB1 have shown an acceleration of sensitivity towards the end of the irradiation. The remaining aluminum RDRs stayed at 0 % for almost half irradiation time, after which they started raising with a sensitivity of about $0.1 \Omega/\Phi_p$, where $\Phi_p = 10^{16} \text{ p/cm}^2$ for all the previously expressed sensitivities.

As also stated before for the neutron irradiation experiment, the thickness of the RDR does not affect greatly the dosimeter performance. On the other hand, the different sensitivity could be attributed to the larger number of fingers (31 instead of 13), but narrower ($30 \mu\text{m}$ instead of $40 \mu\text{m}$), once again suggesting that the top-geometry (device area) meaning the amount of exposed metal, are the key factors for trimming the dosimeter sensitivity. Differently from the logarithmic dependence of the neutron irradiated RDRs, in this case all RDRs follow a nearly linear law, apart from the *Cu-1u* of PCB2, which seems to approach saturation.

As for the *JSI-1* and *LHC-TAN* irradiations, this experiment has shown that copper experiences the greatest increase of resistance also when irradiated with a proton beam. In this case, an oxidation provoked by high-temperature (as for *JSI-1*) can be excluded, since the on-board NTC sensor measured a low temperatures during the whole experiment. Also an inefficient temperature compensation (as for *LHC-TAN*) can be excluded since the NTC sensor has measured an almost constant temperature. For this reason, for this experiment only the extreme particle fluence can be identified as primary cause for the measured increase of resistance. Nevertheless a deeper study of the oxidation process during irradiation is necessary to understand the different contributions to resistance increase.

4.4.5.4 *Third Experimental Run - Results Summary*

The main results of the *Third Experimental Run* are the following:

- *Layout is OK*: the structures designed for this *Third Experimental Run* comprising 3x3 mm² chips with a *Variable L* layout, increased area (one chip per device), and thickness (500 and 1000 nm), have shown to be optimal for the sensitivity range required. This range was shown to not be significantly impacted by the thickness of the RDR, while greater resistance increase was observed by RDRs with larger number and narrower fingers.
- *Readout is OK*: the new FCC-RADMON PCB, designed for wire-bonding the smaller chips, allowed to have the same type of support, cabling, and test-bench for all the experiments.
- *On-board temperature sensors required*: the *JSI-1* experiment has shown that a precise measurement of the temperature at which the irradiation is occurring is necessary to be able to distinguish between the resistance increase due to temperature variations from the one due to particle fluence. For this reason, an on-board NTC sensor has been mounted on the FCC-RADMON prepared for the *LHC-TAN* and *IRRAD-1* experiment of this Experimental Run.
- *Copper is the best active layer*: in all the experiments copper samples have shown a much greater increase of resistance and higher sensitivity, when compared to the chromium and aluminum.
- *Copper oxidation to be studied*: to understand the oxidation process during irradiation and the different contributions to resistance increase of temperature and radiation, a copper oxidation study using SiO₂ passivated RDRs is necessary. A passivation can isolate metal from the humidity and block the resistance increase provoked by standard copper oxidation in air under high temperature. This point is the core of the *Fourth and Final Experimental Run*.

4.5 Final Experimental Run: Cu RDR with SiO₂ in JSI&IRRAD and SEM

DESCRIPTION		METAL	LAYOUT	READOUT	RESULTS	
4 th Experimental Run	JSI-2 Neutron irradi	<ul style="list-style-type: none">Focus on Copper.Impact of SiO₂ passiv.	<ul style="list-style-type: none">Cu with Cu padst = 500 nm.Different deposition tech.SiO₂ passivation.	<ul style="list-style-type: none">3x3 mm² chips.525 chips per wafer1 device per chip.Larger W x L.	<ul style="list-style-type: none">SMU+Switch matrix.Smaller PCB.12-channel cables.Temperature sensor.	<ul style="list-style-type: none">✓ Metal type, Layout & Readout are OK✓ Increase of resistance measured only for non passivated RDR.✓ Oxidation imaged only in non-passivated RDR.✓ Collected data and images used for analysis and model definition of the RDR.
	IRRAD-2 Proton irradi.					
	SEM/FIB Observation of the RDR cross section with SEM/FIB	ANALYZED SAMPLES from 4 th Experimental Run: <ul style="list-style-type: none">Non-irradiated reference copper RDRs.Passivated and Non Passivated RDRs from JSI2.Passivated and Non Passivated RDRs from IRRAD2.				

Figure 4.24 – Summary of the Final Experimental Run.

4.5.1 Description

The *Final Experimental Run* comprises two irradiation experiments (LHC-TAN was not possible due to scheduled *LHC Long Shutdown*):

- *JSI-2*: irradiation experiment in the JSI-TRIGA nuclear reactor, performed over 5 days of irradiation up to a total neutron fluence of 5×10^{17} p/cm². The irradiation was performed at variable temperatures (measured on-board) reaching up to 80°C during the reactor operation and cooling down to 20°C overnight. A total of 10 PCBs were irradiated, with different combinations as described in the next *Material* section.
- *IRRAD-2*: irradiation experiment in the IRRAD proton facility, performed over 5 months of irradiation up to a total proton fluence of 1.2×10^{17} p/cm². The irradiation was performed at constant temperatures around 21°C during the whole irradiation. Two PCBs were irradiated as described in the next *Material* section.

Both experiments were done using only copper RDRs (with and without SiO₂ passivation), using the same layout and readout, but in different radiation environments. An additional pre and post-irradiation morphological analysis, that will be described in Section 4.5.6, was performed on the RDRs used in this *Final Experimental Run*. The electrical characterization results from the *Final Experimental Run* together with the morphological analysis, are the experimental base for the model development that will be described in Chapter 5.

4.5.2 Material

Upon the results of the previous Experimental Run, which confirmed copper as the best candidate material for RDRs, in the *Final Experimental Run* new wafers with an active layer made of 500 nm copper, whose cross-section is shown in Figure 4.25-A, were produced. Only one thickness was considered in this Experimental Run since no significant impact of the active layer thickness was found as discussed in the *Third Experimental Run*.

In addition, to disentangle the phenomenon of oxidation from the displacement damage, as discussed in the results section of the previous Experimental Run, an additional step was introduced during the RDRs fabrication in the *Final Experimental Run*: the produced copper wafers were selectively covered by sputtering a 300 nm SiO₂ passivation layer through a shadow mask, to obtain the cross-section shown in Figure 4.25-B.

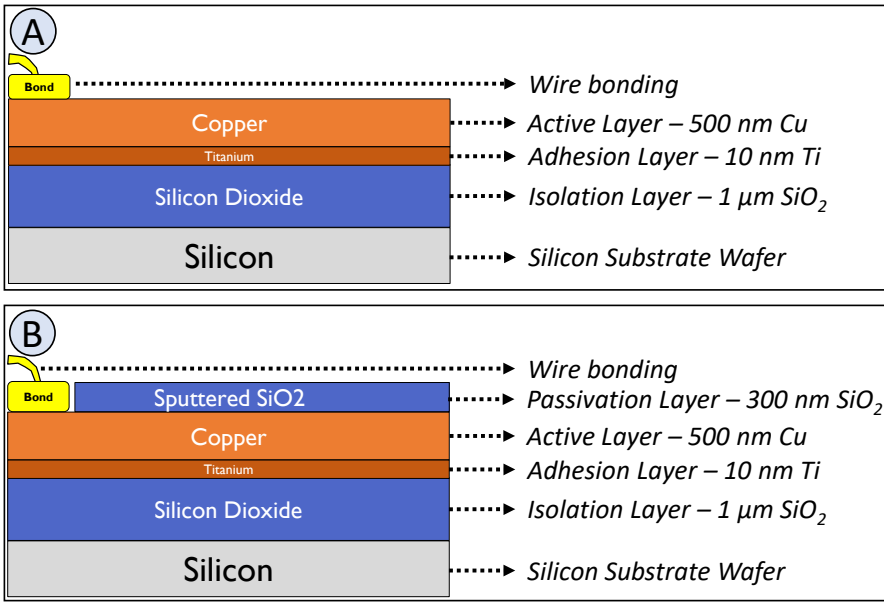


Figure 4.25 – Cross sections of the fabricated devices during the *Final Experimental Run* with active metal layer made of only Cu (A), and Cu with an additional passivation layer of SiO₂ (B).

A number of wafers were produced with different copper deposition techniques: evaporated and sputtered. This additional variable to the experiment was introduced to test its impact on the final RDR performance, since the quality of the copper film, in terms of initial resistivity, depends also on the deposition technique.

4.5.3 Layout

The size of the single RDR chip was not changed in the *Final Experimental Run* and was kept to a 3 x 3 mm² silicon chip with a single device on top.

4.5. Final Experimental Run: Cu RDR with SiO₂ in JSI&IRRAD and SEM

Figure 4.26 shows the layout of wafers produced for the *Final Experimental Run*, with the following structures:

- **Macro-groups:** 21 macro-groups per wafer, of which 10 macro-groups with width varying from 2 to 10 μm in steps of 2 μm , and 11 with width varying from 10 to 50 μm in steps of 10 μm . Additionally, 11 macro-groups were not-passivated, while 10 macro-groups were sputtered with passivating SiO₂ only on top of the active layer, and not covering the contact pads, as shown in Figure 4.26-B.
- **Chips with Single Device:** Up to 525 different resistive structures for each wafer with varying width (2 to 50 μm) and lengths (from 6 to 150 mm) as shown in Figure 4.26-B.

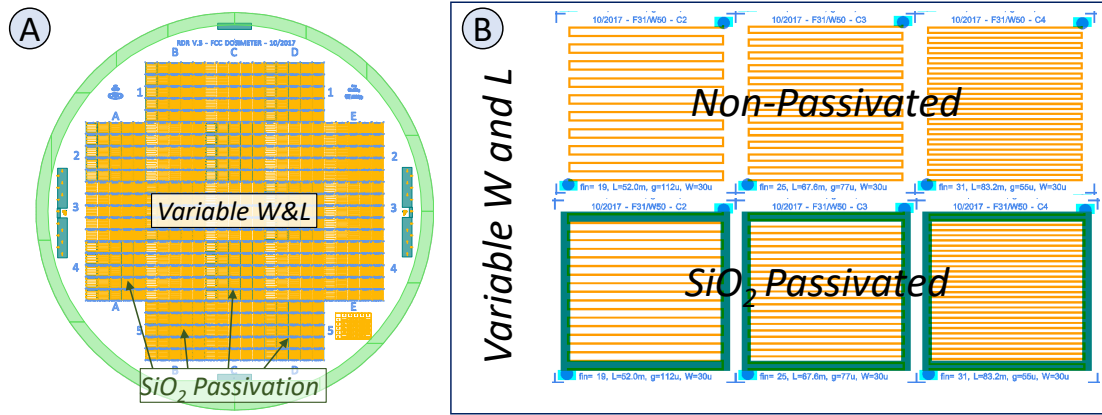


Figure 4.26 – A) Wafer layout of RDRs designed for the *Final Experimental Run* with the matrix of 16 macro groups of chips (in orange), and a subset of macro groups passivated with thorough a shadow mask with sputtered SiO₂ (in dark green). B) Example of the designed serpentine-shaped RDR chips, distinguishing the non-passivated chips (top) from the SiO₂ passivated ones (bottom), leaving the contact pads (in blue) always uncovered. Within a macro group the device width increases from bottom to top, while the length increases from left to right.

The different designed geometries (W,L) allowed obtaining final RDR resistances spanning from few Ω to hundreds Ω .

The process flow followed for the micro-fabrication of SiO₂-passivated RDRs is enlisted in Appendix E.

4.5.4 Readout

As for the previous Experimental Run, the readout procedure during both irradiation experiments of the *Final Experimental Run* has been performed online with the automatic test-bench described in Section 3.2.1.

In Figure 4.27-A, one of the produced wafers is shown with the visible purple SiO₂ passivation

Chapter 4. Experimental Runs

on a subset of macro-groups whose schematized 3D cross-section is shown in Figure 4.27-B. As done previously, also in the *Final Experimental Run* the selection of the RDRs to be mounted on the FCC-RADMON PCBs was performed by screening the several produced wafers with direct on-wafer measurements using a probe-station.

For both *JSI-2* and *IRRAD-2* experiments, an additional on-board NTC temperature sensor was included as shown in Figures 4.28-A and 4.29-A respectively.

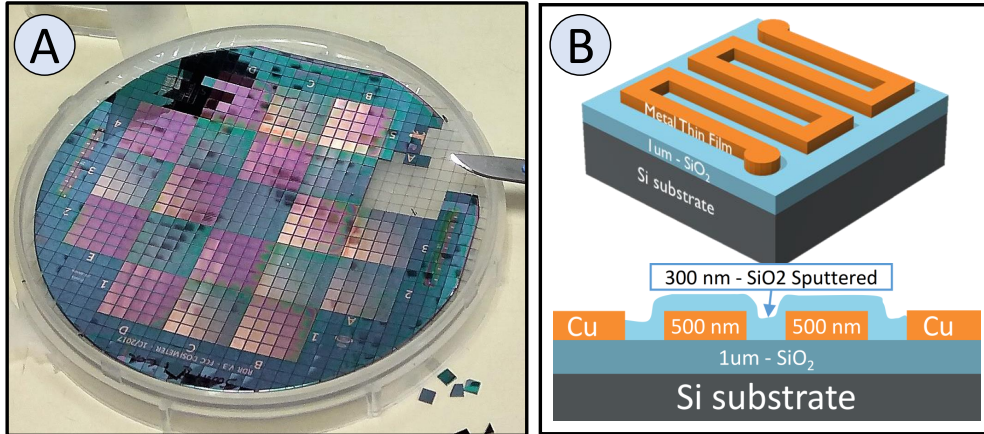


Figure 4.27 – A) One of the produced 100 mm wafers, with visible alternated SiO₂ passivation layer (in purple). B) The 3D model of a Radiation Dependent Resistor and its cross section for the passivated devices.

For the *JSI-2* irradiation experiment at the TRIGA nuclear reactor, the FCC-RADMON PCBs have been paired and piled up as shown in Figure 4.28-A and then inserted in a dedicated cylinder, in order to prevent them from scratching along the irradiation channel while being pulled down into the reactor core (shown in Figure 4.28-B).

Using 10 m long cables, the online samples were connected to two automated readout test-benches located on the top of the reactor, as shown in Figure 4.28-C.

4.5. Final Experimental Run: Cu RDR with SiO₂ in JSI&IRRAD and SEM

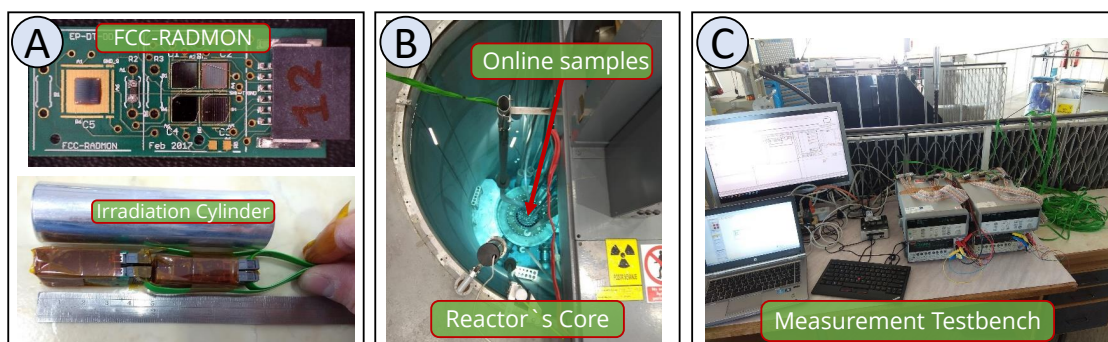


Figure 4.28 – A) On the top, one of the FCC-RADMON PCBs prepared for the JSI-2 irradiation, and on the bottom a picture of the aluminum irradiation cylinder containing where four FCC-RADMON PCBs were inserted as shown. B) Picture of the nuclear reactor's core with the opening of the irradiation channel through which the cylinder with the online samples was pulled down. C) The set of tools for the automated readout test-bench as described in Section 3.2.1 running on two PCs.

For the IRRAD-2 irradiation experiment at the IRRAD proton facility, the FCC-RADMON PCBs were mounted on a carbon fiber support and then installed on the irradiation table (shown in Figure 4.29-B). The reasons for switching from standard cardboard support to a carbon fiber one, were given in Section 3.3.2, and detailed in Appendix B.

Using the patch-panels connecting the irradiation area with the IRRAD control room (with ~30 m of cables), the FCC-RADMON were constantly monitored by the same automated readout test-bench used in the previous Experimental Runs and shown in Figure 4.29-C.

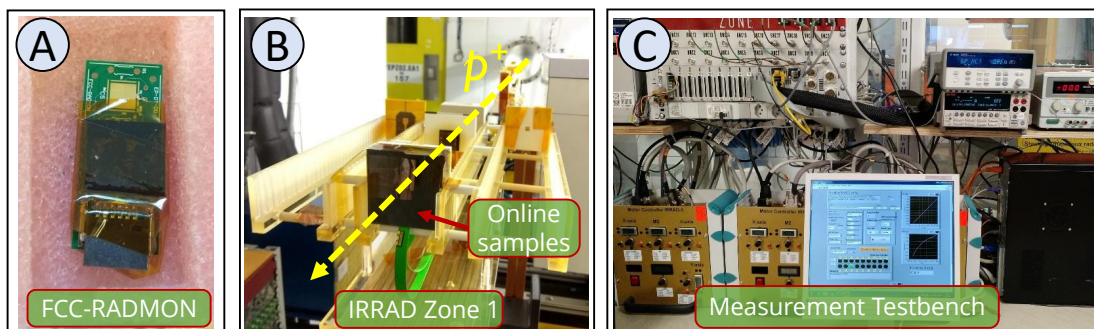


Figure 4.29 – A) Picture of the FCC-RADMON PCBs prepared for the IRRAD-2 irradiation with only 4 RDRs encapsulated with an aluminum lid and kapton tape. B) Picture of the irradiation table in IRRAD zone 1 with samples. C) The set of tools for the automated readout test-bench as described in Section 3.2.1.

4.5.5 Irradiation Tests Results

4.5.5.1 JSI-2 Experiment Results

For this experiment the FCC-RADMON PCBs were tested inside the aluminum cylinder shown in Figure 4.28-A. The cylinder was inserted inside the central channel before turning ON the reactor and measurements of each dosimeter were taken every minute. In Figure 4.30, the change in resistance (in %) of a subset of the measured RDRs is shown against the increasing total integrated neutron fluence (Φ_n).

Figure 4.30 shows initially an increase of resistance for all four devices. Such common initial behavior is explained by a resistance increase due to a jump in temperature inside the irradiation channel whenever the reactor is switched on. The top inset in Figure 4.30, shows the temperature readout from the on-board NTC sensor, which is rising from 30 °C to 100 °C at every day (ON-OFF-ON transitions).

A further change of resistance was observed only for the non-passivated IC1 and IC3 devices. Considering the irradiation period from a fluence of 0.5×10^{17} n/cm² till the end of the irradiation (to exclude the initial temperature induced resistance jump), the change in resistance of IC1 (red curve) was 0.7%. In the same period IC4 (purple curve) shown very little increase. Similarly, IC3 (cyan curve) increased by 0.5% while IC2 (yellow curve) is less than 0.1%.

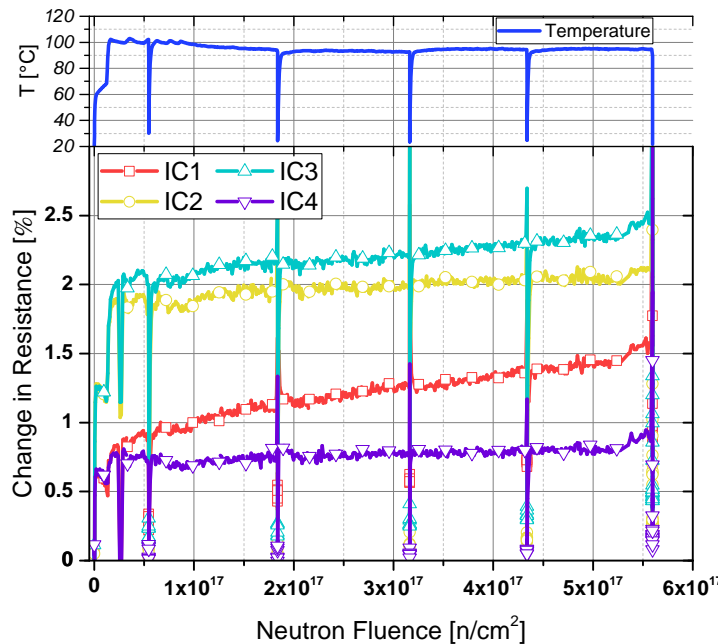


Figure 4.30 – Resistance variation from the initial value in % vs. the integrated neutron fluence, for each RDR of one of the irradiated PCBs. The negative peaks correspond to the overnight ON-OFF-ON transitions of the reactor induced by abrupt changes in temperature. The final jump after 5×10^{17} n/cm² is due to cable damage, resulted when pulling out the cylinder with the samples from the reactor's irradiation channel.

4.5. Final Experimental Run: Cu RDR with SiO₂ in JSI&IRRAD and SEM

The absence of further resistance increase in the passivated samples with respect to the non-passivated ones, suggested that the observed change of resistance of IC1 and IC3 cannot be considered as pure displacement damage in the bulk of the devices. This because the probability of neutron interaction is the same for the passivated as for the non-passivated devices. Therefore, what this experiment suggested, was that the change of resistance occurred due to an accelerated oxidation process, which normally for copper occurs at higher temperatures [58], but in this case has been accelerated by the radiation.

For this reason an additional experiment with the similar set of FCC-RADMONs was repeated in IRRAD (IRRAD2), where irradiation (although with protons) can be performed at constant and low temperature.

4.5.5.2 IRRAD-2 Experiment Results

For this experiment two FCC-RADMON PCBs were mounted on carbon-fiber sample holders as shown in Figure 4.29-B and installed on the irradiation table in IRRAD.

Since the IRRAD beam spot is about 10 mm in diameter, only the four RDRs located next to the connector were mounted and irradiated.

Additionally an NTC temperature sensor was soldered on the PCB.

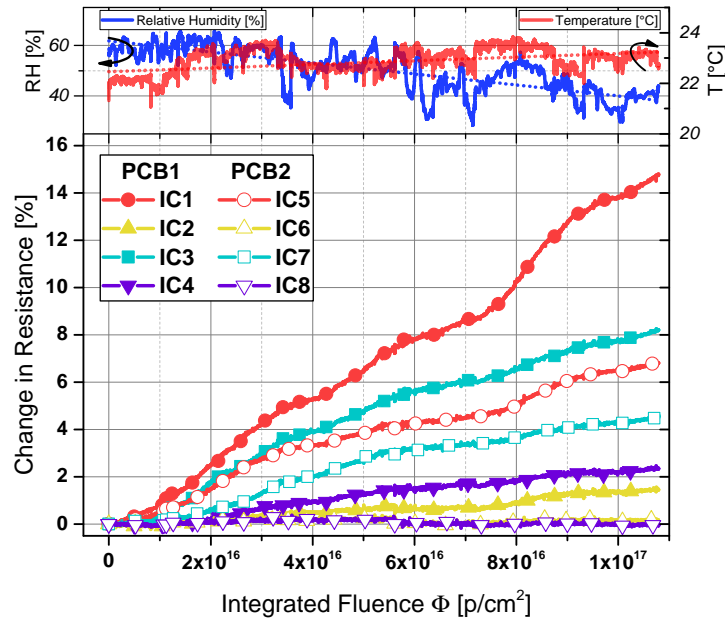


Figure 4.31 – Resistance variation with increasing integrated proton fluence of all the RDRs on the two PCBs irradiated in IRRAD (with IC1, IC3, IC5, and IC7 not passivated and IC2, IC4, IC6, and IC8 SiO₂ passivated). The relative humidity (RH) and temperature (T) are shown in the top inset.

The results from the electrical measurements performed during the IRRAD2 experiment are

shown in Figure 4.31.

By comparing the yellow and purple (triangles) curves of the RDRs with a SiO₂ passivation layer, with the non-passivated RDRs in red and cyan (circles and squares), is clear that the SiO₂ layer has a big impact in limiting the increase of resistivity of the Cu layer.

In fact, the non-passivated (uncovered) samples have increased up to 13% (+12Ω) as for the IC5 in Fig.4.31, while the SiO₂-passivated (covered) RDRs have not increase at all (IC6 and IC8), or have shown an increase of <3% (2 Ω) due to partially passivated contact pads as result of misalignment during SiO₂ sputtering. While the integrated fluence can be considered the same for all the RDRs, a wide range of resistance increase can be observed in the non-passivated samples in Figure 4.31.

Such difference in the sensitivity to radiation of the RDRs can be explained by their different geometrical shape (W, L).

As for the previous *JSI2* experiment with neutrons, also with a very high energy proton beam, the interaction probability of a thin metal film is essentially the same for both covered and uncovered RDRs, since the interaction length of 23 GeV protons in Cu and SiO₂ is several orders of magnitude larger than the RDR thickness [59].

Therefore, both types of RDRs exhibit the same likelihood of developing defects due to particles interaction, indicating also here that displacement damage is not the only responsible for the increase of resistivity.

The temperature and relative humidity (RH) were monitored during the whole irradiation, and are reported in the top inset of Fig.4.31. It is worth noticing that the increase of resistance of the uncovered RDRs has occurred at temperatures between 20 and 24 °C, much lower than the >100°C required to trigger the standard oxidation in air [58]. Moreover, even if RH has greatly varied from 60 % to 30 %, no correlation was found between the rate of resistance increase and RH variation.

As for the *JSI-2* irradiation, this experiment has shown that a significant change of resistance occurs only in devices where copper is being irradiated while directly exposed to air. This supported the hypothesis that radiation-induced processes similar to oxidation were occurring in the copper, although for sure not the known high-temperature copper oxidation that could have been experienced in the *JSI1*, since the samples in IRRAD have always been at temperatures between 20 and 24 °C.

For this reason a morphological study of these irradiated structures has been done and its discussed in Section 4.5.6.

4.5.6 Morphological Analysis

In order to study the effects of radiation on the morphology of the cross-sections, FIB milling and SEM imaging was performed on irradiated and non-irradiated samples. The irradiated samples were taken from the *JSI2* and *IRRAD2* experiments, while similar (non-irradiated)

chips were taken from the same wafers to be used as reference. Details on the setup and techniques used for milling the cross section were given in Section 3.2.2. An overview of the positioning and shape of the milled cross sections is displayed in Figure 4.32.

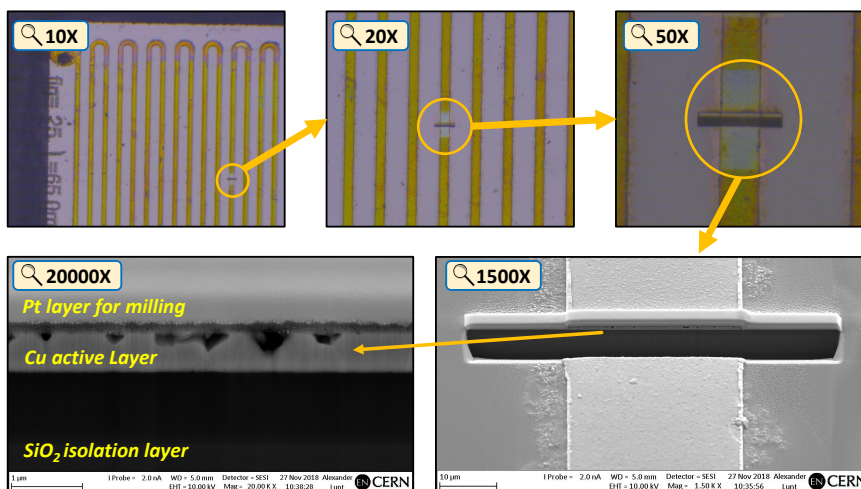


Figure 4.32 – Series of optical and SEM images of the same RDR device, zooming with an increasing magnification into the FIB milled hole.

Figures 4.33 and 4.34, compare the FIB milled cross sections of not irradiated RDRs (reference samples), both passivated and not, with the irradiated ones. Thanks to these SEM images it was possible to directly assess the radiation damage in the bulk of the RDRs that was measured electrically in the previous section.

In the images, the Cu layer can be seen sandwiched in the center, the isolation SiO₂ layer is in black, while the top most gray material is the Pt layer deposited during the FIB milling (as explained in Section 3.2.2). The cross sections of the SiO₂ passivated samples (images *e,f,g,h*) are practically identical for both irradiated and not-irradiated chips.

In contrast, the not-passivated samples (images *b* and *d*), show the presence of large voids, and growth of a uniform oxide layer on the surface (darker contrast on top of Cu), that are not present in the non-irradiated samples (images *a* and *c*). Similar results can be observed in both Figure 4.33, which shows cross sectional images from the RDRs of PCB1 irradiated in the JSI2 experiment, and Figure 4.34, which shows cross sectional images from the RDRs of PCB1 irradiated in the IRRAD2 experiment.

The formation of voids can be explained by the growth of Cu₂O and CuO oxide layers, which corroded the underlying Cu. The presence of this voids only in the non-passivated RDRs is compatible and explains the increase of resistivity measured in Figures 4.30 and 4.31. Moreover, the different increase measured for IC1 and IC3 for JSI2, and more evidently between IC1 and IC3 for IRRAD2, is compatible with what is observed in the cross sectional images, where a greater concentration of voids, and a thicker oxide layer, are seen in Figures 4.33-d and 4.34-b.

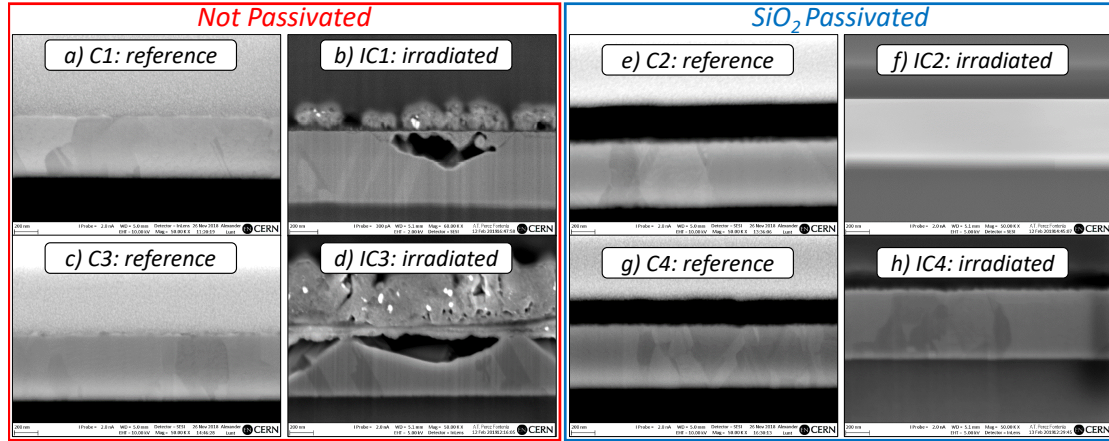


Figure 4.33 – JSI2 experiment: SEM images at 50k magnification of the cross sections of non-irradiated RDR (a,c,e,g) and irradiated ones (b,d,f,h). In red the non-passivated RDRs and in blue the SiO_2 passivated ones. Black areas are SiO_2 , gray areas with grains are Cu, and light gray areas on top are Pt.

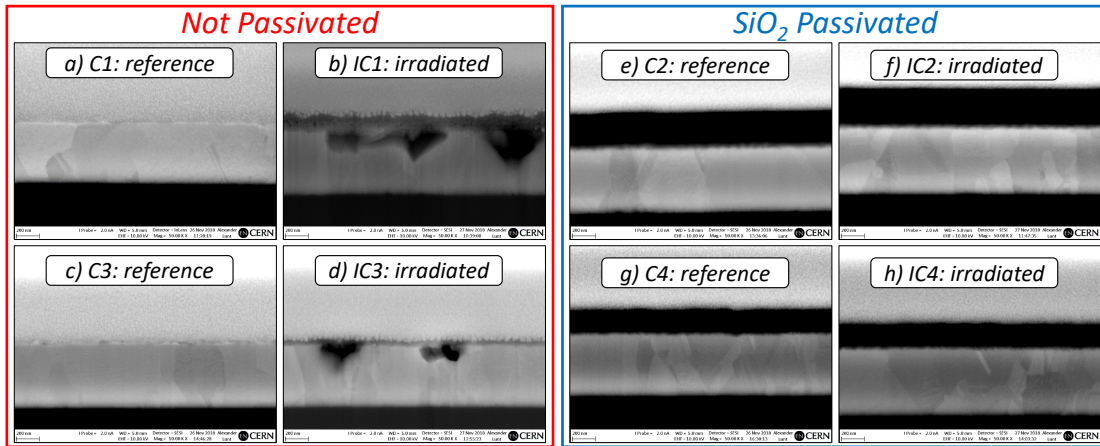


Figure 4.34 – IRRAD2 experiment: SEM images at 50k magnification of the cross sections of non-irradiated RDR (a,c,e,g) and irradiated ones (b,d,f,h). In red the non-passivated RDRs and in blue the SiO_2 passivated ones. Black areas are SiO_2 , gray areas with grains are Cu, and light gray areas on top are Pt.

These observations suggest the presence of an oxidation process, occurring in the Cu layers exposed to air, caused by the particle interaction, rather than a classic oxidation caused by a high temperature baking.

Such radiation enhanced oxidation process is explored in details in the following Chapter 5.

4.5.7 Final Experimental Run - Results Summary

The main results of the *Final Experimental Run* are the following:

- *Material is OK*: with this last iteration of RDR production copper was confirmed as the best material for very high radiation monitoring, resulting in a measurable electrical signal that depends on the amount of active layer exposed to radiation and air.
- *Layout is OK*: the 3x3 mm² chips with a *Variable L* layout and increased area (one chip per device) and thickness of 500 nm, have shown to be optimal for the sensitivity range required.
- *Readout is OK*: the new FCC-RADMON PCB designed for wire-bonding the smaller chips allowed to have the same type of support, cabling, and measurement tools for all experiments, with the possibility to run the Labview test-bench on multiple synchronized computers at the same time, with database data logging. The NTC temperature sensor was included in all the FCC-RADMON PCB to distinguish better between the resistance increase due to temperature variations from the one due to particle fluence.
- *Increase of resistance only for non passivated RDRs*: in both neutron and proton radiation environments the non-passivated copper RDRs were the only to increase their resistance value for the whole irradiation time. On the other hand, the same structures but covered with a SiO₂ passivation layer did not increase their resistance. This result prompted the morphological analysis and is the basis of the Radiation Enhanced Oxidation concept and model discussed in Chapter 5.
- *Voids and CuO/Cu₂O layer imaged only in non passivated RDRs*: the FIB milling and SEM imaging of the irradiated RDRs allowed to unveil great voids and the formation of an oxide layer only in the non passivated RDRs. These results confirmed the electrical measurements and have been used as basis of the Radiation Enhanced Oxidation concept and model discussed in Chapter 5.

All the results from this *Final Experimental Run* are the experimental basis for the model proposed in the following Chapter 5: *Models for the Radiation Enhanced Oxidation of Copper RDRs*.

MODELS FOR THE RADIATION ENHANCED OXIDATION OF COPPER RDRs

In this chapter the results from the Experimental Runs of this thesis were used to model the radiation-enhanced oxidation of copper at room temperature.

First a behavioral model is given to relate the standard copper oxidation at different atmospheric conditions with a radiation triggered oxidation, by identifying multiple mechanisms as possible phenomena governing the observed change of resistance under irradiation.

Then an analytical model is proposed to mathematically describe the growth of copper oxide as dominated by the integrated particle fluence, followed by an empirical model to predict the increase of resistance of an RDR when exposed to radiation, providing a unique lumped coefficient accounting for the radiation-enhanced oxidation.

Finally, the steps required for the RDR calibration are listed, followed by the validation of the model upon experimental data.

This chapter is based on the paper "Radiation enhanced oxidation of proton-irradiated copper thin-films: Towards a new concept of ultra-high radiation dosimetry", published on AIP Advances, vol.9, 08/2019, doi: 10.1063/1.5096606, by G. Gorine, G. Pezzullo, D. Bouvet, F. Ravotti and J.M. Sallese [60].

Contents

5.1 Behavioral Model	80
5.2 Analytical Model	82
5.3 Empirical Model	83
5.4 Dosimeter Calibration Steps and Model Validation	85

5.1 Behavioral Model

From the results of the *Final Experimental Run* described in the previous Chapter 4, the increase of resistance measured on the non-passivated copper RDRs was confirmed by the morphological inspections to be connected with the formation of great voids and the growth an oxide layer. Such observations were found for both experiments carried out with neutrons and protons, and in both constant high (~90 °C) and low (~21 °C) temperatures. In literature copper oxidation is described as a process having a parabolic dependence on temperature [58], where no significant oxide growth is seen at low temperatures such as 21 °C.

For this reason the concept of *Radiation Enhanced Oxidation* is introduced to describe the formation of voids and copper oxide growth caused by the very high radiation even at low temperatures.

Void formation has been documented in studies on copper oxidation [61, 62]. These voids were explained to be resulting from different rate of oxide nucleation along differently oriented grain boundaries, leading to a disordered growth and void creation (also known as Kirkendall voids [63]) in the bulk of the oxide layer.

Also the dynamics of copper oxidation at different atmospheric conditions have been widely covered in literature [64, 65, 66, 67]. In these works, the mechanism of copper oxidation was described in two phases. During the first phase, at low temperatures and pressures, the growth of an amorphous cuprous oxide (Cu(I)) layer occurs. In the second phase, at higher temperatures, a further oxidation into cupric oxide Cu(II) occurs. These phases are detailed in Equations 5.1 and 5.2:



These proposed mechanisms cannot explain why an oxide layer would grow even at low temperature during the irradiation of the RDRs (as shown in Chapter 4).

A behavioral model is proposed to connect the standard copper oxidation at different atmospheric conditions, with a radiation triggered oxidation where the energy required to initiate the oxidizing reactions, is given to the lattice by means of particle interactions and not only by temperature.

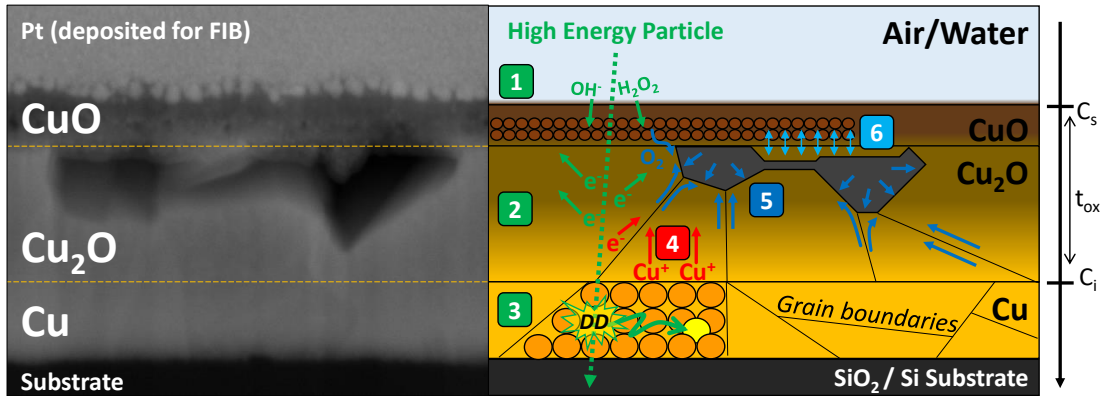


Figure 5.1 – On the left the SEM picture at 50k magnification of the non-passivated and irradiated IC1 from the IRRAD2 experiment described in Section 4.5.6. On the right the mechanisms involved in the Radiation Enhanced Oxidation under high energy particle irradiation.

A schematic illustration of the proposed mechanisms involved in the growth of a copper oxide film on a RDR under irradiation, is depicted in Figure 5.1, and can be described with the following successive phases:

1. Radiolysis of water at the surface into reactive radicals (such as H₂O₂ and OH⁻), due to ionizing energy deposition by incident particles (oxidation triggering effect not present in SiO₂ passivated samples);
2. Electrons are stripped from the oxide along the track of the incident particle;
3. Additional defects and dislocations may occur in the copper layer due to "strong" nuclear reactions (displacement damage "DD"), sputtering and diffusing copper elsewhere (necessary effect but not sufficient without #1 for oxide growth);
4. The generated copper ions and electrons diffuse toward the surface along the grain boundaries;
5. Following the Eq.5.1, Cu ions react with oxygen growing new amorphous Cu₂O along grain boundaries creating voids;
6. Further oxidation of Cu₂O into CuO occurs following Eq.5.2.

While *Phases 2&3* are mechanisms of particles interactions with metals discussed in Section 2.4 and *Phases 4&5&6* are connected to the mentioned void formation and oxide growth, *Phase 1* is similar to the radiation-triggered effects present in literature to describe the corrosion at very high gamma radiation and heat of copper containers for nuclear waste storage [68, 69, 70]. In addition, a distinction can be made between *Phases 1* to 3 which are connected to a set of Radiation Triggered Effects, and *Phases 4&5&6* which are similar to the standard oxidation of copper (at high temperature).

5.2 Analytical Model

In this section a model to describe the growth of copper oxide during irradiation is proposed. This is done by considering the flux of oxidants along the structure and the oxidizing reactions, not dependent on time, but dominated by the integrated particle fluence. This assumption of no time dependency, can be taken into account since no oxidation was observed during the same amount of time in samples measured at room temperature without radiation (see Section 4.4). Instead, samples exposed to radiation have shown a drastic oxidation even if the temperature in the irradiation chamber never exceeded 24 °C.

Therefore, the proposed model replaces time-driven fluxes with radiation-driven ones, by relating time to the equivalent cumulated particle fluence in 1 hour of irradiation in the IRRAD proton facility:

$$1 \text{ hour} = 3.6 \times 10^{12} p/cm^2 \quad (5.3)$$

As previously schematized on the right of Figure 5.1, an oxidation process is occurring at the surface of the copper RDR. A simplified view of this oxidation process, similarly to the model in [71] for silicon, and also proposed in [67] for copper, takes into account two fluxes:

1. F_1 : Diffusion through the oxide till the metal-oxide interface proportional to the gradient of oxidants concentration across the oxide ($\frac{dC}{dt_{ox}}$), and to the diffusivity of the oxidants D_{ox} .
(\rightarrow radiation enhancement in Phases from 1 to 4 in Figure 5.1);
2. F_2 : Generation of new atoms of oxide, via chemical reaction at the interface, proportional to the reaction coefficient k_i .
(\rightarrow radiation enhancement in Phases 5 and 6 in Figure 5.1);

As mentioned, these fluxes are now considered to be accelerated (enhanced) by the increasing particle fluence rather than time. The equations for each flux can be found in [71] and are:

$$\begin{cases} F_1 = D_{ox} \frac{C_s - C_i}{t_{ox}}, & \text{(diffusive flux).} \\ F_2 = k_i C_i, & \text{(reactive flux).} \\ F_1 = F_2 = F_3, & \text{(in steady state).} \end{cases} \quad (5.4)$$

By solving this system of equations:

$$\begin{aligned} F_2 = k_i C_i \rightarrow C_i &= \frac{F_2}{k_i} \\ F_1 = D_{ox} \frac{C_s - C_i}{t_{ox}} &= D_{ox} \frac{C_s - \frac{F_2}{k_i}}{t_{ox}} \rightarrow F_1 t_{ox} = D_{ox} C_s - D_{ox} \frac{F_2}{k_i} \end{aligned} \quad (5.5)$$

and assuming the steady state condition $F = F_1 = F_2$ is possible to solve this set of equations

obtaining the overall flux of oxidants:

$$F_1 t_{ox} = D_{ox} C_s - D_{ox} \frac{F_2}{k_i} \rightarrow F = \frac{D_{ox} C_s}{\left(t_{ox} + \frac{D_{ox}}{k_i}\right)} \quad (5.6)$$

from which the growth rate of the oxide layer with respect to the particle fluence $\frac{dt_{ox}}{d\phi}$ can be calculated as the ratio between the flux of oxidants F (in Eq.5.6), and the total number of available oxidants C_{tot} , obtaining the following differential equation:

$$\frac{dt_{ox}}{d\phi} = \frac{F}{C_{tot}} = \frac{1}{C_{tot}} \frac{D_{ox} C_s}{\left(t_{ox} + \frac{D_{ox}}{k_i}\right)} \quad (5.7)$$

and solving Eq.5.7 by integration with the initial condition of $t_{ox} = 0$ at $\phi = 0$:

$$\begin{aligned} \int_0^{t_{ox}} \left(t_{ox} + \frac{D_{ox}}{k_i}\right) dt_{ox} &= \int_0^{\Phi} \left(\frac{D_{ox} C_s}{C_{tot}}\right) d\Phi \\ \Rightarrow t_{ox}^2 + \underbrace{\frac{2D_{ox}}{k_i}}_A t_{ox} - \underbrace{\frac{2D_{ox} C_s}{C_{tot}}}_{B} \phi &= 0 \end{aligned} \quad (5.8)$$

with $A = 2D_{ox}/k_i$ and $B = 2D_{ox}C_s/C_{tot}$.

Finally, this quadratic equation leads to two solutions depending on the magnitude of Φ :

$$t_{ox} = \begin{cases} \frac{B}{A}\Phi, & \text{for small } \Phi. \\ \sqrt{B\Phi}, & \text{for large } \Phi. \end{cases} \quad (5.9)$$

revealing two modes of oxidation, an initial linear oxide growth dominated by the reaction coefficient k_i , followed by a parabolic behaviour driven by the diffusion coefficient D_{ox} .

These results that relate the oxide thickness t_{ox} to the integrated particle fluence Φ are the base for the *Empirical Model* described in the following Section 5.3 and will be used to extract the radiation enhanced oxidation coefficient β .

5.3 Empirical Model

In this section, we propose an additional model to predict the increase of resistance of an RDR when exposed to radiation. As verified by the several Experimental Runs described in Chapter 4, the main hypothesis of this model is that the resistance of an RDR is linearly

dependent only on temperature (T) and fluence (Φ). This can be written as:

$$R(T, \Phi) = R(\Phi)(1 + \alpha \Delta T) \quad (5.10)$$

where $R(\Phi)$ is the resistance value increasing with fluence, α is the linear temperature coefficient, and ΔT is the increase of temperature from 0°C .

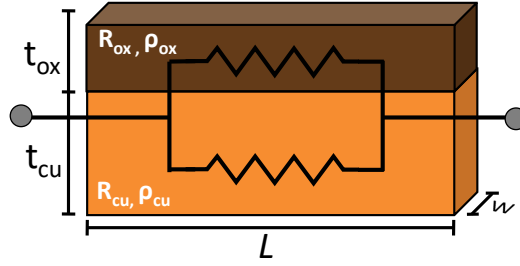


Figure 5.2 – Circuit of $R(\Phi)$ calculated as parallel resistance between the growing Cu_2O layer and the shrinking Cu layer

As shown in Figure 5.2, $R(\Phi)$ can be considered as the parallel resistance between the growing Cu_2O layer and the shrinking Cu layer, as follows:

$$R(\Phi) = R_{ox} \parallel R_{cu} \quad \text{with:} \quad (5.11)$$

$$R_{ox} = \frac{L}{W} \frac{\rho_{ox}}{t_{ox}}; \quad R_{cu} = \frac{L}{W} \frac{\rho_{cu}}{t_{cu}} \quad (5.12)$$

where L and W are design parameters of the RDR, ρ_{ox} and t_{ox} are respectively the resistivity and thickness of the copper oxide, while ρ_{cu} and t_{cu} are the ones of the copper.

By expressing the total thickness t as $t = t_{cu} + 0.3 t_{ox}$ (see calculations in Appendix C), solving Eq. 5.11:

$$\begin{aligned} R(\Phi) &= \frac{1}{\frac{1}{R_{ox}} + \frac{1}{R_{cu}}} = \frac{L}{W} \frac{1}{\frac{t_{ox}}{\rho_{ox}} + \frac{t_{cu}}{\rho_{cu}}} = \frac{L}{W} \frac{\rho_{ox}\rho_{cu}}{\rho_{cu}t_{ox} + \rho_{ox}t_{cu}} \xrightarrow{\text{using Eq.5.12}} \frac{L}{W} \frac{\rho_{ox}\rho_{cu}}{\rho_{cu}t_{ox} + \rho_{ox}t - 0.3\rho_{ox}t_{ox}} \\ &= \frac{L}{W} \frac{\rho_{cu}}{t} \cdot \frac{\rho_{ox}}{\rho_{ox} + \frac{t_{ox}}{t}(\rho_{cu} - 0.3\rho_{ox})} = R_0 \frac{1}{1 + \frac{t_{ox}}{t} \frac{(\rho_{cu} - 0.3\rho_{ox})}{\rho_{ox}}} \end{aligned} \quad (5.13)$$

and by simplifying the ratio $(\rho_{cu} - 0.3\rho_{ox})/\rho_{ox} \approx -0.3$ (since $\rho_{ox} \gg \rho_{cu}$ [72]), is possible to rewrite $R(\Phi)$ in Eq. 5.13, and express it as first order Taylor series approximation:

$$R(\Phi) = R_0 \frac{1}{1 - 0.3 \frac{t_{ox}}{t}} = R_0 \sum_{n=0}^{\infty} \left(0.3 \frac{t_{ox}}{t} \right)^n \approx R_0 \left(1 + 0.3 \frac{t_{ox}}{t} \right) \quad (5.14)$$

5.4. Dosimeter Calibration Steps and Model Validation

where $R_0 = \frac{L}{W} \frac{\rho_{cu}}{t}$ is the RDR resistance at 0°C and $\Phi = 0$, t is the initial thickness, and t_{ox} is the radiation dependent oxide thickness calculated in Eq. 5.9. For a simpler model, only the linear expression of t_{ox} is considered (see Appendix D). By taking the case of small Φ ($t_{ox} = \frac{B}{A}\Phi$), equation Eq.5.14 becomes:

$$R(\Phi) = R_0 \left(1 + \frac{0.3}{\beta} \frac{B}{t} \frac{A}{A} \Phi \right) = R_0 (1 + \beta \Phi) \quad (5.15)$$

with $\beta = \frac{0.3}{t} \frac{B}{A}$ which is the linear radiation enhanced oxidation coefficient.

As will be validated in the next Section 5.4, β can be extracted by a linear fit of the temperature-corrected resistance variation during irradiation, and by finally rewriting Eq. 5.10, an estimate of the integrated fluence Φ can be obtained as:

$$\Phi = \left(\frac{R(T, \Phi)}{R_0(1 + \alpha \Delta T)} - 1 \right) \frac{1}{\beta} \Rightarrow \Phi = \left(\frac{R_{RDR}}{R_T} - 1 \right) \frac{1}{\beta} \quad (5.16)$$

where $R_{RDR} = R(T, \Phi)$ is the experimentally measured resistance of the RDR, and $R_T = R_0(1 + \alpha \Delta T)$ is the temperature dependent resistance calculated from the measured temperature and RDR resistance at 0°C R_0 .

5.4 Dosimeter Calibration Steps and Model Validation

The empirical model is the starting point for using the RDR as a dosimeter, since it allows to relate the physical quantity (input stimulus) of the integrated particle fluence (Φ) with the measurable electrical signal (R_{RDR}), as schematized in Figure 5.3.

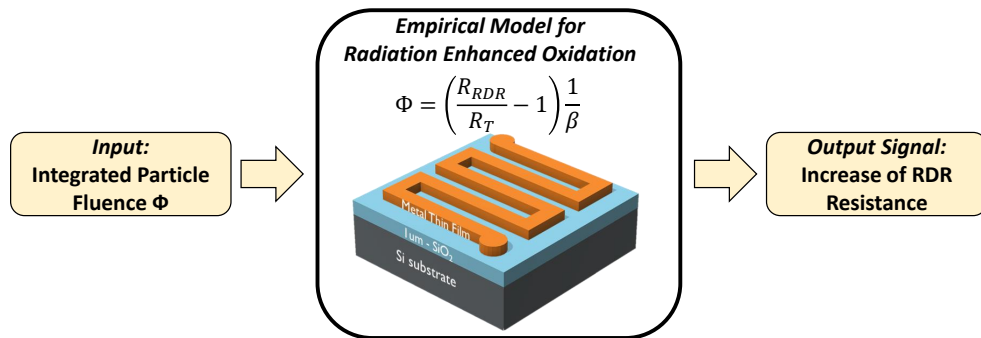


Figure 5.3 – Schematic of the Radiation Dependent Resistor used as transducer from the physical input Φ into the electrical output signal R_{RDR} using the results developed in the empirical model in Section 5.3.

The empirical linear model requires two coefficients for which the following calibrations have to be performed prior using the RDR as a stand-alone dosimeter:

- *Temperature calibration:* the α temperature coefficient of the RDR is obtained, prior irradiation, by fitting the resistance variation during a temperature sweep (e.g. from -10 °C to +10 °C).
- *Sensitivity calibration:* the β linear coefficient of the RDR is extrapolated by a initial irradiation in a controlled environment up to a particle fluence of 2×10^{16} p/cm².

The temperature calibration was performed on the FCC-RADMON PCBs before the *IRRAD2* irradiation experiment (Section 4.5), and the obtained α values are shown in Table 5.1. The linear β coefficient instead was calculated fitting the initial electrical data collected during the *IRRAD2* irradiation test, and the obtained β values are also shown in Table 5.1.

	Tag	R ₀ [Ω]	α [1/°C]	β [cm ² /p]
PCB1	IC1	73.36	0.00391	8.59×10^{-17}
	IC3	59.28	0.00377	3.49×10^{-17}
PCB2	IC5	139.93	0.00379	1.48×10^{-16}
	IC7	77.41	0.00361	1.12×10^{-16}

Table 5.1 – Extracted temperature coefficients α and radiation coefficients β , for the different non passivated Cu RDRs irradiated in *IRRAD2* and described in Section 4.5.

As displayed in Figure 5.4, only the initial data-points in blue (from 1×10^{16} p/cm² to 2×10^{16} p/cm²) were used to extrapolate the β coefficient and plot the linear fit (red dashed line). The first data-points (from 0 p/cm² to 1×10^{16} p/cm²) were excluded because found to be inconsistent with the overall linear increase. This initial inconsistency is very similar to the one found in the Deal-Groove model [71] for silicon, which similarly cannot be used to describe the initial oxidation phase.

In practice, such β coefficient calibration can be obtained by measuring the cumulated fluence using another reference dosimeter (e.g. silicon diode) located in the same position of the RDR, and once the reference dosimeter saturates, the now calibrated RDR can be used instead. In this way the calibration data points will be collected in the same radiation environment as the consecutive dosimetry data points.

Finally Figure 5.4, compares the obtained fits with the actual measured data. The related error distributions, calculated as difference between the measured fluence and the ones obtained from the model, are shown in Figure 5.5. The summary statistics, enlisted in Table 5.2, shows a mean error of less than 10% for IC1, IC5, and IC7, with a standard deviation less than 15%, indicating a good agreement between the model and the real data. The mean error for IC3 is bigger but, the empirical model was developed to get the simplest equations (linear) to correlate resistance variation with fluence, thus not allowing to well follow nonlinearities. Nevertheless the obtained average error shows that a linear model can predict the behaviour

5.4. Dosimeter Calibration Steps and Model Validation

of an RDR with an enough good precision for most common dosimetry applications. A refinement to the model could be done by taking into account the two modes of oxide growth expressed in Eq. 5.9, leading to a more precise model but not applicable in practice (as discussed in Appendix D), and other improvements proposed in the *Future Work* Section 6.2.

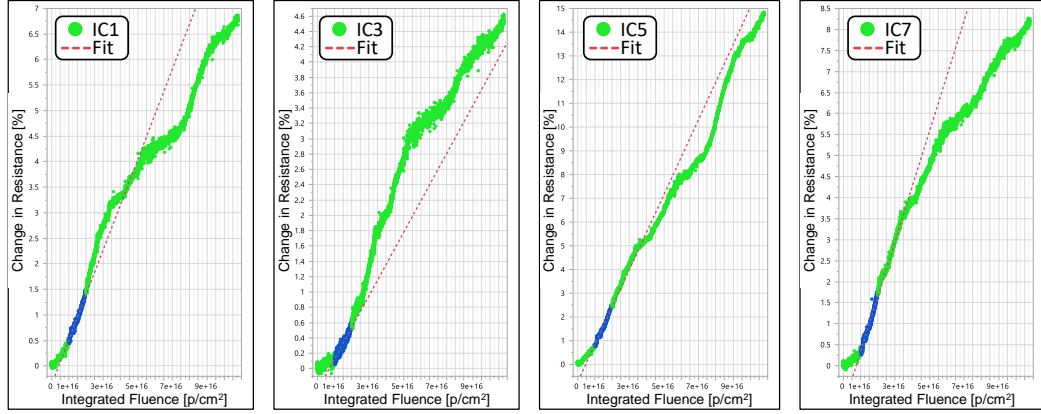


Figure 5.4 – Extraction of the radiation enhanced oxidation coefficient β (listed in Table 5.1), by linearly fitting the initial subset (in blue) of the normalized resistance variation $100 \times \frac{R(T,\Phi) - R_T}{R_T}$ with increasing particle fluence.

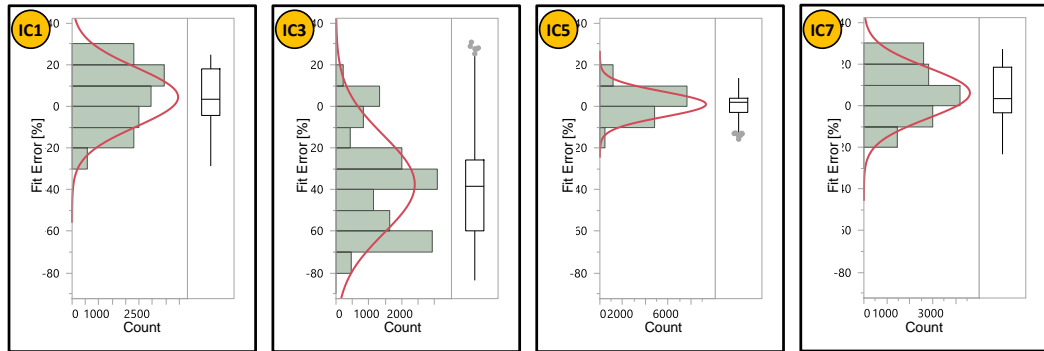


Figure 5.5 – Error distributions (expressed in percentage), calculated as difference between the measured fluence and the ones obtained from the model for each RDR (as shown in Figure 5.4). The summary statistics of the error distributions are shown in Table 5.2.

	IC1	IC3	IC5	IC7
Mean [%]	4.5	-37.5	1.0	6.2
Std Dev [%]	14.2	23.5	6.0	12.1
Std Err Mean [%]	0.1	0.2	0.1	0.1
Upper 95% Mean [%]	4.7	-37.1	1.1	6.4
Lower 95% Mean [%]	4.3	-37.9	0.9	6.0

Table 5.2 – Summary statistics of the error distributions shown in Figure 5.5.

CONCLUSIONS AND PERSPECTIVES

This concluding chapter enlists the achievements and results obtained in this thesis highlighting the main and the additional contributions.

Then the possible future research steps for the optimization of this technology are given.

Finally a list is given for the proposed current and future application envisioned for the RDR sensor technology and the model of Radiation Enhanced Oxidation of copper at room temperature.

Contents

6.1 Conclusions	90
6.2 Future Work	94
6.3 Perspectives	95

6.1 Conclusions

An innovative radiation sensor technology based on metals and the new theory of Radiation Enhanced Oxidation for copper are the main results of this thesis.

An extensive experimental work was done to study and prototype a radiation sensor called Radiation Dependent Resistor, which working principle is based on radiation-induced permanent change in resistivity of the metal thin film.

The *First and Second Experimental Runs* were focused on the optimization of the layout design, micro-fabrication process, and readout system. These phases resulted in the production of 3x3 mm² chips, to be mounted on the special radiation-hard FCC-RADMON PCB allowing to perform online measurements during irradiation.

In the *Third Experimental Run* different pre-selected metals for the active layer were tested. Several RDRs made of chromium, aluminum and copper, of different sizes and thickness were tested in a neutron, mixed-field, and proton environments. The collected experimental data has shown a variation of resistivity with increasing radiation in all the tested environments. This confirming our concept of a dosimeter based on metal thin films. In particular copper was found to be the best material for the RDR in terms of resistance increase and sensitivity to radiation.

The *Final Experimental Run* was dedicated to the understanding of the copper oxidation process during irradiation and the different contributions to resistance increase of temperature and radiation, by testing copper RDRs with and without a SiO₂ passivation layer. These devices were also tested in a neutron and proton environments.

Additionally to assess the resistance increase during irradiation measured only in the non SiO₂ passivated RDRs, a morphological analysis was performed before and after irradiation. This SEM imaging of the cross sections has revealed areas with grown copper oxides (Cu₂O and CuO) and large voids, only in the non-passivated devices which have shown the greater resistance increase.

Such increase was explained by the corrosion of the copper layer as result of chemical and nuclear processes induced by the interaction with energetic particles.

As result, it was suggested to relate the conventional copper oxidation at high temperature to a new concept of Radiation Enhanced Oxidation at room temperature.

A behavioural model was proposed describing the radiation enhanced diffusion rate of oxidants across the forming oxide layer (due to water radiolysis at the surface and electron emission in the oxide), and the radiation enhanced chemical reaction at the interface (due to the induced displacement damage in the copper lattice).

Then, an analytical model was given to quantify the thickness of the grown copper oxide layer depending on the integrated fluence.

Following, an empirical model was created to account for the resistance variation of copper films due to temperature shifts (α) and increasing integrated particle fluence (β), which applicability is foreseen in the field of dosimetry in form of Radiation Dependent Resistors.

Finally, the calibration steps of the RDR to define the α and β coefficients for the empirical model were given and a model validation was performed comparing the fluence values calculated using the model with the real ones from the experimental measurements, showing good results with a mean error within $\pm 10\%$ for most of the samples.

In summary, the main contributions of this research can be outlined as follows:

- **Analysis of metals to use as active layer:**
 - Choice based on the metal properties and availability as sputtering targets (Section 2.5.1).
- **Selection of copper as best metal for active layer:**
 - Copper have shown a much greater increase of resistance and higher sensitivity, when compared to the chromium and aluminum (Section 4.4).
- **Performed very high fluence irradiation tests with neutrons at JSI Nuclear Reactor:**
 - *JSI1* test on chromium, aluminum, and copper RDRs during the Third Experimental Run (Section 4.4).
 - *JSI2* test on SiO₂-passivated and non-passivated copper RDRs during the Final Experimental Run (Section 4.5).
- **Performed one irradiation test in the mixed-radiation field of the LHC accelerator:**
 - *LHC-TAN* tested Cu and Al RDRs from the Third Experimental Run (Section 4.4).
- **Performed very high fluence irradiation tests with protons at CERN-IRRAD:**
 - *IRRAD0* test on chromium RDRs during the First (Section 4.2) and Second Experimental Runs (Section 4.3).
 - *IRRAD1* test on chromium, aluminum, and copper RDRs during the Third Experimental Run (Section 4.4).
 - *IRRAD2* test on SiO₂-passivated and non-passivated copper RDRs during the Final Experimental Run (Section 4.5).
- **Extensive research for radiation damage on thin metal films:**
 - No previous research was ever focused in amplifying the resistivity variation due to radiation damage in metal thin films and exploit this as dosimeter (Section 2.4).
- **Development of an Analytical Model for the Radiation Enhanced Oxidation:**
 - Proposed time independent and radiation-driven relationship between oxide

thickness t_{ox} and integrated particle fluence Φ (Section 5.2).

- **Development of an Empirical Model for the Radiation Enhanced Oxidation:**
 - Defined a mathematical equation to estimate the integrated particle fluence based on the experimentally measured resistance and temperature of the RDR (Section 5.3).
- **Definition of RDR calibration steps and validation of the Empirical Model:**
 - Enlisted the calibration steps to measure the temperature coefficient α and radiation enhanced oxidation coefficient β required by the empirical model (Section 5.4).
 - Validated the empirical model equations by comparing the experimental data from *IRRAD2* with those predicted by the model resulting in a mean error <10% for most samples (Section 5.4).
- **Study of the impact of metal thickness and area on RDR sensitivity:**
 - Optimal sensitivity range was found in thicker and larger area RDRs (Section 4.4).
- **Design and validation of RDR micro-fabrication process:**
 - Validated process flow in Appendix E.
- **Study of different electrical behavior during irradiation for SiO₂ passivated and non passivated copper RDR:**
 - Increase of resistance only for non-passivated RDR suggesting the presence of a radiation enhanced oxidation (Section 4.5).

There are also additional contributions done during this thesis:

- **Radiation damage simulations in Cr, Al, and Cu:**
 - FLUKA simulations show higher DPA generation in Cu (with protons) and Al (with neutrons) (Section 2.5.2).
- **Comparison and analysis of cross-sectional SEM images of irradiated and non irradiated RDRs:**
 - Voids and CuO/Cu₂O layer imaged only in non passivated RDRs (Section 4.5.6).
- **Conceptualization of the Radiation Enhanced Oxidation theory with the Behavioral Model:**
 - Identified main chemical and physical processes responsible for radiation triggered formation of voids and growth of copper oxide (Section 5.1).
- **Conception of optimal RDR layout for irradiation test:**
 - Final layout defined in *Third Experimental Run* (Section 4.4).

- **Selection and realization of the optimal contact pad stack for bondability:**
 - Aluminum or copper contact pads were chosen (Section 4.3).
- **Development of a radiation-hard FCC-RADMON PCB and choice of carbon fiber sample holders:**
 - Special PCB substrate selected for long-irradiation tests (Section 3.3.1).
 - On-board NTC sensor for temperature monitoring during irradiation (Section 4.4).
 - Carbon-fiber sample-holder in IRRAD less brittle and radioactive than cardboard (Section 3.3.2).
- **Design and implementation of an online Labview-based readout test-bench:**
 - Automatic measurement test-bench for wired monitoring of the RDR resistance (Section 3.2.1).
 - Scalable test-bench for readout of multiple FCC-RADMON PCBs and data logging on online database (Section 3.2.1).

6.2 Future Work

The most important research paths and future investigations directly related to the work presented in this thesis are:

- **Investigation of the impact of humidity on the Cu oxidation rate and include it in the analytical model of Radiation Enhanced Oxidation:**

An additional refinement to the Radiation Enhanced Oxidation model would be to consider the effects of varying air-humidity, even if, at low temperature, such effect has been proven to be not dominant (Section 4.5). Nevertheless, as reported in literature [73] for standard copper oxidation at high temperature, relative humidity (RH) can increase the oxidation rate by +50% when oxidizing at 30% RH instead of 0% RH. Such dependence on the relative humidity could be taken into account by including a logarithmic term into the radiation enhanced oxidation coefficient β in Eq.5.10.

- **Production and irradiation of new RDRs to further understand the impact of geometrical parameters on the Radiation Enhanced Oxidation β coefficient:**

Chemical reactions in the empirical model described in Section 5.3 strongly depend on the quality of the deposited copper (size and shape of the Cu grains determine the oxidants diffusivity), so the larger the surface ($W \times L$) the smaller the impact of defects in the Cu layer. New irradiation tests performed on very large devices (compared to the $3 \times 3 \text{ mm}^2$ RDR in this thesis) could show a significant difference in the β coefficient therefore different RDR sensitivity. These assumptions can be checked with such dedicated test.

- **Irradiation test at different particles rate (flux) on copper RDR to study on RDR sensitivity and β coefficient in the Radiation Enhanced Oxidation model:**

Similarly to silicon based dosimeters, the RDRs may be prone to a dose-rate effect where the speed at which the dosimeters integrates the particle fluence affects its sensitivity. Since such effect is known to be affecting the readout deviation in any dosimeter, a dedicated study could be performed when concluding the full characterization of the RDR technology.

- **Evaluation of copper RDRs (with on-board temperature sensor) in the mixed-radiation environment of a real accelerator like in the Large Hadron Collider at CERN:**

As mentioned in Section 4.4, a test inside a *real* accelerator environment was possible only for samples produced in the *Third Exp. Run*. Because of the planned LHC long shut-down (LS2, from 11/2018 to mid-2021), another test with the passivated RDR from the *Final Exp. Run*, was not possible. Once the LHC will be restarted, it could be useful to perform such irradiation test in the LHC, with the latest version of RDRs and evaluate the Radiation Enhanced Oxidation of copper RDR in the mixed-radiation field.

6.3 Perspectives

The following possible applications could be foreseen for the Radiation Enhanced Oxidation of copper and the Radiation Dependent Resistor:

- **Dosimeter for the FCC very high radiation environment:**

This is the main application envisioned from the beginning of this thesis project supported by the CERN Future Circular Collider collaboration. The researched RDR are a valid candidate technology to replace today's silicon-based dosimeters used in the LHC and become the new FCC standard dosimeter.

- **RDRs with selective SiO₂ patterning:**

By patterning a protective SiO₂-passivation area, leaving uncovered only some sections of the device, the RDR can be engineered to target the sensitivity range of the specific application, such as in high energy physics (as the above point), for space applications (with lower radiation levels than FCC) or nuclear and fusion energy (with even higher radiation levels).

- **Low cost integrated dosimeter:**

Another application for the RDR would be as very low cost radiation sensor whose simple fabrication process can be included in the design of more complex chips and devices. This would allow to have monolithic integrated circuits with the readout circuitry and radiation sensor in the same chip.

- **Alternative readout technique:**

The main foreseen application for the RDR is as resistive sensors, but due to the surface oxidation and formation of voids, even if a being a more expensive solution, an optical readout could be taken into account. An option could be to coat the tip of an optical fiber with a thin layer of copper and exploit the change in reflectivity as indicator of the increasing integrated fluence.

IRRADIATION FACILITIES DATABASE

The following main specifications were taken into account for the development of the reference website hosting the Irradiation Facilities Database:

1. Creation of a reference database of irradiation facilities at CERN, EU and Worldwide, to provide all in one table a unique and official list of available facilities around the world.
2. Display, in a concise but exhaustive way, a description of the facility, with information spacing from the standard contact names and addresses, to more technical one concerning radiation safety details and irradiation facility services and requirements.
3. Implementation of an auto-maintenance routine to trigger an update request to all the facilities responsible, thus avoiding outdated and confusing data being stored indefinitely in the database.

A picture displaying the homepage of the realised website is shown in Figure A.1 alongside with the different clickable subpages with the CERN facilities, with the Database Access, and the map displaying all the facilities currently in the database.

The main section of the website is the database that contains all the information about the different available irradiation facilities around the world relevant for high-energy physics applications. The search-panel allows applying some basic filtering to all the facilities stored in the database. In particular, the user can search by:

- *Country*: to select the just the facilities of a chosen country;
- *Source Type*: to list all the facilities providing a particular type of source of radiation (e.g. Co-60, Cs-137, Synchrotron, Nuclear Reactor, etc.);
- *Radiation Field/Type*: to filter the facilities by the means of irradiation (e.g. protons, neutrons, gamma rays, electrons, mixed field, etc.).

By clicking on “*Show Data*”, the webpage automatically performs a query on the MySQL database and displays the requested data as depicted in Figure A.2-B. This displayed data contains only a subset of all the information that are actually stored for each facility. This choice was done to limit the amount of data displayed and ease the visualization of the filtered facilities. In fact, at this stage, the user can additionally refine the search by ordering the desired column, clicking on the arrows next to the column names, or, if interested in having the complete information about a particular facility, he/she can click on the details icon to have a complete printable table.

Appendix A. Irradiation Facilities Database

Up to today the Irradiation Facilities Database hosts more than 200 facilities, becoming the reference "search engine" for irradiation facilities for the high energy physics community. The website can be accessed at www.cern.ch/irradiation-facilities.

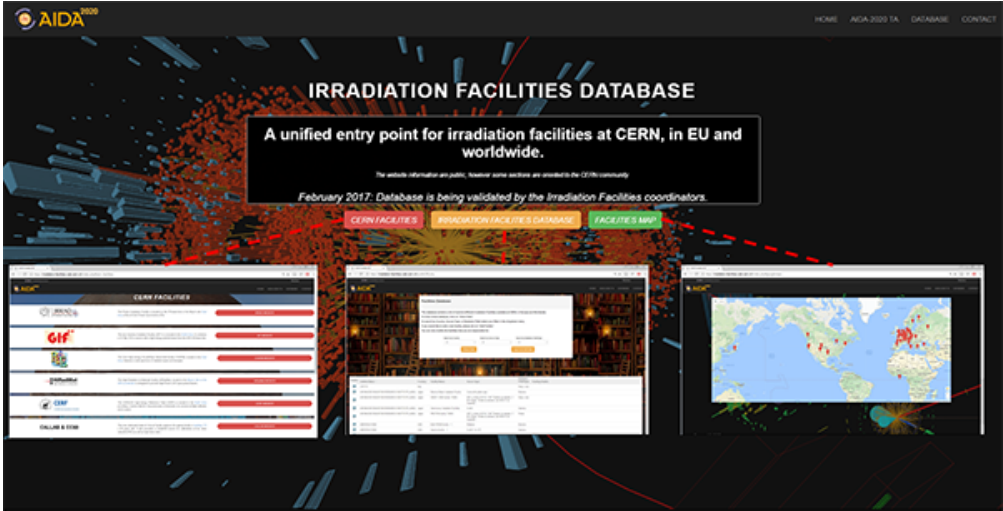


Figure A.1 – Homepage available at www.cern.ch/irradiation-facilities

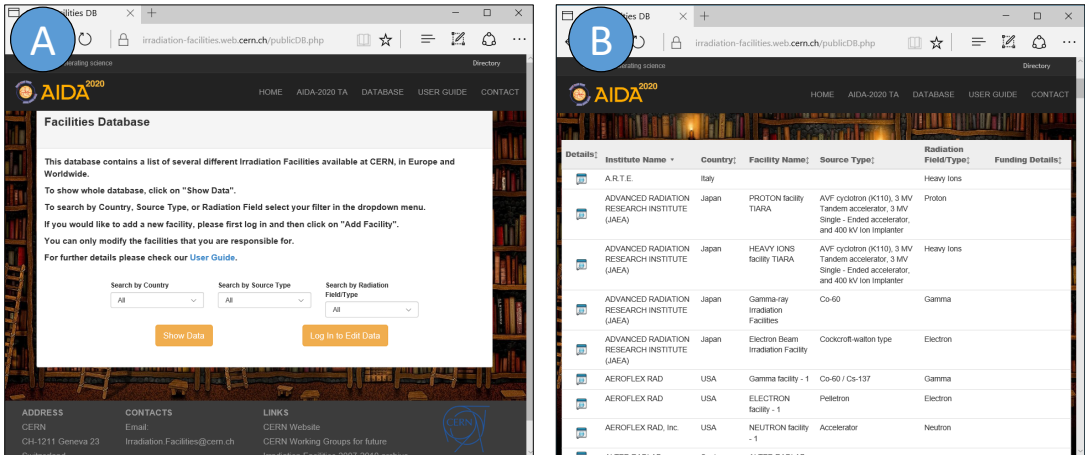


Figure A.2 – A) Subpage shown when the Irradiation Facilities Database is first loaded. B) The result of a query showing essential information about different facilities that can be sorted by each column.

MATERIALS FOR SAMPLE HOLDERS

In the last decade increasing number of samples irradiated in IRRAD targeted a total proton fluence of 10^{16} p/cm² or higher. Such a requested fluence is now further increasing due to the greater number of experiments targeting HL-LHC, and FCC developments, such as for this thesis, often exceeding the 10^{17} p/cm².

Today, the irradiation tests in IRRAD are performed by either mounting the objects on custom made supports (usually built of plastic material), or by adapting them to be compatible with the standard 5x5 cm² cardboard holders, which can then be conveniently stacked and fixed on the irradiation tables as shown in Figure B.1-A, or on the shuttle system as shown in Figure B.1-B.



Figure B.1 – A) Sample holders installed on an irradiation table. B) Sample holders installed on the IRRAD1 shuttle system. C) Current Sample Holder after high fluence irradiation

These cardboards are being used in IRRAD since 2000s as standard carriers for small samples, typically silicon PAD detector structures. At first a commercial “recycled-paper” cardboard was used, later this was replaced with a higher purity “cellulose” cardboard, which by having less impurities, reduced its activation.

The main advantages of the cardboard sample-holders are:

1. Low cost, commercially available high-purity cardboard;
2. Versatile and easily adaptable to the sample size and shape (by using a simple cutter-blade).

However, with the increasing radiation levels required by HL-LHC and FCC experiments, the cardboard holder is showing strong degradation (Figure B.1-C).

The main identified drawbacks of the cardboard sample-holders for HL-LHC and FCC

developments are:

1. Very strong deterioration after long irradiations ($>1 \times 10^{16}$ p/cm²), with loss of mechanical strength;
2. Higher risk of contamination due to cardboard embrittlement.
3. Not reusable, generating a lot of radioactive waste.
4. Higher radioactivity (due to unavoidable impurities in the cellulose).

These facts motivated the research for an new version of sample holders to be used as support of the devices and PCBs tested in this thesis, as well as for any future HL-LHC and FCC developments, in IRRAD and in other irradiation facilities.

New Sample Holders Specifications

The ideal sample holder material should not become very radioactive and its radioactivity should decay as fast as possible, in order to limit the exposure to users and operators during handling.

These characteristics are proportional to the chemical composition (higher-Z materials, are normally more radioactive), and to the overall mass (the lighter, the better). While ultra-thin sample holders should be the perfect solution, a minimum thickness is required in order to give enough mechanical strength to the support for enduring handling operations.

The combination of fast radiation decay and strong mechanical properties result in a sample holder that can be reused more than once, thus justifying a higher cost than a cheaper cardboard-based solution.

Finally the availability of the material at CERN, the possibility of easy-machining and adaptability to differently shaped detectors, as well as satisfying safety requirements in terms of flammability, are all specifications taken into account in this study for finding the best material for the next generation sample holders.

Material and Irradiation Experiments

Several materials were selected for this study. Along with the standard cardboard, different sets of carbon-based materials were tested such as plastics and fibers. The complete set of tested samples is listed in Table B.1. All irradiations were carried out in steps allowing intermediate assessments of the degradation of the material with increasing integrated particle fluence.

Material	Type	Chemical Comp.	Max n Fluence	Max p Fluence	Ref.
Cardboard	Cellulose	$C_6H_{10}O_5$	5×10^{16} n/cm ²	2×10^{16} p/cm ²	[a]
Nylon	PA 6.6, PA6	$C_{18}H_{37}N_3O_5$	5×10^{16} n/cm ²	-	[b]
3D Printed	ABSplus-P430	$(C_8H_8 \cdot C_4H_6 \cdot C_3H_3N)_n$	2×10^{17} n/cm ²	-	[c]
Carbon Fiber	CarbonVeneta, FAPS , BRT	C_3H_3N precursor	5×10^{17} n/cm ²	1.6×10^{17} p/cm ²	[d]
PEEK	Natur KundertAG	$(C_{19}H_{12}O_3)_n$	2×10^{17} n/cm ²	1.6×10^{17} p/cm ²	[e]
ULTEM	1000	$(C_{37}H_{24}O_6N_2)_n$	2×10^{17} n/cm ²	1.6×10^{17} p/cm ²	[f]

Table B.1 – Set of different material samples, with details on their chemical composition, tested with neutrons at JSI-TRIGA Nuclear Reactor and with protons at CERN-IRRAD.

[a] Carton: <https://www.klug-conservation.fr/Cartons-Musee-017-ES-blanc-nature>

[b] Nylon: <http://www.dupont.com/products-and-services/plastics-polymers-resins>

[c] 3D Printed: <https://www.stratasys.com/materials/search/absplus>

[d] Carbon Fibers: CarbonVeneta <http://www.carbonveneta.it>; FAPS <http://www.fapsteam.it>; BRT www.brtindustrialservice.com

[e] PEEK: <https://omnexus.specialchem.com/product-categories/thermoplastics-pk-polyketone-peek>

[f] ULTEM: <https://www.sabic.com/en/products/specialties/ultem-resins/ultem-resin>

Two irradiation campaigns, in 2017 and 2018, were performed in Ljubljana at the JSI TRIGA Nuclear Reactor (Figure B.2), and one irradiation in 2018, was carried out at the CERN IRRAD Proton Facility (Figure B.3).

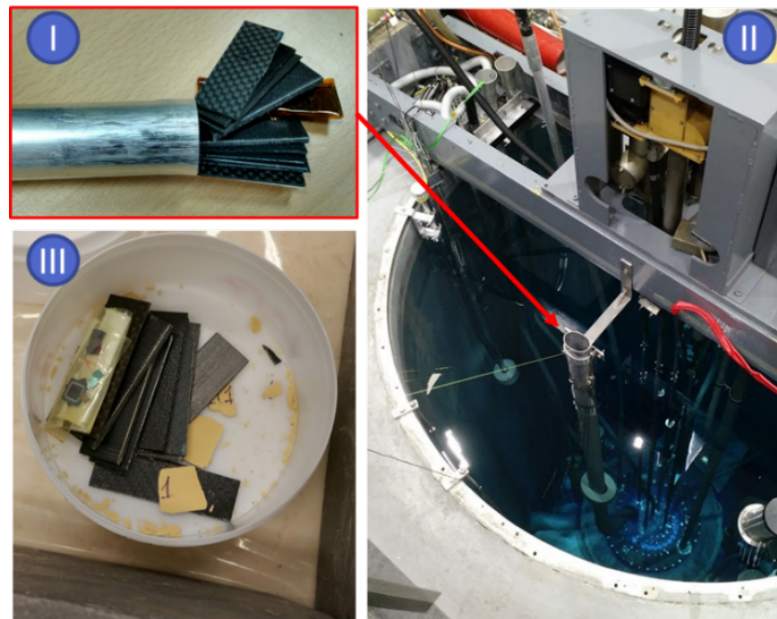


Figure B.2 – Irradiation setup at the JSI TRIGA Nuclear Reactor, with the irradiation cylinder (I), inserted in the irradiation channel (II) and the resulting irradiated materials with the powdered cardboard (III).

Appendix B. Materials for Sample Holders

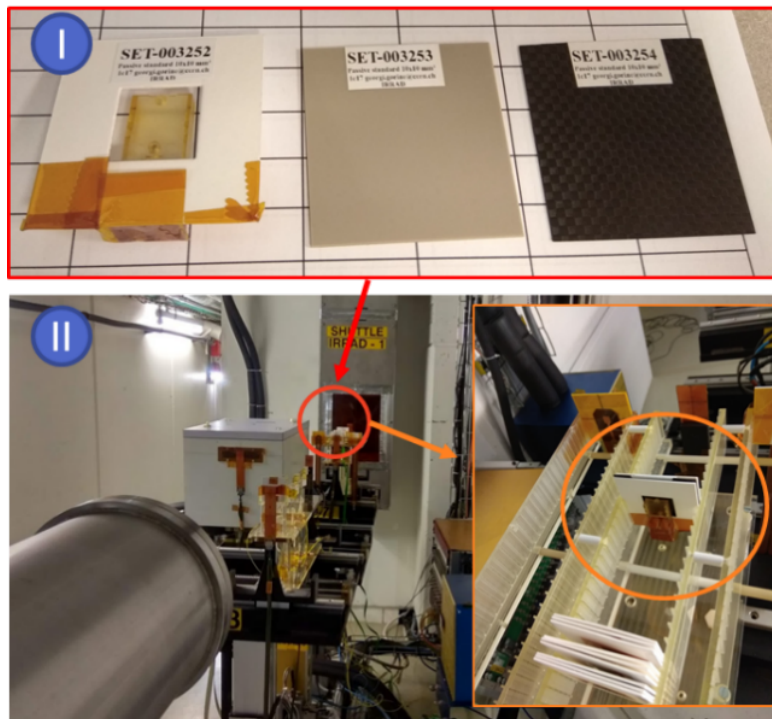


Figure B.3 – Irradiation setup at CERN IRRAD, with the samples (I) and the irradiation table (II).

During the first test in JSI, carton and nylon were excluded from further experiments due to great degradation even at lower fluence levels, while 3D-printed samples were excluded due to a very high activation. For these reasons, the irradiation steps that followed, were performed only on the Carbon fiber, PEEK, and ULTEM samples.

Measurement Description and Results

In order to qualify the different materials in terms of their radiation hardness, activation, and mechanical qualification as sample holders, three tests were performed after each irradiation step:

1. *Optical inspection:* detection of radiation-induced cracks and/or deformations, by means of optical microscope imaging (Figure B.4-A).
2. *Activation measurement:* in order to assess the level of activation, and the radioactivity decay that follows, measurements were performed using a Geiger-Muller counter (Automess 6150-AD6), at 10 cm and at contact with the material (as shown in Figure B.4-B), and repeated after one week and two weeks of cool down.
3. *Mechanical test:* by keeping the sample with two hands (or with two pliers as shown in Figure B.4-C), a stress test in “operative conditions” is performed, by bending the support as if detaching a detector or aluminium.

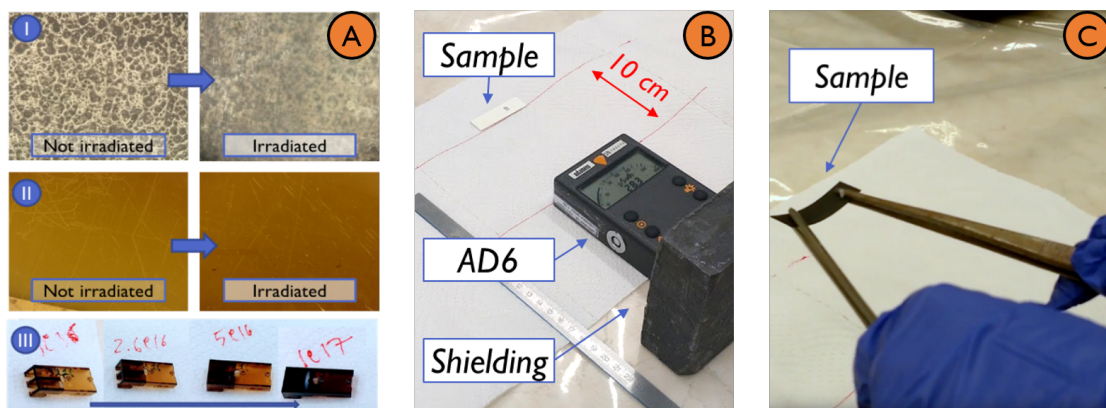


Figure B.4 – A) Optical inspection before and after irradiation of a carbon fibre (I), PEEK (II), and ULTEM (III). B) Activation measurement at 10 cm distance, C) Mechanical test.

These assessments, together with an analysis on the costs, material availability at CERN, and safety, allowed to compare the different materials and rule out the best alternatives to today's cardboard.

The main results of this study are schematized in Table B.5, justifying carbon fiber as best material in terms of decay time and reusability, and ULTEM as best in terms of initial activation levels and costs.

	Activation (after irradiation)	Decay Time (in 2 weeks)	Mechanical Strength	Machining At CERN	Fabrication Cost	Safety (*IS41)	Reusability
Cardboard	★★	★★	★	★★★★	★★★★	★	★
3D Printed	★	★★	★★★	★★★	★★★	★	★★
Nylon	★★	★★★	★★	★★★	★★★	★★	★★
Carbon Fibre	★★★	★★★★	★★★★	★★	★★	★★★	★★★★
PEEK	★★★★	★★★	★★★★	★★★	★	★★★★	★★★
ULTEM	★★★★	★★★	★★★★	★★★	★★★	★★★★	★★★
★★★★★ Best ★★★ Better ★★ Good ★ Not so good							

Figure B.5 – Comparison table between possible alternatives to cardboard as materials for future sample holders. * IS41 <https://edms.cern.ch/document/335806/1.02>

For this thesis project, carbon fiber was selected as material for supports used in the irradiations performed in IRRAD and also as support for the irradiation of the passive samples in JSI-TRIGA .

COPPER EXPANSION DURING OXIDATION

During the radiation enhanced oxidation of the copper, as the oxide thickness $t_{\text{Cu}_2\text{O}}$ grows, it consumes the copper atoms at the surface. This causes the Cu-Cu₂O interface to move while the oxide grows, with the final device thickness t_f being different from the initial thickness t_i . The equation which governs the amount of consumed copper is:

$$t_{\text{Cu}} = t_{\text{Cu}_2\text{O}} \cdot \frac{N_{\text{Cu}_2\text{O}}}{N_{\text{Cu}}} \quad (\text{C.1})$$

where $N_{\text{Cu}_2\text{O}}$ and N_{Cu} are the molecular densities of Cu₂O and Cu, respectively. Copper has an atomic weight $A_{\text{Cu}} = 63.546 \text{ g/mol}$ and an atomic density $\rho_{\text{Cu}} = 8.960 \text{ g/cm}^3$. Oxygen has an atomic weight $A_{\text{O}} = 15.999 \text{ g/mol}$ and an atomic density $\rho_{\text{O}} = 1.141 \text{ g/cm}^3$. Cu₂O has an atomic density $\rho_{\text{Cu}_2\text{O}} = 6.0 \text{ g/cm}^3$. The molecular densities of Cu and Cu₂O can be then calculated as:

$$\begin{aligned} N_{\text{Cu}} &= \frac{\rho_{\text{Cu}} \cdot N_A}{A_{\text{Cu}}} = \frac{8.96 \cdot N_A}{63.546} = 8.491 \times 10^{22} \text{ atoms/cm}^3 \\ N_{\text{Cu}_2\text{O}} &= \frac{\rho_{\text{Cu}_2\text{O}} \cdot N_A}{2 \cdot A_{\text{Cu}} + A_{\text{O}}} = \frac{6.0 \cdot N_A}{2 \cdot 63.546 + 15.999} = 2.525 \times 10^{22} \text{ molecules/cm}^3 \end{aligned} \quad (\text{C.2})$$

Finally, by following Eq. C.1 is possible to find the amount of copper consumed with respect to the oxide thickness:

$$t_{\text{Cu}} = t_{\text{Cu}_2\text{O}} \cdot \frac{N_{\text{Cu}_2\text{O}}}{N_{\text{Cu}}} = 0.297 \cdot t_{\text{Cu}_2\text{O}} \quad (\text{C.3})$$

indicating that approximately 30% of the Cu₂O is found within the original copper, while approximately 70% is new volume growing outwards into the ambient, as shown in Figure C.1. Finally is possible to express the total initial thickness t of the device as:

$$t = t_{\text{Cu}} + 0.3 t_{\text{Ox}} \quad (\text{C.4})$$

where t_{Ox} is the radiation induced growing oxide layer.

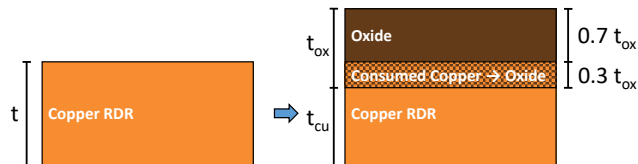


Figure C.1 – Moving interfaces and volume expansion after copper oxidation.

NON-LINEAR MODEL FOR THE RADIATION ENHANCED OXIDATION

One of the possible modifications to the linear Radiation Enhanced Oxidation model explained in Section 5.3 is to consider the two different modes of copper oxide growth. As calculated in Section 5.2, the oxide thickness t_{ox} is found to have two solutions depending on the magnitude of Φ :

$$t_{ox} = \begin{cases} \frac{B}{A}\Phi, & \text{for small } \Phi. \\ \sqrt{B\Phi}, & \text{for large } \Phi. \end{cases} \quad (D.1)$$

with $A = 2D_{ox}/k_i$ and $B = 2D_{ox}C_s/C_{tot}$.

For the simpler model (as done in Section 5.3), only the linear expression of oxide growth was considered in Eq.5.14 obtaining:

$$R(\Phi) = R_0 \left(1 + \underbrace{\frac{0.3}{t} \frac{B}{A}}_{\beta_1} \Phi \right) = R_0 (1 + \beta_1 \Phi) \quad (D.2)$$

with $\beta_1 = \frac{0.3}{t} \frac{B}{A}$ which is the *linear* radiation enhanced oxidation coefficient.

A refinement of the Radiation Enhanced Oxidation model is to consider also the square-root function of t_{ox} and substituting again in Eq.5.14, $R(\Phi)$ becomes:

$$R(\Phi) = R_0 \left(1 + \underbrace{\frac{0.3}{t} \sqrt{B}}_{\beta_2} \sqrt{\Phi} \right) = R_0 (1 + \beta_2 \sqrt{\Phi}) \quad (D.3)$$

with $\beta_2 = \frac{0.3}{t} \sqrt{B}$ being the *square-root* radiation enhanced oxidation coefficient.

Figure D.1 shows the linear fit and the square-root fits. The first obtained calibrating β_1 for small Φ in the interval from 1×10^{16} to 2×10^{16} (blue data points), and the second obtained calibrating β_2 for large Φ from 4×10^{16} to 5×10^{16} (red data points). All the coefficients that were found are listed in Table D.1.

Appendix D. Non-linear Model for the Radiation Enhanced Oxidation

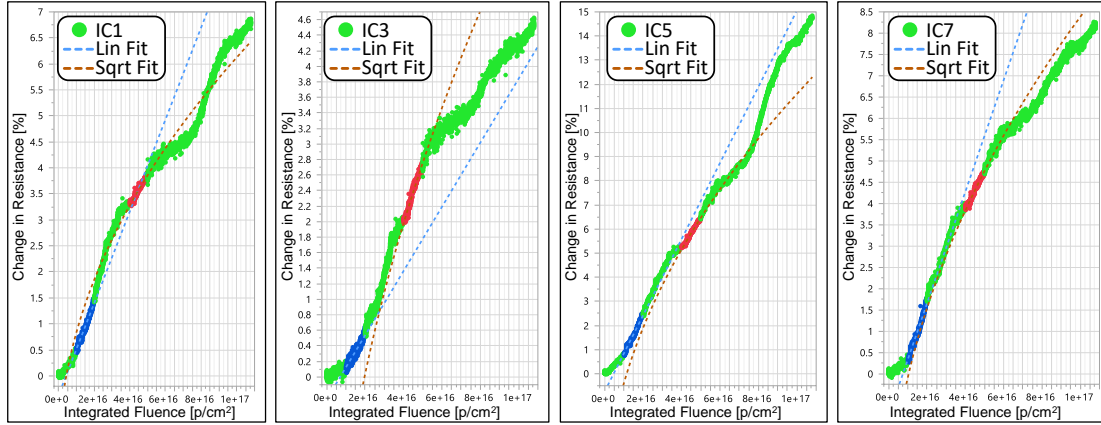


Figure D.1 – Extraction of the radiation enhanced oxidation coefficients β_1 by considering a linear fit of the initial subset (in blue), and β_2 by considering a square-root fit of the middle subset (in red), of the normalized resistance variation $100 \times \frac{R(T,\Phi) - R_T}{R_T}$ with increasing particle fluence.

	Tag	R_0 [Ω]	α [$1/^\circ\text{C}$]	β_1 [cm^2/p]	β_2 [$\text{cm}/\sqrt{\text{p}}$]
PCB1	IC1	73.36	0.00391	8.59×10^{-17}	2.45×10^{-8}
	IC3	59.28	0.00377	3.49×10^{-17}	3.31×10^{-8}
PCB2	IC5	139.93	0.00379	1.48×10^{-16}	5.56×10^{-8}
	IC7	77.41	0.00361	1.12×10^{-16}	3.92×10^{-8}

Table D.1 – Extracted temperature coefficients α and the radiation coefficients β_1 and β_2 for the different non passivated Cu RDRs irradiated in IRRAD2 and described in Section 4.5.

As can be seen in Figure D.1, while combining the two laws would provide a more accurate prediction especially for higher levels of Φ , the calibration of β_2 cannot be performed simply extrapolated at the beginning of an irradiation. This precludes the usage of this refined model since in practice the RDR calibration is possible only for low levels of Φ when the calibrating device is still operating.

On the other hand, β_2 could be extrapolated from β_1 , but this would require to have a precise knowledge of the oxidation coefficients D_{ox} and k_i (included in A and B in Eq. D.1). Unfortunately such values are not known for sub-micrometer thin films of copper as the ones used for the RDRs. Therefore, before refining the Radiation Enhanced Radiation model by including the square-root function of t_{ox} , additional experimental data has to be collected to deeper study the oxidation process and experimentally define the A and B coefficients in Eq. D.1.

RDR PROCESS FLOW






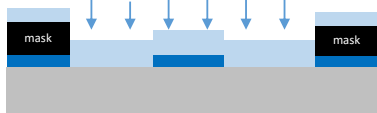
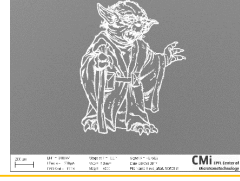

Step	Process description	Cross-section after process
1	Double PR coating for Lift Off Machine: ACS200 Gen3 PR: 0.82 μm LOR 5A + 1.5 μm AZ 1512 HS	
2	PR Exposure with Mask Machine: MA6Gen3 Dose : 68 mJ/cm ² (i-line)	
3	Photoresist development Machine: ACS200	
4	Metal Sputtering Machine: DP650 Metal :10 nm Ti+ 500 nm Cu	
5	Lift-Off Wet Bench: Microposit 1165	
6	Shadow Mask Alignment 385 μm thick shadow mask, aligned and fixed with Kapton using optical microscope	
7	Passivation Layer Sputtering Machine: Spider 600 Oxide : 200 nm SiO ₂	
8	Inspection Machine: SEM Zeiss MERLIN	
9	Wafer Dicing Machine: Disco DAD321	
10	Chip Wire Bonding Machine: TPT HB10	

Figure E.1 – Process flow for 500 nm thick Cu-RDRs with and without SiO₂ passivation.

Bibliography

- [1] P. W. Higgs, “Broken symmetries and the masses of gauge bosons,” *Physical Review Letters*, vol. 13, pp. 508–509, 10 1964. [DOI]: 10.1103/PhysRevLett.13.508.
- [2] The CEPC Study Group, “CEPC Conceptual Design Report,” *arXiv.org*, 2018. [URL]: <https://arxiv.org/abs/1811.10545v1>
- [3] “Fcc physics opportunities,” *The European Physical Journal C*, vol. 79, no. 6, p. 474, 6 2019. [DOI]: 10.1140/epjc/s10052-019-6904-3.
- [4] M. I. Besana, M. Capeans, F. Cerutti, S. Danzeca, F. Faccio, G. Gorine, A. Infantino, M. Moll, F. Ravotti, and J. M. Sallese, “Fcc-hh: The hadron collider,” *The European Physical Journal Special Topics*, vol. 228, no. 4, pp. 755–1107, 8 2019. [DOI]: 10.1140/epjst/e2019-900087-0.
- [5] W. Herr and B. Muratori, “Concept of luminosity,” *CAS - CERN Accelerator School: Intermediate Course on Accelerator Physics, Zeuthen, Germany*, vol. 2, no. 3, pp. 361–378, 2003. [DOI]: 10.5170/CERN-2006-002.361.
- [6] G. E. Knoll and J. Wiley, *Radiation Detection and Measurement Third Edition*. John Wiley & Sons, 2000. ISBN 0471073385. [URL]: <http://www.slac.stanford.edu/spires/find/books/www?cl=QCD915:K55:2000>
- [7] G. Choppin, J.-O. Liljenzin, and J. Rydberg, *Radiochemistry and Nuclear Chemistry*. ELSEVIER, 2001. ISBN 9780750674638. [URL]: <https://www.elsevier.com/books/radiochemistry-and-nuclear-chemistry/choppin/978-0-7506-7463-8>
- [8] A. Infantino, R. G. Alía, M. I. Besana, M. Brugger, and F. Cerutti, “Preliminary design of CERN Future Circular Collider tunnel: first evaluation of the radiation environment in critical areas for electronics,” in *ICRS13*, Paris, France, 2016. [DOI]: 10.1051/epjconf/201715303004.
- [9] M. I. Besana, F. Cerutti, A. Ferrari, W. Riegler, and V. Vlachoudis, “Evaluation of the radiation field in the future circular collider detector,” *Physical Review Accelerators and Beams*, vol. 19, no. 11, p. 111004, 2016. [DOI]: 10.1103/PhysRevAccelBeams.19.111004.
- [10] D. Taylor and J. Sharpe, “Nuclear particle and radiation detectors. Part 1: Ion chambers and ion-chamber instruments,” *Proceedings of the IEE - Part II: Power Engineering*, 1951. [DOI]: 10.1049/pi-2.1951.0058.

Bibliography

- [11] C. G. Soares, "Radiochromic film dosimetry," *Radiation Measurements*, 2006. [DOI]: 10.1016/j.radmeas.2007.01.007.
- [12] B. J. Mincher and M. K. Zaidi, "Calibration of Far West Technology (FWT-60) Radiochromic Dye Dosimeters," *Radiation Protection Dosimetry*, 1993. [DOI]: 10.1093/rpd/47.1-4.571.
- [13] L. Karsch, E. Beyreuther, T. Burris-Mog, S. Kraft, C. Richter, K. Zeil, and J. Pawelke, "Dose rate dependence for different dosimeters and detectors: TLD, OSL, EBT films, and diamond detectors," *Medical Physics*, 2012. [DOI]: 10.1118/1.3700400.
- [14] A. S. Beddar, T. R. Mackie, and F. H. Attix, "Water-equivalent plastic scintillation detectors for high-energy beam dosimetry: I. Physical characteristics and theoretical considerations," *Physics in Medicine and Biology*, 1992. [DOI]: 10.1088/0031-9155/37/10/006.
- [15] S. Liao, R. Erasmus, H. Jivan, C. Pelwan, G. Peters, and E. Sideras-Haddad, "A comparative study of the radiation hardness of plastic scintillators for the upgrade of the Tile Calorimeter of the ATLAS detector," in *Journal of Physics: Conference Series*, 2015. [DOI]: 10.1088/1742-6596/645/1/012021. . ISSN 1742-6596
- [16] M. F. Desrosiers, A. M. Forney, and J. M. Puhl, "A comparison of Harwell & FWT alanine temperature coefficients from 25 °C to 80 °C," *Journal of Research of the National Institute of Standards and Technology*, 2012. [DOI]: 10.6028/jres.117.007.
- [17] A. Mainwood, "Recent developments of diamond detectors for particles and UV radiation," *Semiconductor Science and Technology*, 2000. [DOI]: 10.1088/0268-1242/15/9/201.
- [18] C. E. DeAlmeida, R. Ochoa, M. C. De Lima, M. G. David, E. J. Pires, J. G. Peixoto, C. Salata, and M. A. Bernal, "A feasibility study of Fricke Dosimetry as an absorbed dose to water standard for ¹⁹²Ir HDR sources," *PLoS ONE*, 2014. [DOI]: 10.1371/journal.pone.
- [19] F. Ravotti, M. Glaser, and M. Moll, "'SENSOR CATALOGUE" Data compilation of solid-state sensors for radiation monitoring," *Cern Edms*, vol. TS-Note-20, 2005. [URL]: <https://edms.cern.ch/document/590497/1>
- [20] NASA, "Nuclear and space radiation effects on materials, NASA Space Vehicle Design Criteria- (Structures)," *NASA space vehicle design criteria*, no. June, p. 44, 1970. [URL]: <https://ntrs.nasa.gov/archive/nasa/casi.ntrs.nasa.gov/19710015558.pdf>
- [21] L. K. Mansur, "Theory and experimental background on dimensional changes in irradiated alloys," *Journal of Nuclear Materials*, vol. 216, no. C, pp. 97–123, 1994. [DOI]: 10.1016/0022-3115(94)90009-4.
- [22] R. L. Chaplin and R. R. Coltman, "Defects and transmutations in reactor-irradiated copper," *Journal of Nuclear Materials*, vol. 108-109, no. C, pp. 175–182, 1982. [DOI]: 10.1016/0022-3115(82)90485-8.

- [23] J. A. Brinkman, "On the nature of radiation damage in metals," *Journal of Applied Physics*, vol. 25, no. 8, pp. 961–970, 1954. [DOI]: 10.1063/1.1721810.
- [24] J. Brinkman, "Production of Atomic Displacements by High-Energy Particles," *American Journal of Physics*, vol. 24, no. 4, pp. 246–267, 1956. [DOI]: 10.1119/1.1934201.
- [25] S. J. Zinkle, *Radiation-induced effects on microstructure*. Elsevier Inc., 2012, vol. 1. ISBN 9780080560335. [URL]: <https://doi.org/10.1016/B978-0-08-056033-5.00003-3>
- [26] M. Kangilaski, "The effects of neutron radiation on structural materials," NASA, Tech. Rep., 1967. [URL]: <https://ntrs.nasa.gov/search.jsp?R=19680007407>
- [27] A. Y. Dunn, "Radiation damage accumulation and associated mechanical hardening in thin films and bulk materials," Ph.D. dissertation, 2016. [URL]: <https://smartech.gatech.edu/handle/1853/54959>
- [28] J. W. Martin, "The electrical resistivity of some lattice defects in FCC metals observed in radiation damage experiments," *Journal of Physics F*, vol. 2, no. 5, p. 842, 1972. [DOI]: 10.1088/0305-4608/2/5/008.
- [29] S. J. Zinkle, "Electrical resistivity of small dislocation loops in irradiated copper," *Journal of Physics F: Metal Physics*, vol. 18, p. 377, 1988. [DOI]: 10.1088/0305-4608/18/3/009.
- [30] M. M. Ramsay, "The effect of neutron irradiation on thin film resistors," *Trans. Metall. Soc. AIME*, vol. 239, pp. 917–919, 1967. [DOI]: 10.1016/0040-6090(68)90069-2.
- [31] J. Shewchun, W. R. Hardy, D. Kuenzig, and C. Tam, "Reactively sputtered tantalum thin film resistors part 2. low energy, low fluence proton radiation damage," *Thin Solid Films*, vol. 8, no. 2, pp. 101–115, 1971. [DOI]: 10.1016/0040-6090(71)90002-2.
- [32] J. F. Ziegler, M. D. Ziegler, and J. P. Biersack, "SRIM – The Stopping and Range of Ions in Matter (2010)," *Nucl. Instr. Meth. B*, vol. 268, pp. 1818–1823, 2010. [URL]: <http://dtic.mil/dtic/tr/fulltext/u2/a515302.pdf>
- [33] A. Ferrari, P. R. Sala, A. Fasso, and J. Ranft, "FLUKA: a multi-particle transport code," *CERN Yellow Reports: Monographs*, no. CERN-2005-10, 2005. [DOI]: 10.5170/CERN-2005-010.
- [34] T. T. Böhlen, F. Cerutti, M. P. W. Chin, A. Fassò, A. Ferrari, P. G. Ortega, A. Mairani, P. R. Sala, G. Smirnov, and V. Vlachoudis, "The FLUKA Code: Developments and challenges for high energy and medical applications," *Nuclear Data Sheets*, vol. 120, pp. 211–214, 2014. [DOI]: 10.1016/j.nds.2014.07.049.
- [35] A. Fasso, A. Ferrari, G. Smirnov, F. Sommerer, and V. Vlachoudis, "FLUKA Realistic Modeling of Radiation Induced Damage," *Progress in Nuclear Science and Technology*, vol. 2, pp. 769–775, 2011. [URL]: <http://www.aesj.or.jp/publication/pnst002/data/769-775.pdf>

- [36] M. Guthoff, W. De Boer, and S. Müller, “Simulation of beam induced lattice defects of diamond detectors using FLUKA,” *Nuclear Instruments and Methods in Physics Research, Section A: Accelerators, Spectrometers, Detectors and Associated Equipment*, vol. 735, pp. 223–228, 2014. [DOI]: 10.1016/j.nima.2013.08.083.
- [37] R. Froeschl, M. Brugger, and S. Roesler, “The CERN High Energy Accelerator Mixed Field (CHARM) Facility in the CERN PS East Experimental Area,” in *Proceedings, 12th Meeting of Task-Force on Shielding Aspects of Accelerators, Targets and Irradiation Facilities (SATIF-12): Batavia, IL, USA, April 28-30, 2014*, 2015, pp. 14–25. [URL]: http://old.inspirehep.net/record/1479509/files/1479081_14-25.pdf
- [38] L. Snoj, G. Žerovnik, and A. Trkov, “Computational analysis of irradiation facilities at the JSI TRIGA reactor,” *Applied Radiation and Isotopes*, vol. 70, no. 3, pp. 483–488, 2012. [DOI]: 10.1016/j.apradiso.2011.11.042.
- [39] B. Gkotse, M. Brugger, P. Carbonez, S. Danzeca, A. Fabich, R. G. Alia, M. Glaser, G. Gorine, M. R. Jaekel, I. M. Suau, G. Pezzullo, F. Pozzi, F. Ravotti, M. Silari, and M. Tali, “Irradiation facilities at cern,” in *2017 17th European Conference on Radiation and Its Effects on Components and Systems (RADECS)*, 2017. [DOI]: 10.1109/RADECS.2017.8696163.
- [40] J. Bronuzzi, B. Gkotse, M. Glaser, G. Gorine, I. Mateu, and G. Pezzullo, “Radiation-hard instrumentation for the CERN Proton Facility,” 2 2019. [URL]: <https://cds.cern.ch/record/2663195>
- [41] A. G. Holmes-Siedle and L. Adams, *Handbook of Radiation Effects*. Oxford: Oxford Univ. Press, 2002. ISBN 978-0198507338. [URL]: <https://cds.cern.ch/record/579299/>
- [42] B. Gkotse, M. Glaser, P. Jouvelot, E. Matli, G. Pezzullo, and F. Ravotti, “Towards a unified environmental monitoring, control and data management system for irradiation facilities: the cern irrad use case,” in *2017 17th European Conference on Radiation and Its Effects on Components and Systems (RADECS)*, 2017. [DOI]: 10.1109/RADECS.2017.8696209.
- [43] F. Pozzi, R. G. Alia, M. Brugger, P. Carbonez, S. Danzeca, B. Gkotse, M. R. Jaekel, F. Ravotti, M. Silari, and M. Tali, “CERN Irradiation Facilities,” *Radiation Protection Dosimetry*, vol. 180, no. 1-4, pp. 120–124, 09 2017. [DOI]: 10.1093/rpd/ncx187.
- [44] G. Gorine and B. Gkotse, “Irradiation Facilities Database Website,” 2016. [URL]: <https://www.cern.ch/irradiation-facilities>
- [45] M. Glaser, M. Moll, and F. Ravotti, “Installation of new equipment: Movable irradiation tables operational,” *AIDA2020*, 8 2013. [URL]: <https://cds.cern.ch/record/1594787>
- [46] C. Kurfürst, B. Dehning, M. Sapinski, M. R. Bartosik, T. Eisel, C. Fabjan, C. A. Rementeria, E. Griesmayer, V. Eremin, E. Verbitskaya, A. Zabrodskii, N. Fadeeva, Y. Tuboltsev, I. Eremin, N. Egorov, J. Härkönen, P. Luukka, and E. Tuominen, “In situ radiation test of silicon and diamond detectors operating in superfluid helium and developed for beam loss

- monitoring,” *Nuclear Instruments and Methods in Physics Research Section A: Accelerators, Spectrometers, Detectors and Associated Equipment*, vol. 782, pp. 149–158, 2015. [DOI]: 10.1016/j.nima.2015.02.002.
- [47] K. Ambrožič, G. Žerovnik, and L. Snoj, “Computational analysis of the dose rates at JSI TRIGA reactor irradiation facilities,” *Applied Radiation and Isotopes*, vol. 130, no. August, pp. 140–152, 2017. [DOI]: 10.1016/j.apradiso.2017.09.022.
- [48] “Advanced European Infrastructures for Detectors at Accelerators - AIDA2020,” 2019. [URL]: <http://aida2020.web.cern.ch>
- [49] L. Snoj and B. Smodiš, “45 Years of TRIGA Mark II in Slovenia,” in *Proceedings of the International Conference Nuclear Energy for New Europe 2011*, Bovec, Slovenia, 2011, p. 401. [URL]: <http://www.nss.si/proc/nene2011/pdf/401.pdf>
- [50] N. V. Mokhov and I. L. Rakhno, “Protecting lhc components against radiation resulting from colliding beam interactions,” 6 2001. [URL]: <http://cds.cern.ch/record/527220>
- [51] E. Hoyer, W. Turner, and W. Elliot, “LHC IP1 / IP5 NEUTRAL BEAM ABSORBERS (TAN),” CERN, Tech. Rep., 2002. [URL]: <https://edms.cern.ch/document/108093/2.2>
- [52] H. S. Matis, M. Placidi, A. Ratti, W. C. Turner, E. Bravin, and R. Miyamoto, “The BRAN luminosity detectors for the LHC,” *Nuclear Instruments and Methods in Physics Research, Section A: Accelerators, Spectrometers, Detectors and Associated Equipment*, vol. 848, no. 4, pp. 114–126, 2017. [DOI]: 10.1016/j.nima.2016.12.019.
- [53] A. Ratti, J. F. Beche, J. Byrd, K. Chow, P. Denes, L. Doolittle, W. Ghiorso, P. F. Manfredi, H. Matis, M. Monroy, D. Plate, T. Stezelberger, J. Stiller, B. Turko, W. C. Turner, H. Yaver, S. Zimmermann, E. Braving, A. Drees, and R. Miyamoto, “The luminosity monitoring system for the lhc: Modeling and test results,” in *2009 IEEE Nuclear Science Symposium Conference Record (NSS/MIC)*, 10 2009. [DOI]: 10.1109/NSSMIC.2009.5401747. pp. 286–289.
- [54] “Doosan Corporation Electro-Materials,” 2019. [URL]: <http://www.doosanelectronics.com/en/halogen-free-substrate-materials/fr-4-ds-7402/>
- [55] F. Ravotti, M. Glaser, M. Moll, K. Idri, J. R. Vaillé, H. Prevost, and L. Dusseau, “Conception of an integrated sensor for the radiation monitoring of the CMS experiment at the large hadron collider,” *IEEE Transactions on Nuclear Science*, vol. 51, no. 6 II, pp. 3642–3648, 2004. [DOI]: 10.1109/TNS.2004.839265.
- [56] F. Ravotti, M. Glaser, A. B. Rosenfeld, M. L. F. Lerch, A. G. Holmes-Siedle, and G. Sarabayrouse, “Radiation monitoring in mixed environments at CERN: From the IRRAD6 facility to the LHC experiments,” *IEEE Transactions on Nuclear Science*, vol. 54, no. 4, pp. 1170–1177, 2007. [DOI]: 10.1109/TNS.2007.892677.

Bibliography

- [57] G. Gorine, G. Pezzullo, I. Mandic, A. Jazbec, L. Snoj, M. Capeans, M. Moll, D. Bouvet, F. Ravotti, and J. M. Sallese, "Ultra high fluence radiation monitoring technology for the future circular collider at cern," *IEEE Transactions on Nuclear Science*, vol. 65, no. 8, pp. 1583–1590, aug 2018. [DOI]: 10.1109/tns.2018.2797540.
- [58] M. R. Pinnel, H. G. Tompkins, and D. E. Heath, "Oxidation of copper in controlled clean air and standard laboratory air at 50°C to 150°C," *Applications of Surface Science*, vol. 2, no. 4, pp. 558–577, 1979. [DOI]: 10.1016/0378-5963(79)90047-3.
- [59] M. J. Berger, J. S. Coursey, and M. A. Zucker, "Stopping-power and range tables for electrons, protons, and helium ions." [URL]: <http://dx.doi.org/10.18434/T4NC7P>
- [60] G. Gorine, G. Pezzullo, D. Bouvet, F. Ravotti, and J. M. Sallese, "Radiation enhanced oxidation of proton-irradiated copper thin-films: Towards a new concept of ultra-high radiation dosimetry," *AIP Advances*, vol. 9, no. 8, p. 085217, 2019. [DOI]: 10.1063/1.5096606.
- [61] Z. Han, L. Lu, H. W. Zhang, Z. Q. Yang, F. H. Wang, and K. Lu, "Comparison of the oxidation behavior of nanocrystalline and coarse-grain copper," *Oxidation of Metals*, vol. 63, no. 5-6, pp. 261–275, 2005. [DOI]: 10.1007/s11085-005-4381-6.
- [62] S. Samal, *High [U+2010] Temperature Oxidation of Metals*, Z. Ahmad, Ed. Rijeka: IntechOpen, 2016. [URL]: <https://doi.org/10.5772/63000>
- [63] C. J. Love, J. D. Smith, Y. Cui, and K. K. Varanasi, "Size-dependent thermal oxidation of copper: Single-step synthesis of hierarchical nanostructures," *Nanoscale*, vol. 3, no. 12, pp. 4972–4976, 2011. [DOI]: 10.1039/c1nr10993f.
- [64] P. K. Krishnamoorthy and S. C. Sircar, "Formation of very thin oxide films on copper: Kinetics and mechanism," *Oxidation of Metals*, vol. 2, no. 4, pp. 349–360, 1970. [DOI]: 10.1007/BF00604475.
- [65] Y. Zhu, K. Mimura, and M. Isshiki, "Oxidation mechanism of Cu₂O to CuO at 600-1050 °C," *Oxidation of Metals*, vol. 62, no. 3-4, pp. 207–222, 2004. [DOI]: 10.1007/s11085-004-7808-6.
- [66] C. Gattinoni and A. Michaelides, "Atomistic details of oxide surfaces and surface oxidation: the example of copper and its oxides," *Surface Science Reports*, vol. 70, no. 3, pp. 424–447, 2015. [DOI]: 10.1016/j.surfrep.2015.07.001.
- [67] S. Choudhary, J. V. N. Sarma, S. Pande, S. Ababou-Girard, P. Turban, B. Lepine, and S. Gangopadhyay, "Oxidation mechanism of thin Cu films: A gateway towards the formation of single oxide phase," *AIP Advances*, vol. 8, no. 5, 2018. [DOI]: 10.1063/1.5028407.
- [68] S. Le Caër, "Water Radiolysis: Influence of Oxide Surfaces on H₂ Production under Ionizing Radiation," *Water*, vol. 3, no. 1, pp. 235–253, 2 2011. [DOI]: 10.3390/w3010235.

-
- [69] T. Björkbacka, S. Hosseinpour, M. Johnson, C. Leygraf, and M. Jonsson, "Radiation induced corrosion of copper for spent nuclear fuel storage," *Radiation Physics and Chemistry*, vol. 92, pp. 80–86, 2013. [DOI]: 10.1016/j.radphyschem.2013.06.033.
- [70] B. Ibrahim, D. Zagidulin, M. Behazin, S. Ramamurthy, J. C. Wren, and D. W. Shoesmith, "The corrosion of copper in irradiated and unirradiated humid air," *Corrosion Science*, vol. 141, no. April, pp. 53–62, 2018. [DOI]: 10.1016/j.corsci.2018.05.024.
- [71] B. E. Deal and A. S. Grove, "General Relationship for the Thermal Oxidation of Silicon," *Journal of Applied Physics*, vol. 36, no. 12, pp. 3770–3778, dec 1965. [DOI]: 10.1063/1.1713945.
- [72] L. De Los Santos Valladares, D. H. Salinas, A. B. Dominguez, D. A. Najarro, S. I. Khondaker, T. Mitrelias, C. H. W. Barnes, J. A. Aguiar, and Y. Majima, "Crystallization and electrical resistivity of Cu₂O and CuO obtained by thermal oxidation of Cu thin films on SiO₂/Si substrates," *Thin Solid Films*, vol. 520, no. 20, pp. 6368–6374, 2012. [DOI]: 10.1016/j.tsf.2012.06.043.
- [73] Z. Feng, C. R. Marks, and A. Barkatt, "Oxidation-Rate Excursions During the Oxidation of Copper in Gaseous Environments at Moderate Temperatures," *Oxidation of Metals*, vol. 60, no. 5, pp. 393–408, 2003. [DOI]: 10.1109/IEMBS.2006.260048.

Glossary

Abbreviations

AFM	Atomic Force Microscopy
AIDA	Advanced European Infrastructures for Detectors and Accelerators
ATLAS	A Toroidal LHC Apparatus Detector
BPM	Beam Profile Monitor
BRAN	Beam Rate of Neutrals
CC60	Calibration Co-60 Gamma Irradiation Facility at CERN
CCC	CERN Control Center
CDR	Conceptual Design Report
CERN	The European Organization for Nuclear Research
CHARM	Mixed-field Irradiation Facility in CERN
COTS	Component of-The-Shelf
CPPM	Centre De Physiques Des Particules De Marseille
DAQ	Data Acquisition System
DD	Displacement Damage
EM	Electro Magnetic
EN	Engineering Department
EPFL	École Polytechnique Fédérale De Lausanne
EPFL-CMi	Center of Micronanotechnology at EPFL
FCC	Future Circular Collider
FCC-hh	Future Proton-Proton Collider
FIB	Focused Ion Beam
FLUKA	Monte Carlo Simulator
FRICKE	Chemical Dosimeter
GIF	Gamma Irradiation Facility at CERN
GPIB	General Purpose Interface Bus
GUI	Graphical User Interface
HEH	High Energy Hadron
HEP	High Energy Physics
HL-LHC	High Luminosity LHC
HSE	Health & Safety And Environmental Protection Unit
HW	Hardware

IC	Integrated Circuit
IEL	Ionizing Energy Loss
IP	Interaction Point
IRRAD	Proton Irradiation Facility at CERN
JSI	Jožef Stefan Institute in Ljubljana (Slovenia).
LabVIEW	Software Package
LBSD	Long Base Silicon Diode used in the RADMON system
LHC	Large Hadron Collider
LHC RADMON	RADMON developed for the LHC tunnel
MME	CERN Mechanical And Materials Engineering Group
MOSFET	Metal-Oxide-Semiconductor Field-Effect Transistor
MySQL	Software Package
NIEL	Non-Ionizing Energy Loss
NTC	Negative Temperature Coefficient
OSL	Optically Stimulated Luminescence Dosimeter
PCB	Printed Circuit Board
PEEK	Poliitere Etere Chetone Poliamid
PH RADMON	RADMON developed for the LHC experiments
RadFET	Radiation Metal-Oxide Field Effect Transistor
RADMON	RADIation MONitoring System
RDR	Radiation Dependent Resistor
REM	Ph-Radmon Device For LHC Experiments
RP	Radiation Protection
SEE	Secondary Electronemission
SEM	Scanning Electron Microscope
SESI	Secondary Electron Secondary Ion Detector
SEU	Single Event Upset
SI	Systems of Units
SMU	Source Meter Unit
SRIM	Stopping and Range of Ions in Matter Simulator
SSD	Solid State Detectors
STI	CERN Sources, Targets and Interactions Group
SW	Software
TAN	Target Absorber For Neutrals in LHC
TID	Total Ionizing Dose
TLD	Thermoluminescent Dosimeter
TRIGA	Triga Mark II Nuclear Reactor
ULTEM	Resin
VESPER	Irradiation Facility in CERN

Chemical Symbols

^{137}Cs	Cesium 137
^{60}Co	Cobalt 60
Al	Aluminum
bcc	Body-Centered Cubic
Cl	Chlorine
Cr	Chromium
Cu	Copper
Cu_2O	Cupric Oxide
CuO	Cuprous Oxide
fcc	Face-Centered Cubic
H	Hydrogen
H_2O_2	Hydrogen Peroxide
He	Helium
LHe	Liquid Helium
O_2	Oxygen
OH^-	Hydroxide
SiO_2	Silicon Dioxide
Ti	Titanium

Units and Constants

α	Temperature Coefficient
β	Radiation Enhanced Oxidation Coefficient
C_i	Oxidants Concentration at the Interface
C_{tot}	Total Number of Oxidants
C_s	Oxidants Concentration at the Surface
D	Dose
D_{ox}	Oxidants Diffusivity
dE	The Meanenergy Transferred By A Charged Particle
DPA	Displacements Per Atom
ev	Electronvolt
Gy	Gray
k_i	Oxidation Reaction Coefficient
Kerma	Kinetic Energy Per Unit of Mass
L	Length
m	Meter
Ω	Resistance
Φ	Particle Fluence

ϕ	Particle Flux
RH	Relative Humidity
ρ_{cu}	Copper Resistivity
ρ_{ox}	Oxide Resistivity
t_{Cu}	Copper Thickness
t_{ox}	Oxide Thickness
W	Width

List of publications

- [1] **G. Gorine**, G. Pezzullo, D. Bouvet, F. Ravotti, and J.-M. Sallese, "Radiation enhanced oxidation of proton-irradiated copper thin-films: Towards a new concept of ultra-high radiation dosimetry," *AIP Advances*, vol. 9, no. 8, p. 085217, 2019. [Online]. DOI: 10.1063/1.5096606
- [2] **G. Gorine**, G. Pezzullo, M. Moll, M. Capeans, K. Väyrynen, M. Ritala, D. Bouvet, F. Ravotti, and J.-M. Sallese, "Metal Thin-Film Dosimetry Technology for the Ultra-High Particle Fluence Environment of the Future Circular Collider at CERN," *RAD Association Journal*, vol. 3, no. 3, pp. 172–177, 2019. [Online]. DOI: 10.21175/RadJ.2018.03.029
- [3] **G. Gorine**, G. Pezzullo, I. Mandic, A. Jazbec, L. Snoj, M. Capeans, M. Moll, D. Bouvet, F. Ravotti, and J. M. Sallese, "Ultrahigh Fluence Radiation Monitoring Technology for the Future Circular Collider at CERN," *IEEE Transactions on Nuclear Science*, vol. 65, no. 8, pp. 1583–1590, 2018. [Online]. DOI: 10.1109/TNS.2018.2797540
- [4] **G. Gorine**, F. Ravotti, G. Pezzullo, M. Capeans, M. Moll, and J.-M. Sallese, "Radiation Monitoring Technologies and Irradiation Test Facilities for FCC," in *FCC Week 2017*, (Berlin), 2017.
- [5] J. Bronuzzi, B. Gkotse, M. Glaser, **G. Gorine**, I. Mateu, and G. Pezzullo, "Radiation-hard instrumentation for the CERN Proton Facility," Feb 2019. [Online]. Available: <https://cds.cern.ch/record/2663195>
- [6] G. Quero, P. Vaiano, F. Fienga, M. Giaquinto, V. D. Meo, **G. Gorine**, P. Casolaro, L. Campajola, G. Breglio, A. Crescitelli, E. Esposito, A. Ricciardi, A. Cutolo, F. Ravotti, S. Buontempo, M. Consales, and A. Cusano, "A novel lab-on-fiber radiation dosimeter for ultra-high dose monitoring," *Scientific Reports*, vol. 8, dec 2018. [Online]. DOI: 10.1038/s41598-018-35581-3
- [7] I. Mateu, M. Glaser, **G. Gorine**, M. Moll, G. Pezzullo, and F. Ravotti, "Readmon: a portable readout system for the cern PH-RADMON sensors," *IEEE Transactions on Nuclear Science*, 2017. [Online]. DOI: 10.1109/TNS.2017.2784684

- [8] D. Pfeiffer, **G. Gorine**, H. Reithler, B. Biskup, A. Day, A. Fabich, J. Germa, R. Guida, M. Jaekel, and F. Ravotti, "The radiation field in the gamma irradiation facility GIF++ at CERN," *Nuclear Instruments and Methods in Physics Research, Section A: Accelerators, Spectrometers, Detectors and Associated Equipment*, vol. 866, pp. 91–103, 2017. [Online]. DOI: 10.1016/j.nima.2017.05.045
- [9] B. Gkotse, M. Brugger, P. Carbonez, S. Danzeca, A. Fabich, R. Garcia, M. Glaser, **G. Gorine**, M. R. Jaekel, I. M. Suau, G. Pezzullo, F. Pozzi, F. Ravotti, M. Silari, and M. Tali, "Irradiation facilities at cern," in *2017 17th European Conference on Radiation and Its Effects on Components and Systems (RADECS)*, pp. 1–7, Oct 2017. [Online]. DOI: 10.1109/RADECS.2017.8696163
- [10] **G. Gorine** et al., "Fcc-hh: The hadron collider," *The European Physical Journal Special Topics*, vol. 228, no. 4, pp. 755–1107, Jul 2019. [Online]. Available: <https://doi.org/10.1140/epjst/e2019-900087-0>.

Georgi Gorine

ggorine@gmail.com

ABOUT ME

Italian and Russian nationalities.
Swiss B residence permit.
Birthday: Oct 5, 1990

LANGUAGES

- English , fluent.
- Italian , fluent.
- Russian , fluent.
- French , intermediate.
- German , learning.

LINKS

- <https://linkedin.com/in/ggorine>
- <https://orcid.org/0000-0002-7093-5835>

KEY EXPERTISE

RF Microelectronics
Embedded Systems
Microfabrication
Device Characterization
Radiation Effects
Data Analysis
Web Programming
Databases

SKILLS

- Origin • JMP • Matlab
- Clewin • Eagle • Altium
- Cadence • Sentaurus TCAD • HFSS
- Labview • Arduino
- C • Java • Python
- HTML • JavaScript • PHP • MySQL

INTERESTS

- Baseball • Volleyball
- Climbing • Hiking • Skiing
- Piano • Electrical Guitar
- DIY electronics • 3D printing

EDUCATION

ÉCOLE POLYTECHNIQUE FÉDÉRALE DE LAUSANNE

PHD IN MICROSYSTEMS AND MICROELECTRONICS

Grad. Apr 2020 | Lausanne, Switzerland

UNIVERSITY OF PAVIA

MSc IN MICROELECTRONICS

Grad. Apr 2015 | Pavia, Italy

UNIVERSITY OF PAVIA

BSc IN ELECTRONICS AND TELECOMUNICATIONS

Grad. Feb 2013 | Pavia, Italy

CORE EXPERIENCE

ON SEMICONDUCTOR | RF APPLICATIONS ENGINEER

Apr 2019 – Present | Zurich, Switzerland

- Member of the Wireless Connectivity Solutions group.
- Developing HW&SW for bench evaluation and RF demo systems.
- Expanding collateral on current and future 2.4&SubGHz portfolio.
- Supporting customers with trainings and solving of technical issues.
- Bridge between customer requirements and design team.

CERN & EPFL | PHD STUDENT

Nov 2015 – Mar 2019 | Geneva, Switzerland

- Member of the CERN EP-DT Irradiation Facilities team and of the Emerging Devices group at EPFL.
- Experience in microfabrication techniques by developing an innovative radiation sensor in the CMI cleanroom facilities of EPFL.
- Managing irradiation test campaigns for very high radiation.
- Results published and presented international conferences.

IMEC | DEVELOPMENT ENGINEER

Oct 2014 – Oct 2015 | Leuven, Belgium

- Member of the Memory Device Design group, responsible for electrical characterization and modeling of the program stability of non-volatile Resistive RAM memory cells.
- Developed software in C for wafer level automated test-benches, and scripts in statistical software (Excel, JMP, Matlab, Origin).
- Results monthly presented to core partners (Samsung, Intel, etc.).

CERN | JUNIOR HARDWARE ENGINEER (SUMMER INTERNSHIP)

Jul 2012 - Sep 2012 & Jul 2013 - Sep 2013 | Geneva, Switzerland

- Developed a portable reader for commercial radiation dosimeters (EP-RADMON), for the users of the CERN Irradiation Facilities.
- Simulated schematics (Pspice), designed and produced PCBs (Eagle), wrote C code for Arduino and other microcontrollers.

ACCENTURE | SOFTWARE DEVELOPER (SUMMER INTERNSHIP)

Jul 2011 - Aug 2011 | Naples, Italy

- As Java programmer in SW factory participated in the development of websites for the telecom companies (MySQL, PHP, Javascript, etc.).
- Communicated with the customers' beta testers in order to adjust the web-forms before online publication.

